Spin dynamics in strongly coupled spin-photon hybrid systems

Stefan Weichselbaumer

BAdW
BAYERISCHE
AKADEMIE
DER
WISSENSCHAFTEN

WALTHER
MEIßNER
INSTITUT

TECHNISCHE UNIVERSITÄT MÜNCHEN

Lehrstuhl E23 für Technische Physik

Walther-Meißner-Institut für Tieftemperaturforschung
der Bayerischen Akademie der Wissenschaften

Spin dynamics in strongly coupled spin-photon hybrid systems

Stefan Weichselbaumer

Vollständiger Abdruck der von der Fakultät für Physik der
Technischen Universität München zur Erlangung des
akademischen Grades eines

Doktors der Naturwissenschaften

genehmigten Dissertation.

Vorsitzender:	Prof. Dr. Johannes Knolle
Prüfer der Dissertation:	1. Priv.-Doz. Dr. Hans-Gregor Hübl
	2. Prof. Dr. Alexander Holleitner

Die Dissertation wurde am 16.01.2020 bei der Technischen
Universität München eingereicht und durch die Fakultät für
Physik am 17.03.2020 angenommen.

ABSTRACT

Hybrid quantum systems, consisting of a spin ensemble and a superconducting microwave resonator, have been proposed for the implementation of quantum memory applications due to the long coherence time of the spins. A key requirement for a coherent exchange of quantum information is the realization of the so-called strong coupling regime, where the interaction or coupling rate between the spin ensemble and the microwave resonator exceeds the individual loss rates of the two systems. However, the dynamics of such a coupled system are complicated, and cannot be described anymore by the behaviour of the individual subsystems.

The focus of this thesis is to deepen the understanding of the dynamics of a spin ensemble strongly coupled to a microwave resonator. In particular, we study the dynamics of the coupled system after applying a two-pulse spin echo sequence. This pulse sequence is used in quantum memory protocols to refocus the information. We observe an unexpected series of spin echo signals (echo train) when the system is in the strong coupling regime, while in the weak coupling regime we only observe a single conventional spin echo. We analyze the decay of the echo train and find a dependence on the spin coherence time and loss rates of the spin ensemble and microwave resonator. Using spin echo spectroscopy, we also investigate the spin coherence and relaxation times of the spin system in the strong coupling regime.

Furthermore, we investigate the influence of the microwave resonator on the coupling rate. We study three different superconducting resonator geometries in regard to their field homogeneity as well as their temperature and magnetic field robustness. We quantitatively calculate the expected coupling rate based on the simulated microwave magnetic field distribution of the microwave resonator and find good agreement with our experimental data.

ZUSAMMENFASSUNG

Hybride Quantensysteme, bestehend aus einem Spinensemble und einem supraleitenden Mikrowellenresonator, wurden für die Implementierung von Quantenspeichern vorgeschlagen. Eine Voraussetzung für den kohärenten Austausch von Quanteninformation stellt dabei das starke Kopplungsregime dar, in dem die Kopplungsrate zwischen dem Spinsystem und dem Mikrowellenresonator die individuellen Verlustraten beider Systeme übersteigt. Die Dynamik des stark gekoppelten Sytems ist jedoch aufgrund der vorliegenden Kopplung reichhaltiger als das der individuellen Systeme.

Der Schwerpunkt dieser Dissertation ist die Vertiefung des Verständnisses der Dynamik eines Spinsystems, das stark an einen Mikrowellenresonator gekoppelt ist. Insbesondere untersuchen wir die Dynamik des gekoppelten Systems nach Anwendung einer Spinecho-Pulssequenz. Diese Pulssequenz wird in Quantenspeicherprotokollen zum Refokussieren der Information verwendet. Wir beobachten eine Serie von Spinechosignalen, wenn sich das System im Zustand starker Kopplung befindet. Im Bereich schwacher Kopplung beobachten wir nur ein einzelnes, konventionelles Spinecho. Im Folgenden wird der Zerfall dieser Spinechosignale analysiert und ein Zusammenhang mit der Kohärenzzeit und den Verlustraten des Spinensembles und des Mikrowellenresonators hergestellt. Mithilfe von Spinecho-Spektroskopie untersuchen wir die Kohärenz- und Relaxationszeiten des Spinsystems in starker Kopplung. Desweiteren untersuchen wir den Einfluss der Mikrowellenresonatoren auf die Kopplungsrate. Zu diesem Zweck untersuchen wir drei unterschiedliche Resonatorgeometrien im Bezug auf ihre Feldhomogenität sowie ihrer Stabilität gegenüber Temperatur- und Magnetfelderhöhungen. Wir berechnen die zu erwartende Kopplungsrate, basierend auf der simulierten Feldverteilung des Mikrowellenfeldes des Resonators und finden eine gute Übereinstimmung mit experimentellen Daten.

»Ich habe keine besondere Begabung,
sondern bin nur leidenschaftlich neugierig.«

Albert Einstein

TABLE OF CONTENTS

CHAPTER 1

INTRODUCTION

Magnetic resonance is based on the absorption and emission of electromagnetic radiation by an ensemble of electron or nuclear spins. The pioneering experiments by Rabi and Zavoisky [1–3] have led to the discovery of nuclear magnetic resonance (NMR) [4, 5] and electron spin resonance (ESR). The fact that commercial ESR spectrometers are readily available and that a plethora of different types of ESR experiments exists, have lead to a widespread application in many fields of research. Presently, ESR spectroscopy is applied in solid-state physics, ranging from defect spectroscopy in semiconductor physics [6] to polymer physics [7] and biophysics [8]. It is also used in chemistry and biology [9], for example to study the structure and dynamics of proteins via site-directed spin labeling [10]. A number of excellent general review books on ESR are available [11–14], with an exhaustive list given in [6].

One can distinguish two complementary implementations of ESR spectroscopy. In continuous-wave (CW) ESR, the sample is irradiated with constant-power microwave radiation, while the magnetic field is swept. CW ESR spectroscopy offers high sensitivity, but only a limited time resolution. In contrast, in pulsed ESR spectroscopy, a time-dependent microwave amplitude is applied using short microwave pulses. This allows to directly measure relaxation times, as the duration of the microwave pulses is on the same time scale as relaxation occurs [6]. An important milestone in the development of pulsed magnetic resonance have been the observation of the free induction decay signal [15] and spin echo signals in nuclear magnetic resonance by Hahn [16] in 1950. The first electron spin echos (ESE) have been observed by Blume in 1958 [17].

Spin echos are one of the most basic and most versatile pulse sequences in pulsed magnetic resonance. For example, in an echo-detected magnetic field sweep, a simple two-pulse spin echo sequence is applied at each magnetic field sweep. The recorded ESE signal as a function of magnetic field results in an ESR spectrum comparable to a continuous-wave spectrum. Spin echos also allow the direct measurement of the coherence and relaxation times of the investigated spin ensemble. Furthermore, they are a fundamental building block for many more advanced ESR pulse sequences, where they are used to read out the spin polarization at the end of the pulse sequence [13]. These advanced pulse sequences allow to extract additional information, for example about nuclear spins present in the sample using electron spin echo envelope modulation (ESEEM) [18, 19] or electron-nuclear double resonance (ENDOR) [20–23] experiments.

Nowadays, the development of modern ESR spectroscopy focuses on increasing the spin sensitivity, i.e. the mininum number of spins that is still detectable. One approach is to increase the microwave frequency and magnetic field, which offers a higher absolute spin sensitivity as well as a high spectral resolution due to the increased thermal spin polarization [24–26]. An alternative to enhance spin sensitivity and to read out the spin state is to convert the spin information to a photon or charge state in optically or electrically detected magnetic resonance [27, 28]. These techniques allow detection on the single-spin level [29–31]. This also naturally links the technique to modern quantum information processing concepts [32, 33] and quantum sensing schemes, e.g. NV centers in diamond [34], where ESR techniques are essential for the control of the two-level spin system.

In the recent years, devices and concepts of circuit quantum electrodynamics (cQED) have been introduced in the field of ESR to implement ultra-sensitive solid-state spectroscopy at millikelvin temperatures. In cQED, the light-matter interaction between artificial atoms (two-level systems) and an electromagnetic field mode [33] is studied. The artificial atoms or qubits are implemented using superconducting quantum circuits based on Josephson junctions [35–37], while the electromagnetic field is provided by superconducting microwave resonators [38, 39]. A major milestone in the field of cQED was the realization of the strong coupling regime between a qubit and a superconducting resonator [40–45]. In the strong coupling regime, the coupling or interaction rate between the qubit and the resonator is greater than the two dissipation rates of both systems, allowing a coherent exchange of excitations [46]. These techniques enable the generation of quantum microwave signals and thus are of interest for ultra-sensitive ESR.

In addition, the introduction of quasi-noiseless amplification using Josephson parametric amplifiers [47] developed within cQED allows to bring the sensitivity of inductively-detected ESR spectrometers to the quantum level [48]. A further way to improve the spin-sensitivity is to increase the coupling rate between the microwave resonator and the spin ensemble [49, 50]. Analogously to cQED, the strong coupling regime has been achieved for a number of different paramagnetic spin systems, including NV centers in diamond [51, 52], Cr^{3+} spins in Al_2O_3 [53], Er^{3+} spins in Y_2SiO_5 [54, 55] and phosphorus donors in silicon [56]. Donor electrons in silicon have gained particular interest for the implementation of quantum information processing due to their extraordinary spin coherence times [57–59], suggesting their use in quantum memory applications. Consequently, the coherent storage of microwave excitations in a spin ensemble has been demonstrated [60–63].

The dynamics of such a strongly coupled system cannot be described anymore by the dynamics of their individual components [64], which leads to new physical effects and phenomenons. For example, spin relaxation is no longer solely determined anymore by the properties of the spin ensemble, but is influenced also by the microwave resonator [65–69]. Already in 1954, Dicke pointed out that an ensemble of two-level emitters, coupled to a common radiation field, can undergo a process called superradiance, where the spontaneous emission intensity scales non-linearly with the number of emitters [70]. Superradiance has been experimentally demonstrated also for spin ensembles coupled to a microwave resonator [71, 72].

In this thesis, we aim to further investigate the dynamics of a strongly-coupled spin-photon hybrid system. In particular, we investigate the dynamics following a two-pulse spin echo sequence. While spin echos belong to the standard repertoire of conventional ESR spectroscopy, an analysis of the dynamics of spin echos in a strongly-coupled system is still missing. Operating in the strong coupling regime is one of the key requirements to build a quantum memory protocol [46, 62]. In the implementation of these protocols, spin echos are of crucial importance, as the second pulse of the spin echo sequence effectively acts as a time reversal and thus allows an efficient refocusing of the quantum information [73, 74]. In our experiments, we observe an sequence of echo signatures (echo train) after applying a conventional two-pulse spin echo sequence, when the spin system is strongly coupled to the resonator, suggesting that the strong coupling leads to new dynamics. We analyze the decay of the echo train, which we quantitatively understand in terms of a rate equation model.

Moreover, understanding the coupling strength qualitatively and quantitatively is important in order to tailor the spin-photon coupling to the desired application. For example, in quantum memory applications, strong coupling is required for a coherent exchange of information, while in ultra-sensitive ESR spectroscopy one might prefer a lower coupling rate to avoid the complications arising from the coupled dynamics of the spin-photon hybrid system. To this end, we investigate three different resonator geometries using finite element simulations and experimental data and quantitatively calculate the expected spin-photon coupling rate, taking into account the magnetic field inhomogeneity. Additionally, we analyze them in regard to their field homogeneity as well as their temperature- and magnetic field robustness. Our results allow an evaluation of a given resonator geometry for their suitability for achieving strong coupling and enabling coherent control of the spin ensemble.

This thesis is structured as follows: In Chapter 2, we start with the foundations of electron spin resonance. We start with a classical approach first, where we introduce the resonance phenomenon and the precessional motion of the electron spin on the Bloch sphere. An intuitive picture of pulsed ESR is obtained in the rotating frame of reference, which we will discuss in the following along with the basic ESR pulse sequences. Next, we present the spin ensemble investigated in this thesis, namely phosphorus donors in silicon. Finally, we will make the transition from the classical picture to the quantum regime. In particular, we will discuss the quantization of the electromagnetic field and the coherent interaction between a single spin or an ensemble of spins with the electromagnetic radiation, leading to the strong coupling regime.

We then present the technical implementation of our pulsed ESR spectrometer in Chapter 3. We present in detail the phase-sensitive generation and detection of arbitrarily shaped microwave pulses and pulse sequences. To this end, we developed a pulsed ESR spectrometer based on an arbitrary waveform generator and a fast digitizer. Following that, we describe the microwave circuitry inside the two cryogenic setups used in this thesis. The third chapter concludes with characterization and calibration measurements of the spectrometer, both for continuous-wave and pulsed ESR measurements.

In the first main part of this thesis, Chapter 4, we present our results concerning the design and geometry of superconducting microwave resonators. We first present the three different geometries and analyze them in the following. Using finite element simulations, we are able to calculate the three-dimensional microwave magnetic field distributions of resonators. Using these results, we compare the different resonators in regard to their field homogeneity. Furthermore, we show measurements of the temperature- and magnetic field resilience of the superconducting resonators. We find that one resonator geometry in particular offers an improved field homogeneity as well as an improved temperature- and magnetic field resilience, compared to the other two resonators. In the last part of this chapter, we investigate the spin-photon coupling of an ensemble of phosphorus donor spins with the microwave resonator. We present a theoretical model based on the calculated three-dimensional microwave magnetic field distribution in order to predict the achievable coupling rate. We find a good agreement between experimental data and our model.

In Chapter 5, we investigate the dynamics of a strongly coupled spin-photon hybrid system with experiments conducted in the millikelvin regime. First, we identify two spin systems with different coupling rates using continuous-wave ESR, allowing a comparison between the strong and weak coupling regime at identical experimental conditions. We then apply standard two-pulse spin echo sequences to the two systems. In the case of the strongly coupled spin ensemble, we observe a whole series of spin echos (echo train) due to the coupled dynamics of the system. We further analyze the decay of the echo train and find good agreement with a rate equation model that takes into account the individual loss rates of the two systems. Finally, we use spin echo and inversion recovery spectroscopy to determine the coherence and life time of the two spin systems. We find an unexpected temperature dependence, which can not be explained by the coupling mechanism. We find that the coherence time as well as the life time increases with decreasing sample temperature, which is in contrast to the expected temperature independent behavior.

The thesis concludes with a summary and outlook in Chapter 6.

CHAPTER 2

FOUNDATIONS OF ELECTRON SPIN RESONANCE

2.1 A classical approach to magnetic resonance

In this section, we introduce the fundamental principles of electron spin resonance (ESR), following the seminal book by Schweiger and Jeschke [13]. A rigorous description of ESR requires a quantum mechanical approach, as quantum objects (i.e. spins) are involved. In this thesis, however, we will consider a spin ensemble with a large number of spins, N, which allows to describe the fundamental principles of ESR with a classical approach

2.1.1 The resonance phenomenon and rotating frame of reference

Consider an electron with an intrinsic angular momentum (spin) of $S = 1/2$. The spin of an electron gives rise to a magnetic moment

$$\vec{\mu} = \frac{q}{2m}\hbar\vec{S}, \tag{2.1}$$

where q and m are the charge and mass of the particle. With the electron mass m_e and the elementary charge $q = -e$, the Bohr magneton is defined as

$$\mu_\mathrm{B} = \frac{e\hbar}{2m_e}, \tag{2.2}$$

and therefore Eq. (2.1) can be rewritten as

$$\vec{\mu} = -g_\mathrm{e}\mu_\mathrm{B}\vec{S}, \tag{2.3}$$

where g_e is the electron g-factor or Landé-factor. In general, the g-factor deviates from the g-factor of free electrons ($g_\mathrm{free} \approx 2.00232$ [75]) and is a material dependent quantity.

In the presence of an arbitrary (time-dependent) magnetic field $\vec{B}(t)$[1], the classical equation of motion of a magnetic moment is given by [4]

$$\frac{\mathrm{d}\vec{\mu}}{\mathrm{d}t} = -\frac{g_\mathrm{e}\mu_\mathrm{B}}{\hbar}\vec{\mu} \times \vec{B}. \tag{2.4}$$

In an spin ensemble, the individual magnetic moments of each electron add up to a macroscopic magnetic moment. In an ESR experiment, the detected quantity is the voltage induced by the precessional motion of the magnetization $\vec{M}$, which is defined as the net magnetic moment

---

[1] The magnetic induction B is related to the magnetic field strength H via $B = \mu_r\mu_0 H$, where μ_r is the relative permeability. It can be related to the susceptibility χ via $\mu_r = 1 + \chi$. For paramagnetic materials, χ is in the order of 10^{-6}, and therefore $\mu_r \approx 1$, resulting in $B \approx \mu_0 H$. Hence, we use the term magnetic field and magnetic induction synonymously.

per unit volume V:

$$\vec{M} = \frac{1}{V} \sum_i \vec{\mu}_i. \tag{2.5}$$

Combining Eq. (2.4) and (2.5), the equation of motion can be written as

$$\frac{\mathrm{d}\vec{M}}{\mathrm{d}t} = -\frac{g_\mathrm{e}\mu_\mathrm{B}}{\hbar}\vec{M} \times \vec{B}. \tag{2.6}$$

In the following, we assume a static magnetic field along the z direction, $\vec{B}(t) = B_0\vec{e}_z$. In this case, the equation of motion of the magnetization reduces to

$$\frac{\mathrm{d}\vec{M}}{\mathrm{d}t} = -\omega_\mathrm{s}\vec{M} \times \vec{e}_z, \tag{2.7}$$

where $\omega_\mathrm{s} = (g_\mathrm{e}\mu_\mathrm{B}/\hbar)B_0$ is the so-called Larmor frequency. This equation describes the precession of the magnetization vector around the static magnetic field direction at frequency ω_s. Note that the length of the magnetization vector does not change. Therefore, the tip of the magnetization vector moves on a sphere with radius M, as depicted in Fig. 2.1 (a)[2].

In the following, we introduce an additional, oscillatory magnetic field $\vec{B}_1 = 2B_1 \cos(\omega t)\, \vec{e}_x$ with frequency ω, that is perpendicular to $\vec{B}_0$. To discuss the motion of the magnetization, it is convenient to describe the system in a rotating frame of reference, which rotates in the right-hand sense with frequency ω[3]. Here, the oscillatory magnetic field becomes time-independent, when one neglects fast-rotating terms in 2ω:

$$\tilde{B}_1 = B_1\tilde{e}_x. \tag{2.8}$$

The fast rotating term appears because a linear polarized field can be expressed as a superposition of a right-hand and left-hand circular polarized field. When changing to the rotating frame of reference, the right-hand term becomes time-independent and the left-hand

---

[2] For a single spin-1/2 particle, this sphere is called Bloch sphere.

[3] In the following, we denote vectors in the rotating frame of reference with a tilde symbol.

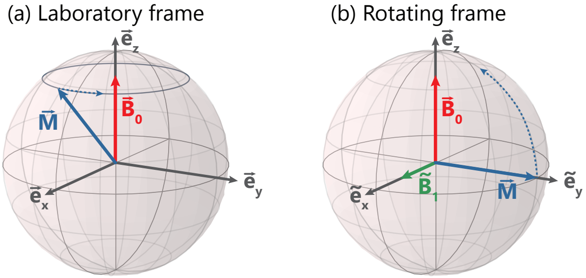

Fig. 2.1 (a) In the laboratory frame, the magnetization vector $\vec{M}$ precesses with a frequency ω_s around the static magnetic field $\vec{B}_0$. (b) In the rotating frame, an additional oscillatory magnetic field $\vec{B}_1$ with frequency ω appears to be static. The magnetization precesses around the additional $\tilde{B}_1$ field (nutation).

term rotates with 2ω. However, for $B_1 \ll B_0$, i.e. when the oscillatory magnetic field acts only as a perturbation to the static magnetic field, the fast-rotating terms can be neglected. This condition is always fulfilled in our experiments. An complete derivation for circular polarized radiation is given in Ref. [13].

In the rotating frame, the equation of motions for $\vec{M}$ are given by

$$\frac{\mathrm{d}\tilde{M}_x}{\mathrm{d}t} = -\Delta_\mathrm{s}\tilde{M}_y, \tag{2.9}$$

$$\frac{\mathrm{d}\tilde{M}_y}{\mathrm{d}t} = \Delta_\mathrm{s}\tilde{M}_x - \omega_1\tilde{M}_z, \tag{2.10}$$

$$\frac{\mathrm{d}\tilde{M}_z}{\mathrm{d}t} = \omega_1\tilde{M}_y. \tag{2.11}$$

The equations of motion (2.9)–(2.11) describe the precessional motion. First, $\tilde{M}$ precesses around the z-axis with the resonance offset frequency $\Delta_\mathrm{s} = \omega_\mathrm{s} - \omega$. Second, $\tilde{M}$ precesses around the direction of $\tilde{B}_1$ with the frequency $\omega_1 = (g_\mathrm{e}\mu_\mathrm{B}/\hbar)B_1$. The superposition of both precessional movements is called *nutation*, where the magnetization rotates around an effective magnetic field $\omega_1\tilde{e}_x + \Delta_\mathrm{s}\tilde{e}_z$ with the Rabi (or nutation) frequency

$$\Omega_{\mathrm{R}} = \sqrt{\Delta_{\mathrm{s}}^2 + \omega_1^2}. \tag{2.12}$$

In the resonant case, the detuning $\Delta_{\mathrm{s}} = 0$ and the precession axis is parallel to $\tilde{e}_x$. This nutation is shown in Fig. 2.1 (b).

The rotational axis of the nutation in the on-resonant case can be changed by applying a phase shift ϕ to the oscillatory magnetic field. Then, in the laboratory frame $\vec{B}_1(t) = 2B_1 \cos\left(\omega t + \phi\right) \vec{e}_x$. In the rotating frame of reference this becomes

$$\tilde{B}_1 = B_1 \cos(\phi)\tilde{e}_x + B_1 \sin(\phi)\tilde{e}_y. \tag{2.13}$$

This can be used for an arbitrary manipulation of the magnetization vector. Furthermore, by applying the oscillatory B_1 field only for a certain time period t_{p}, the magnetization can be flipped by a rotation angle θ:

$$\theta = \frac{g_{\mathrm{e}}\mu_{\mathrm{B}}}{\hbar} \int_0^{t_{\mathrm{p}}} \left|\tilde{B}_1(t)\right| \,\mathrm{d}t. \tag{2.14}$$

Choosing the pulse phase ϕ and the pulse length t_{p} appropriately allows to bring the magnetization vector to an arbitrary point on the sphere surface. Note that this procedure is still valid for small resonance offsets, as long as $\Delta_{\mathrm{s}} \ll \omega_1$ holds [13].

2.1.2 Relaxation and the Bloch equations

So far, we have only considered the ideal case of a precessional motion: Once started, the precessional motion of the magnetization continues forever. In reality, however, there are always relaxation processes which restore the magnetization to its thermal equilibrium state, $\vec{M}_0 \parallel \vec{B}_0$. In the following, we give a phenomenological description of the magnetization relaxation. One can distinguish two processes:

- *Longitudinal relaxation*: In this process, the spin ensemble loses energy (e.g. to the lattice) and the longitudinal magnetization along z relaxes to its equilibrium state $\vec{M}_0$. With the characteristic longitudinal relaxation time T_1, the relaxation of M_z is given by

$$\frac{\mathrm{d}M_z}{\mathrm{d}t} = \frac{-(M_z - M_0)}{T_1}. \tag{2.15}$$

- *Transverse relaxation or decoherence*: The transverse magnetization in the xy plane is also subject to relaxation and vanishes with a time constant T_2. In general, T_2 differs from T_1 and is usually much smaller. The relaxation of the x and y component of the magnetization are then given by

$$\frac{\mathrm{d}M_{x,y}}{\mathrm{d}t} = \frac{-M_{x,y}}{T_2}. \tag{2.16}$$

We can now introduce these relaxation mechanisms in the equations of motion (2.9)–(2.11) and obtain the famous Bloch equations [4], which describe the spin dynamics of an ensemble of two-level systems:

$$\frac{\mathrm{d}\tilde{M}_x}{\mathrm{d}t} = -\Delta_\mathrm{s}\tilde{M}_y - \frac{M_x}{T_2}, \tag{2.17}$$

$$\frac{\mathrm{d}\tilde{M}_y}{\mathrm{d}t} = \Delta_\mathrm{s}\tilde{M}_x - \omega_1\tilde{M}_z - \frac{M_y}{T_2}, \tag{2.18}$$

$$\frac{\mathrm{d}\tilde{M}_z}{\mathrm{d}t} = \omega_1\tilde{M}_y - \frac{M_z - M_0}{T_1}. \tag{2.19}$$

A spin ensemble that experiences the same time-averaged local fields is called a spin packet and has a linewidth $1/T_2$. The origin of this linewidth is transverse relaxation, e.g. due to fluctuating fields caused by electron and nuclear spin flips. Besides this *homogeneous broadening* of the resonance frequencies, the spin ensemble can also be subject to *inhomogeneous broadening*. One possible source of inhomogeneous broadening is, for example, a spatial inhomogeneity of the static magnetic field, which introduces a spatial variation of the Larmor frequency across the sample. Another possible source are unresolved hyperfine interactions, where the electrons spin interacts with many nuclear spins. A inhomogeneously broadened line consists of a superposition of spin packets. It has a linewidth $1/T_2^*$, which can be much larger than the homogeneously broadened linewidth. However, as we will discuss later, it is possible to counteract the effects of inhomogeneous broadening.

2.1.3 Pulsed ESR and inductive detection

We previously investigated the effect of an oscillatory B_1 field on the magnetization. We saw in Eq. (2.13) and (2.14) that the magnetization vector can be moved to an arbitrary point on the Bloch sphere by applying an appropriate microwave pulse. We will now investigate the effect of such pulses on the electron spin ensemble and the subsequent detection of the precessional motion of the magnetization.

We show a schematic of a typical ESR setup based on inductive detection in Fig. 2.2. A spin ensemble is embedded in the inductor of a RLC circuit with frequency ω_r. The Larmor frequency of the spin ensemble is tuned by the external static magnetic field $\vec{B}_0$ to the microwave resonator: $\omega_\mathrm{s} \approx \omega_\mathrm{r}$. When a microwave pulse is applied, the inductor generates an oscillatory $\vec{B}_1$ field at the location of the spins and orthogonal to $\vec{B}_0$. According to the principles discussed above, the magnetization rotates away from thermal equilibrium along z and the components M_x and M_y of the magnetization become non-zero.

The detection of this transverse magnetization takes place in the inductor. In the laboratory frame, the magnetization precesses around $\vec{B}_0$ with ω_s. This precession induces a voltage in the inductor by an electromotive force, which is subsequently detected using a quadrature-detection scheme. This allows to simultaneously detect both M_x and

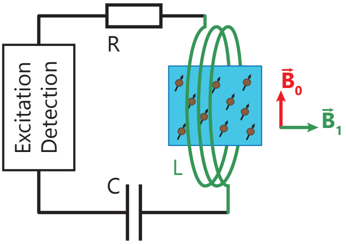

Fig. 2.2 Schematic of an inductive detection ESR setup. A spin ensemble is embedded in the inductor of an RLC circuit, which generates an oscillatory magnetic field $\vec{B}_1$, perpendicular to a static magnetic field $\vec{B}_0$. Vice versa, a precessing, transverse magnetization induces an oscillatory current in the inductor, which is subsequently detected. Note that we assume here a weak interaction between the spin ensemble and the RLC circuit. Figure adapted from Ref. [76].

M_y as the real and imaginary part of a complex voltage signal[4]:

$$V(t) \propto \left(\tilde{M}_y(t) + i\tilde{M}_x(t)\right) e^{i\omega_s t}. \tag{2.20}$$

For the discussion above, we assume a weak interaction between the spin ensemble and the RLC circuit, i.e. the influence of the spin ensemble on the RLC circuit can be modeled as a weak perturbation. The case of a strong interaction will be discussed in Sec. 2.3. We will now show several pulse sequences, which create transverse magnetization and discuss which information can be obtained from applying them.

Free induction decay

The simplest pulsed ESR experiment consists of a single microwave pulse. At $t = 0$ the magnetization is in its equilibrium state along the z axis. The microwave pulse with length t_p then rotates the magnetiza-

---

[4] Note that the longitudinal magnetization M_z cannot be detected directly with inductively-detected ESR setups [13]. In contrast, electrically- or optically-detected magnetic resonance experiments [27, 28, 77] are sensitive to the z component of the magnetization.

tion by 90° around the x axis, so that after the pulse the magnetization is on the equator of the Bloch sphere, creating a transverse magnetization.

As we discussed in the previous section, the magnetization is also subject to relaxation and decoherence, characterized by the T_1 and T_2^* time constants (we assume an inhomogeneous broadening here). The detected signal is given by

$$V(t) \propto \left(\tilde{M}_y(t) + i\tilde{M}_x(t)\right) e^{i\omega_\mathrm{s} t} e^{-t/T_2^*}. \tag{2.21}$$

We have neglected T_1 relaxation here, as the decay is usually dominated by the inhomogeneous broadening ($T_2^* \ll T_1$). This type of signal is called *free-induction decay*, as it describes the decay of the inductive signal during free evolution. It can be used to extract the inhomogeneous relaxation rate T_2^*.

Spin echo

The spin echo pulse sequence [16] allows to counteract the effects of inhomogeneous broadening, such that the coherence time of the magnetization is determined by the (inherent) homogeneous broadening. The coherence time defines the timescale in which quantum information survives and in consequence the time frame for quantum computing and quantum memory protocols. In the following, we discuss the echo formation in the weak coupling regime [78]. In the main part of this thesis, however, we investigate the influence of spin echos in a strong coupling environment, where the coupled dynamics of the spin ensemble and the microwave resonator are much more complicated than described here.

Technically, a spin echo consists of two microwave pulses with pulse durations of $t_{\pi/2}$ and t_π, separated by a free evolution period with length τ. The principle of a two-pulse spin echo is shown in Fig. 2.3. The top panel shows the resonator signal of the microwave pulses (blue) and the induced spin echo signal (green) as a function of time.

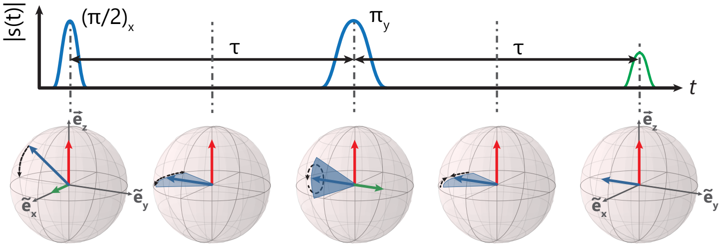

Fig. 2.3 Principle of a spin echo sequence with the corresponding position of the magnetization vector on the surface of a sphere (in the rotating frame).

In the lower part of the figure, the movement of $\vec{M}$ is depicted in a "Bloch sphere"-like representation.

At the start of the sequence, the magnetization $\vec{M}$ (blue arrow) points along the static magnetic field $\vec{B}_0$ (red arrow). A "hard" $\pi/2$ pulse generates an oscillatory B_1 field along the x axis (green arrow) and rotates the magnetization to the $-y$ axis. A hard microwave pulse describes a short pulse with a high excitation bandwidth, such that all magnetization is rotated away from the z axis [78].

During the free evolution period, the magnetization is subject to decoherence and dephases, as each spin experiences a slightly different local B_0 field. When choosing two spins at random, the dephasing can be visualized by the spins lagging behind or advancing with respect to the magnetization in the rotating frame of reference. This "fanning out" is indicated by the blue-shaded circular sector in the second panel of Fig. 2.3 and is nothing less than the free-induction decay discussed previously. The observed signal is the sum of all vectors, which will decrease on a timescale T_2^*.

After the free evolution period τ, a hard π pulse (refocusing pulse) with a phase-shift of 180° with respect to the first pulse is applied. The oscillatory B_1 field generated by this pulse rotates the magnetization by 180° degrees around the y axis. This effectively corresponds to an time-inversion, so that during the second free evolution period all inhomogeneous effects are reversed. The two vectors from before will now coincide again with the $-y$ axis after a time τ and a spin echo is formed. The time-reversal operation during the spin echo removes all inhomogeneous broadening effects, so that the homogeneous spin coherence time T_2 can be measured by varying the length of the free evolution period τ.

While we discussed here the case for ideal $\pi/2$- and π-pulses, a spin echo occurs for almost any combination of two microwave pulses [13]. In particular, it is not necessary to rotate the magnetization by exactly 90° and 180° [78]. The microwave resonators used in our experiments inherently generate an inhomogeneous B_1 field such that spins in different areas of the sample experience different rotation angles. As long as there is a non-zero magnetization in the equatorial plane after 2τ, a spin echo is formed.

Inversion recovery

The last pulse sequence we discuss is the inversion recovery sequence, which is used to experimentally determine the longitudinal relaxation time T_1. It consists of three microwave pulses. The first π-pulse inverts the magnetization and brings it to the $-z$ axis. After a variable wait time t_{wait}, the z component of the magnetization has decayed towards its equilibrium position according to Eq. (2.19). This component or projection is then measured using a spin echo sequence. By varying t_{wait}, the spin lifetime T_1 can be determined. Note that t_{wait} should be chosen longer than $5 \cdot T_2$, such that the magnetization completely dephases before the last two pulses are applied.

2.2 Phosphorus donors in silicon

The spin ensemble investigated in this thesis consists of phosphorus donors in a silicon host crystal. Donors in silicon have been investigated since the beginning of ESR spectroscopy [79–82]. A wide range of reference data is available, including measurements regarding the hyperfine interaction of the donors [81, 83–86], exchange-effects of donors [87–90] and coherence time and spin life time measurements [82, 91–93]. In particular, phosphorus donors in an isotopically purified ^{28}Si:P crystal are of interest, as their ultra-long coherence times [57–59] enable the implementation of quantum computing and quantum storage protocols. This makes donors in silicon an ideal benchmark system to verify the correct operation of our homebuilt ESR spectrometer.

2.2.1 The spin Hamiltonian

A phosphorus donor introduced in the silicon lattice provides an unbound electron with electron spin $S = 1/2$ as well as a nuclear spin from the ^{31}P nuclei of $I = 1/2$. The spin Hamiltonian of phosphorus donors in an external magnetic field $\vec{B}_0 = B_0\hat{z}$ is given by [12, 13]

$$\mathcal{H}_{\mathrm{r}} = g_{\mathrm{e}}\mu_{\mathrm{B}}\vec{S}\cdot\vec{B}_0 - g_{\mathrm{n}}\mu_{\mathrm{n}}\vec{I}\cdot\vec{B}_0 + A\vec{S}\cdot\vec{I}. \tag{2.22}$$

The first two terms describe the Zeeman interaction of the electron and nuclear spin with the external magnetic field with their corresponding g-factors $g_{\mathrm{e}} = 1.9985$ [81] and $g_{\mathrm{n}} = 2.2632$ [94]. μ_{B} and μ_{n} are the Bohr and nuclear magneton, respectively. The last term in Eq. (2.22) describes an isotropic Fermi-contact interaction with a hyperfine constant $A/h = 117.53\,\mathrm{MHz}$ [81], where h is Planck's constant.

The corresponding eigenstates of the spin Hamiltonian in Eq. (2.22) are given by [95]

$$|1\rangle = |\uparrow\Uparrow\rangle, \tag{2.23}$$

$$|2\rangle = \alpha|\uparrow\Downarrow\rangle + \beta|\downarrow\Uparrow\rangle, \tag{2.24}$$

$$|3\rangle = -\beta|\uparrow\Downarrow\rangle + \alpha|\downarrow\Uparrow\rangle, \tag{2.25}$$

$$|4\rangle = |\downarrow\Downarrow\rangle, \tag{2.26}$$

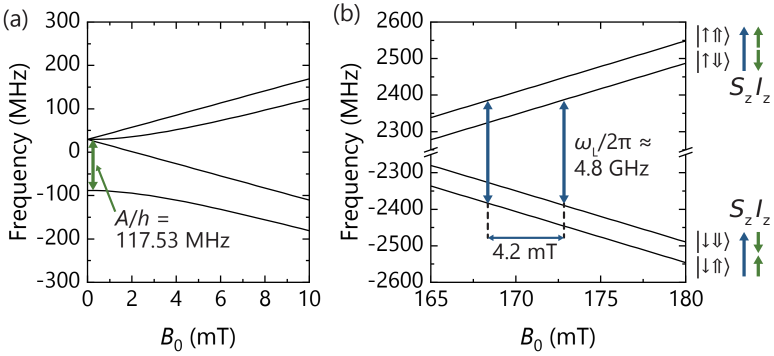

Fig. 2.4 Breit-Rabi diagram of phosphorus donors in silicon for the spin Hamiltonian given in Eq. (2.22). (a) In the low-field limit, the eigenstates split in a spin single and spin triplet, separated by the hyperfine interaction. (b) In the high-field limit, the degeneracy of the triplet state is lifted, resulting in four distinct eigenstates. This gives rise to two possible ESR transitions (blue arrows), separated by 4.2 mT in magnetic field.

where ↑, ↓ and ⇑, ⇓ describe the spin state of the electron and nuclear spin, respectively. The coefficients $\alpha = \cos\frac{\eta}{2}$ and $\beta = \sin\frac{\eta}{2}$ depend on the mixing angle $\eta = A/(g_e\mu_B B_0 - g_n\mu_n B_0)$. The corresponding eigenenergies of the four states as a function of the applied magnetic field are shown in Fig. 2.4 in the (a) low-field limit and (b) high-field regime. At low magnetic fields, the eigenstates split into a spin singlet and triplet, separated by the hyperfine energy A (indicated by a green arrow).

The experiments presented in this thesis are performed in the high-field regime, where $\omega_s \approx 4.8\,\text{GHz} \gg A/h = 117.53\,\text{MHz}$. Here, $\eta \approx 0$ and the eigenstates can be described by four distinct states $|\uparrow\Uparrow\rangle$, $|\uparrow\Downarrow\rangle$, $|\downarrow\Uparrow\rangle$ and $|\downarrow\Downarrow\rangle$. The spin states are indicated next to the corresponding eigenenergies in Fig. 2.4 (b) in the high-field case. The eigenstates give rise to the two dipole-allowed ESR transitions with $\Delta m_s = 1$. The two ESR transitions are separated by the hyperfine interaction corresponding to 4.2 mT in the magnetic field axis (indicated by blue arrows).

In natural silicon, the phosphorus electron spin is subject to an additional hyperfine interaction with the nuclear spin $I = 1/2$ of nearby ^{29}Si nuclei [81, 84, 96]. Due to the statistical distribution of the ^{29}Si nuclei on the lattice, this hyperfine interaction experienced by each phosphorus electron spin also varies, leading to additional electron spin transitions with varying transition frequencies. Since the additional hyperfine splitting is small compared to the homogeneous linewidth, these additional transitions cannot be spectroscopically resolved, but lead to an inhomogeneous broadening of the electron spin transition [97].

2.2.2 Exchange-coupled phosphorus donors (P_2 dimers)

A further complication of the ESR spectrum arises in samples with intermediate doping concentrations $1 \times 10^{16}\,\mathrm{cm}^{-}3 \lessapprox N_\mathrm{D} \lessapprox 2 \times 10^{18}\,\mathrm{cm}^{-}3$ [98]. In this doping regime, the distance between neighboring phosphorus centers is small enough, such that the wave function of the two electrons can overlap. This gives rise to statistically formed exchange-coupled donor pairs (P_2 dimers) [79, 87, 89]. Due to the random distribution of donor atoms, the distance between dimer constituents varies over a broad range and therefore leads to a broad distribution of exchange couplings. The spin Hamiltonian of a pair of donor atoms can be written as [88]

$$\begin{aligned}\mathcal{H}_\mathrm{r} = {} & g_\mathrm{e}\mu_\mathrm{B}\left(\vec{S}_1 + \vec{S}_2\right)\cdot\vec{B}_0 - g_\mathrm{n}\mu_\mathrm{n}\left(\vec{I}_1 + \vec{I}_2\right)\cdot\vec{B}_0 \\ & + A\left(\vec{S}_1\cdot\vec{I}_1 + \vec{S}_1\cdot\vec{I}_1\right) + J\vec{S}_1\cdot\vec{S}_2. \end{aligned} \tag{2.27}$$

Here, $\vec{S}_i$ and $\vec{I}_i$ are the electron and nuclear spins of the two donors. The last term describes the exchange coupling between the two electron spins with the exchange coupling constant J.

The subset of dimers with $J > A$ forms a ESR line in the center between the two hyperfine transitions [90]. The eigenstates for $J > A$ consist of a spin-0 singlet state and three spin-1 triplet states [99]. In total, eight ESR transitions are allowed, that can be combined into four pairs

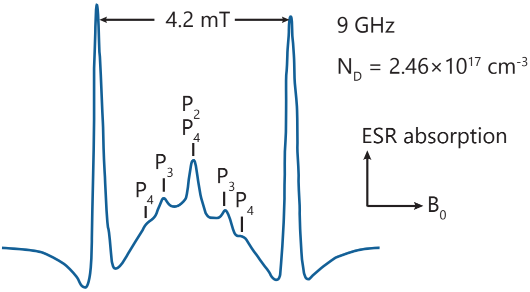

Fig. 2.5 ESR absorption spectrum as a function of magnetic field of a phosphorus-doped silicon crystal. The doping concentration is $N_{\mathrm{D}} = 2.46 \times 10^{17}\,\mathrm{cm}^{-3}$. Besides the two hyperfine transitions (separated by 4.2 mT), additional peaks due to exchange-coupled donor pairs (and higher order clusters) are visible in the center of the spectrum. Figure adapted from Ref. [100].

of transitions with identical transition frequencies. Two of the pairs have an transition frequency coinciding with the transition frequency of the isolated donors and are thus indistinguishable from the much stronger transitions of the isolated donors [99]. The other two pairs have distinct transition frequencies and contribute to a central ESR line between the two hyperfine transitions. We show an exemplary absorption spectrum of a phosphorus-doped silicon crystal with a doping concentration of $N_{\mathrm{D}} = 2.46 \times 10^{17}\,\mathrm{cm}^{-3}$, recorded at 9 GHz, in Fig. 2.5 (adapted from Ref. [100]).

At the edges of the spectrum, the two phosphorus hyperfine-split transitions, separated by 4.2 mT, are visible. The center of the spectrum contains additional structures due to the exchange coupling between phosphorus donors. Several peaks are noticeable, corresponding to phosphorus dimers (P_2) as well as higher-order clusters (P_3, P_4). The exact position of the P_2 peak can be determined by solving the Hamiltonian in Eq. (2.27) [88]. Underlying the peaks is a broad background signal, known as *broad center line* (BCL) in literature [98]. The BCL arises primarily from clusters of three or more donors [98] and interactions between higher-order clusters [101, 102].

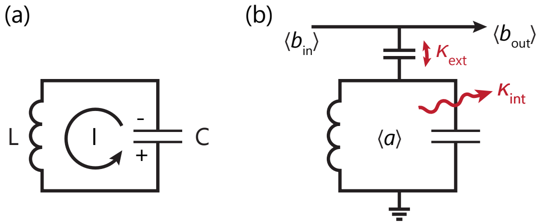

Fig. 2.6 (a) Schematic drawing of a resonant LC oscillator. The energy oscillates between the inductor L and the capacitor C. It is stored in the magnetic field of the inductor or the electric field of the capacitor, respectively. (b) LC oscillator with internal dissipation rate κ_{int}, coupled to a microwave feedline with the coupling rate κ_{ext}.

2.3 Magnetic resonance in the quantum regime

Now that we have established the basic principles of magnetic resonance and have introduced the spin system under investigation, we will discuss the quantum mechanical treatment of magnetic resonance. In this work, we perform magnetic resonance experiments at temperatures, where both the microwave resonator and the spin ensemble are cooled to their quantum mechanical groundstate. Therefore, we start with the quantum mechanical description of an LC oscillator and then discuss the interaction between a spin ensemble and the quantized field mode of a microwave resonator.

2.3.1 The classical and quantum LC oscillator

Consider a simple circuit with an inductor L and a capacitor C, as depicted in Fig. 2.6 (a). As is known from classical electrodynamics, such a circuit represents a simple LC oscillator. The energy is stored either in the magnetic field of the inductor or the electric field of the capacitor and oscillates back and forth between the two. In the following, we follow the discussion in Ref. [12, 103].

The inductance L is a measure how much magnetic flux Φ is created when a current I_{L} flows through the inductor, hence $L = \Phi / I_{\mathrm{L}}$. Additionally, Faraday's law states that a current flow also leads to a voltage induced in the inductor given by $V_\mathrm{L} = L\frac{\mathrm{d}I_\mathrm{L}}{\mathrm{d}t}$. In contrast to that, the capacitor is characterized by the charge q stored on the capacitor plates and the voltage V_C across it, giving rise to the capacitance $C = q/V_\mathrm{C}$. Applying Kirchhoff's laws, we find for the voltages and currents

$$V_\mathrm{C} + V_\mathrm{L} = 0, \quad I_\mathrm{C} = I_\mathrm{L} = I \tag{2.28}$$

and with this we can derive the characteristic equation

$$\frac{\mathrm{d}^2}{\mathrm{d}t^2} I + \omega_\mathrm{r} I = 0, \tag{2.29}$$

where the resonance frequency is given by $\omega_\mathrm{r}^2 = \frac{1}{LC}$. The energy stored in the inductance and capacitance is given by $E_\mathrm{L} = \frac{1}{2}LI^2 = \frac{\Phi}{2L}$ and $E_\mathrm{C} = \frac{1}{2}CV^2 = \frac{q^2}{2C}$.

Once the total energy density in the circuit is known, we can now make a transition to Hamilton's mechanics [104]. The Hamilton is given by

$$\mathcal{H}_\mathrm{r} = \frac{1}{2}\left(\frac{q^2}{C} + L\dot{q}^2\right) = \frac{1}{2}\left(\frac{q^2}{C} + \frac{\Phi^2}{L}\right) \tag{2.30}$$

with $\partial\mathcal{H}_\mathrm{r}/\partial q = -\dot{\Phi} = q/C$ and $\partial\mathcal{H}_\mathrm{r}/\partial\Phi = \dot{q} = \Phi/L$. We can associate the magnetic flux Φ with the "kinetic" energy stored in the inductor and the electric charge q with the "potential" energy stored in the capacitor. Therefore, Φ and q are the canonical variables of a harmonic oscillator. The circuit can be quantized using the commutator relationship for canonical variables, $\left[\Phi, q\right] = -i\hbar$, and the introduction of annihilation and creation operators, a and $a^\dagger$, as

$$q = \sqrt{\frac{\hbar}{2Z}}\left(a + a^\dagger\right) \text{ and } \Phi = -i\sqrt{\frac{\hbar Z}{2}}\left(a - a^\dagger\right), \tag{2.31}$$

where $Z = \sqrt{L/C}$ is the characteristic impedance of the circuit [103]. With this, the Hamiltonian for a loss-less quantized LC oscillator is given by

$$\mathcal{H}_{\mathrm{r}} = \hbar\omega_{\mathrm{r}}\left(a^{\dagger}a + \frac{1}{2}\right). \tag{2.32}$$

Driven, dissipative LC oscillator and input-output model

So far, we discussed an ideal classical LC oscillator and introduced the quantized version of it. Of course, in a real experiment, the LC circuit is also dissipative (and then becomes a RLC circuit) and is also powered by an external drive. In the field of quantum optics, this problem is treated using the input-output formalism [64, 105, 106]. Here the Hamiltonian in Eq. (2.32) is used in a Master equation approach. The equation of motion for the cavity field operator a in the Heisenberg picture is then given by [105, 107]

$$\begin{aligned}\dot{a} &= \frac{i}{\hbar}\left[a, \mathcal{H}_{\mathrm{r}}\right] - \left(\kappa_{\mathrm{int}} + \kappa_{\mathrm{ext}}\right)a + \sqrt{\kappa_{\mathrm{ext}}}c_{\mathrm{in}} \\ &= i\omega_{\mathrm{r}}a - \left(\kappa_{\mathrm{int}} + \kappa_{\mathrm{ext}}\right)a + \sqrt{\kappa_{\mathrm{ext}}}c_{\mathrm{in}} \end{aligned} \tag{2.33}$$

We have introduced here the damping rates κ_{int} and κ_{ext} in a Markovian approximation, which describe the internal dissipation of the LC circuit as well as the coupling rate to an external drive c_{in}. c_{in} is normalized in such a way that $P_{\mathrm{S}} = \hbar\omega\langle c_{\mathrm{in}}^{\dagger}c_{\mathrm{in}}\rangle$ is the applied sample power and $\langle c_{\mathrm{in}}^{\dagger}c_{\mathrm{in}}\rangle$ describes the rate of photons impinging on the cavity [108]. We show an schematic of this setup in Fig. 2.6 (b). The output of the system is given by [105]

$$c_{\mathrm{out}} = c_{\mathrm{in}} - \sqrt{\kappa_{\mathrm{ext}}}a. \tag{2.34}$$

Next, we derive the steady-state solution of Eq. 2.33. We assume an external probe tone $c_{\mathrm{in}} = c_0 e^{i\omega t}$ with frequency ω. In the frame rotating with the probe tone frequency, Eq. (2.33) reads [109]

$$\dot{a} = -\left(i\Delta + \kappa_{\mathrm{c}}\right)a + \sqrt{\kappa_{\mathrm{ext}}}c_0, \tag{2.35}$$

where we introduced the frequency detuning $\Delta = \omega - \omega_r$ and the total loss rate $\kappa_\mathrm{c} = \kappa_\mathrm{ext} + \kappa_\mathrm{int}$. Solving for the steady-state, i.e. $\dot{a} = 0$, we obtain for the average field amplitude:

$$\langle a \rangle_\mathrm{st} = \frac{\sqrt{\kappa_\mathrm{ext}}}{\kappa + i\Delta} c_0, \tag{2.36}$$

In the experiment, we do not have direct access to the field amplitude a inside the resonator. However, we are able to measure the transmitted signal c_out in order to determine the transmission parameter S_{21}:

$$S_{21}(\omega) = \frac{\langle c_\mathrm{out} \rangle}{\langle c_\mathrm{in} \rangle} = 1 - \frac{\kappa_\mathrm{ext}}{\kappa + i\Delta}. \tag{2.37}$$

We will explain in the following chapter how S_{21} is determined experimentally.

Using the normalization relation of the input field c_in, we can give an expression for the steady-state resonator population, i.e. the average number of photons in the resonator [108]:

$$\bar{n}_\mathrm{ph} = \langle a^\dagger a \rangle = |\langle a \rangle|^2 = \frac{\kappa_\mathrm{ext}}{\Delta^2 + \kappa^2} \frac{P_\mathrm{S}}{\hbar\omega}. \tag{2.38}$$

On resonance, $\Delta = 0$ and the expression above simplifies to

$$n_\mathrm{ph} = \frac{\kappa_\mathrm{ext}}{\kappa^2} \frac{P_\mathrm{S}}{\hbar\omega_\mathrm{r}}. \tag{2.39}$$

2.3.2 Spin-photon interaction and the Jaynes-Cummings model

In the following, we discuss the interaction of a single, quantized field mode with a single spin 1/2 on the basis of the Jaynes-Cummings model [110]. This model is the foundation in many fields of quantum information processing, e.g. in cavity and circuit quantum electrodynamics (cQED). We follow the discussion of Ref. [64, 104].

The Jaynes-Cummings Hamiltonian consists of three parts and is given by

$$\mathcal{H}_{\mathrm{JC}} = \mathcal{H}_{\mathrm{r}} + \mathcal{H}_{\mathrm{spin}} + \mathcal{H}_{\mathrm{int}}, \tag{2.40}$$

with $\mathcal{H}_{\mathrm{r}} = \hbar\omega_{\mathrm{r}} a^{\dagger} a$, as described previously and $\mathcal{H}_{\mathrm{spin}} = \frac{1}{2}\hbar\omega_{\mathrm{s}} \left(|\downarrow\rangle\langle\downarrow| - |\uparrow\rangle\langle\uparrow|\right) = \frac{1}{2}\hbar\omega_{\mathrm{s}}\sigma_{\mathrm{z}}$ describing the spin. The last term describes the interaction between the spin and the electromagnetic field inside the resonator. The spin is treated as a quantum mechanical two-level system (TLS) with two eigenstates, $|\downarrow\rangle$ and $|\uparrow\rangle$ using the Pauli spin matrices σ_{z}.

While the interaction Hamiltonian can describe any type of interaction between the TLS and the resonator field mode, we are interested in the interaction of the resonator magnetic field with the spin magnetic dipole moment. According to Eq. (2.1), the magnetic moment is written as $\vec{\mu} = -\frac{g_{\mathrm{e}}\mu_{\mathrm{B}}}{\hbar}\vec{S}$, where $\vec{S}$ is the spin of the electron. With this, the interaction Hamiltonian reads

$$\mathcal{H}_{\mathrm{int}} = -\vec{\mu} \times \vec{B}_1, \tag{2.41}$$

where $\vec{B}_1$ is the magnetic field inside the resonator.

The magnetic moment of the TLS can be rewritten as

$$\vec{\mu} = -\frac{g_{\mathrm{e}}\mu_{\mathrm{B}}}{\hbar} \sum_{ij} |i\rangle\langle i|\vec{\sigma}|j\rangle\langle j|, \tag{2.42}$$

where $|i\rangle = |\uparrow\rangle$ and $|j\rangle = |\downarrow\rangle$ describe the two eigenstates of the TLS. With the dipole transition matrix element $M_{ij} = \langle i|\vec{\sigma}|j\rangle$ and $\sigma_{ij} = |j\rangle\langle j|$ one finds

$$\vec{\mu} = -\frac{g_{\mathrm{e}}\mu_{\mathrm{B}}}{\hbar} \sum_{ij} M_{ij}\sigma_{ij} \tag{2.43}$$

With the quantized magnetic field mode $\vec{B_1} = -iB_1\left(a - a^\dagger\right)\vec{e}_y$ derived from Eq. (2.31), the interaction Hamiltonian reads

$$\begin{aligned}\mathcal{H}_{\text{int}} &= i\frac{g_{\text{e}}\mu_{\text{B}}}{\hbar}B_1\sum_{ij}M_{ij}\sigma_{ij}\left(a - a^\dagger\right)\vec{e}_y \\ &= \hbar g_0\left(\sigma_+ + \sigma_-\right)\left(a + a^\dagger\right).\end{aligned} \tag{2.44}$$

Here, we have introduced the single-spin coupling rate $g_0 = i\frac{g_{\text{e}}\mu_{\text{B}}}{\hbar^2}B_1$ $M_{ij}\vec{e}_y$ and the spin raising- and lowering operators $\sigma_\pm = \sigma_{\text{x}} \pm \sigma_{\text{y}}$, which allow to create (σ_{x}) and destroy (σ_-) spin excitations. In a last step, the counter-rotating terms $\sigma_- a$ and $\sigma_+ a^\dagger$ in Eq. (2.44) are dropped in the so-called rotating-wave approximation (RWA) and we obtain the Jaynes-Cummings Hamiltonian

$$\mathcal{H}_{\text{JC}} = \hbar\omega_{\text{r}}a^\dagger a + \frac{1}{2}\hbar\omega_{\text{s}}\sigma_{\text{z}} + \hbar g_0\left(\sigma_+ a - \sigma_- a^\dagger\right). \tag{2.45}$$

The expression for g_0 can be further simplified by evaluating the transition matrix element M_{ij} using the known commutator relations:

$$\begin{aligned}M_{ih} &= \langle i|\vec{\sigma}|j\rangle\vec{e}_y = \langle i|\sigma_{\text{y}}|j\rangle \\ &= \frac{1}{2i}\langle i|\sigma_+ - \sigma_-|j\rangle = -\frac{\hbar}{2i}.\end{aligned} \tag{2.46}$$

The magnetic field amplitude B_1 is normalized to the ground state energy (vacuum fluctuations) inside the resonator mode volume V_{m} [33, 107]:

$$\frac{1}{2}\frac{\hbar\omega_{\text{r}}}{2} = \frac{1}{2\mu_0}\int_{V_{\text{m}}} B_1^2\,\mathrm{d}V = \frac{1}{2\mu_0}B_1^2 V_{\text{m}}, \tag{2.47}$$

$$\Rightarrow \quad B_1 = \sqrt{\frac{\mu_0\hbar\omega_{\text{r}}}{2V_{\text{m}}}}. \tag{2.48}$$

We introduce an additional factor of $1/2$ on the left-hand side, as only half of the energy is stored in the magnetic field mode. Additionally, we assume a constant magnetic field in the vicinity of the spin under investigation, as the microwave wavelength is much longer than the Bohr radius of the phosphorus donor atom. With this, we obtain for the single-spin coupling rate:

$$g_0 = \frac{g_\mathrm{e}\mu_\mathrm{B}}{2\hbar}\sqrt{\frac{\mu_0\hbar\omega_\mathrm{r}}{2V_\mathrm{m}}}. \tag{2.49}$$

When we limit the discussion to the case that there are zero or one photon in the resonator, the eigenstates of the Jaynes-Cummings Hamiltonian can be found by writing Eq. (2.45) in matrix form [111]:

$$\mathcal{H}_\mathrm{JC} = \hbar\begin{pmatrix}\omega_\mathrm{s} & g_0\\ g_0 & \omega_\mathrm{r}\end{pmatrix}. \tag{2.50}$$

After solving the eigenvalue problem $\mathcal{H}_\mathrm{JC}|\pm\rangle - \lambda|\pm\rangle = 0$, the eigenenergies of the coupled spin-resonator system can be written as

$$\epsilon_\pm = \frac{\hbar}{2}\left(\omega_\mathrm{r} + \omega_\mathrm{s} \pm \sqrt{4g_0^2 + \Delta^2}\right), \tag{2.51}$$

with the corresponding eigenstates

$$|\pm\rangle = \cos(\theta)|1\uparrow\rangle \pm \sin(\theta)|0\downarrow\rangle. \tag{2.52}$$

Here, $|1\uparrow\rangle$ and $|0\downarrow\rangle$ describe the eigenstates with one photon in the resonator and the spin in the upstate or no photon in the resonator and the spin in the downstate. $\Delta = \omega_\mathrm{s} - \omega_\mathrm{r}$ is the resonator-spin detuning. The eigenstates are superpositions of the resonator and spin eigenstates, where $\theta = \arctan(g_0/\Delta)$ is the mixing angle between the photon and spin state. These eigenstates are also known as *dressed states* or *polariton modes*. We plot the solution of the Jaynes-Cummings model in Fig. 2.7. The dashed lines show the undisturbed resonator and spin dispersion. The two polariton modes exhibit an avoided crossing on

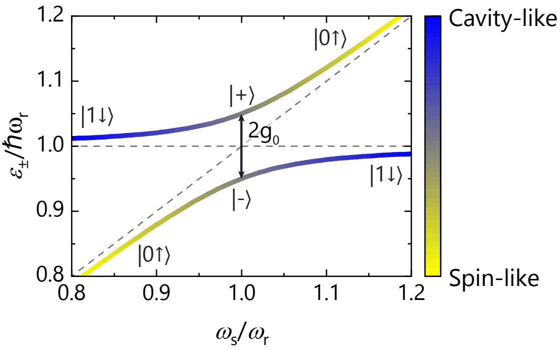

Fig. 2.7 Energy eigenstates of the Jaynes-Cummings Hamiltonian describing the coupled spin-resonator system. The color gradient indicates if the eigenstate is spin-like (yellow) or resonator-like (blue). On resonance $\omega_r = \omega_s$ the system hybridizes to the polariton modes $|\pm\rangle$, an equal superposition of the spin and resonator eigenstates.

resonance and are split by $2g_0$. The color gradient indicates whether the polariton mode is more spin-like (yellow) or cavity-like (blue).

The resonator and spin ensemble loss rates can be taken into account by making ω_s and ω_r complex quantities [107, 112]:

$$\omega_s \mapsto \omega_s - i\gamma_s, \quad \omega_r \mapsto \omega_r - i\kappa_c. \tag{2.53}$$

The loss rate Γ of the coupled system is given by the imaginary part of the eigenenergy and reads

$$\Gamma = \frac{\gamma_s + \kappa_c \pm \mathrm{Re}\left(\sqrt{(\gamma_s - \kappa_c)^2 - 4g_0^2}\right)}{2}. \tag{2.54}$$

On resonance, the total loss rate is given by $\Gamma = \frac{\kappa_c + \gamma_s}{2}$.

We can now distinguish two regimes, depending on the ratio between the coupling rate g_0 and the loss rates κ_c, γ_s:

- *Weak coupling regime*: For $g_0 \ll \kappa_\mathrm{c}, \gamma_\mathrm{s}$, the resonator-spin interaction is smaller than the individual loss rates of the system. An avoided crossing is not visible, but the resonator transmission dip can be smeared out. This is the usual regime in conventional ESR spectroscopy.
- *Strong coupling regime*: For $g_0 \gg \kappa_\mathrm{c} + \gamma_\mathrm{s}$, the transition from the weak to the strong coupling regime occurs. Here, the interaction between the spin and the resonator is not negligible anymore and a normal mode splitting or avoided crossing is observed. A figure of merit is the cooperativity, $C = \frac{g_0^2}{\kappa_\mathrm{c}+\gamma_\mathrm{s}}$ with $C \gg 1$ in the strong coupling regime.

In this thesis, we use microwave resonators with a frequency in the order of 5 GHz. The electromagnetic mode extends in a volume of approx. $1.5 \times 10^7\,\mu\mathrm{m}^{-3}$ (see Sec. 4.3). With this, we can calculate the single-spin coupling rate according to Eq. (2.49) and find $g_0 \approx 30\,\mathrm{Hz}$ [113, 114]. Using specialized microwave resonator structures, single-spin coupling rates in the order of 150 Hz are possible[49, 50]. When comparing these values to the usual loss rates of the resonator and the spin ensemble in the order of several 100 kHz, it is clear that the strong coupling regime is out of reach. It is, however, possible to reach the strong coupling regime by exploiting collective effects in an ensemble of spins.

2.3.3 The Tavis-Cummings model and collective effects

So far, we have discussed the interaction between a single spin 1/2 particle and the magnetic field generated by a microwave resonator on the basis of the Jaynes-Cummings model. However, in an ensemble of two-level systems, collective effects occur. Robert Henry Dicke discovered, that an ensemble of two-level emitters coupled to a common radiation field, can spontaneously emit radiation with a larger intensity than the individual emitters due to collective effects [70]. Vice versa, we can make use of collective effects to increase the spin-resonator coupling.

An extension to the Jaynes-Cummings model for an ensemble of N spins was given by Tavis and is therefore called the Tavis-Cummings model [115]. In the case of a spin ensemble coupling to a resonator, additional eigenstates are created. These eigenstates can be divided in two groups, called "bright" and "dark" or "superradiant" and "subradiant", respectively, indicating their interaction strength with the resonator [104].

In a simple approach, we assume that all spins have the same transition energy ω_s and that dipole-dipole interactions between spins are negligible. The Tavis-Cummings Hamiltonian can then be written as [116]

$$\mathcal{H}_\mathrm{TC} = \hbar\omega_\mathrm{r} a^\dagger a + \frac{1}{2}\hbar\omega_\mathrm{s}\sum_{i=1}^{N}\sigma_\mathrm{z}^i + \hbar\sum_{i=1}^{N} g_0^i\left(\sigma_+ a - \sigma_- a^\dagger\right). \tag{2.55}$$

This expression can be further simplified by introducing collective spin operators [117]

$$J_z = \frac{1}{2}\sum_{i=1}^{N}\sigma_\mathrm{z}^i \text{ and } J_\pm = \sum_{i=1}^{N}\sigma_\pm^i, \tag{2.56}$$

and we obtain

$$\mathcal{H}_\mathrm{TC} = \hbar\omega_\mathrm{r} a^\dagger a + \hbar\omega_\mathrm{s} J_z + \hbar\sum_{i=1}^{N} g_0^i\left(\sigma_+ a - \sigma_- a^\dagger\right). \tag{2.57}$$

The collective spin operators behave like the standard angular momentum operators. Defining $\vec{J} = (J_x, J_y, J_z)$ and $J_\pm = (J_x \pm iJ_y)$, we can derive the corresponding eigenstates $|J, M\rangle$ of $\vec{J}^2$ and J_z [117]:

$$\vec{J}^2|J, M\rangle = J(J+1)|J, M\rangle \text{ and } J_z|J, M\rangle = M|J, M\rangle, \tag{2.58}$$

with the cooperation number $J = 0, \dots, \frac{N}{2}$ and the projection number $M = -J, \dots, J$ [70]. These states are also called Dicke states. The interesting states of an ensemble with N spins are the two states, where either all spins are excited ($J = N/2, M = J$) or in the ground state ($J = N/2, M = -J$) [116]: $|E\rangle = |\uparrow, \uparrow, \ldots, \uparrow\rangle$ and $|G\rangle = |\downarrow, \downarrow, \ldots, \downarrow\rangle$. The states in between can be generated by successive application of the ladder operators $J_\pm$ [117]:

$$J_\pm |J, M\rangle = \sqrt{(J \pm M + 1)(J \mp M)}|J, M \pm 1\rangle. \tag{2.59}$$

Assuming that the single-spin coupling rate of the individual spins is equal, $g_0^i = g_0$, we can introduce an effective collective coupling [118]

$$g_\mathrm{eff} = \sqrt{\sum_{i=1}^{N} \left|g_0^i\right|^2} = g_0 \sqrt{N}. \tag{2.60}$$

and obtain finally the Tavis-Cummings Hamiltonian

$$\mathcal{H}_\mathrm{TC} = \hbar\omega_\mathrm{r} a^\dagger a + \hbar\omega_\mathrm{s} J_z + \hbar g_\mathrm{eff} \left(J_+ a - J_- a^\dagger\right). \tag{2.61}$$

Considering Eq. (2.60), it is clear that even with a single-spin resonator coupling $g_0 \approx 30\,\mathrm{Hz}$, collective coupling rates in the order of MHz can be reached by increasing the number of spins in the ensemble.

The Dicke ladder and superradiance

In the following we will consider states with the highest cooperation number $J = N/2$. As discussed above, the ground state is given by $|G\rangle = |J, -J\rangle = |\downarrow, \downarrow, \ldots \downarrow\rangle$. The first excited state is generated by applying the raising operator to $|G\rangle$:

$$\begin{aligned} |B\rangle = |J, -J + 1\rangle = \\ = \frac{1}{\sqrt{N}} \left(|\uparrow, \downarrow, \downarrow, \ldots \downarrow\rangle + |\downarrow, \uparrow, \downarrow, \ldots \downarrow\rangle + |\downarrow, \downarrow, \ldots \uparrow\rangle\right). \end{aligned} \tag{2.62}$$

$|B\rangle$ is a highly symmetric spin state, where the excitation is shared accross all N spins. By subsequently applying the ladder operator, more excitations are introduced and the complete ladder of states, the

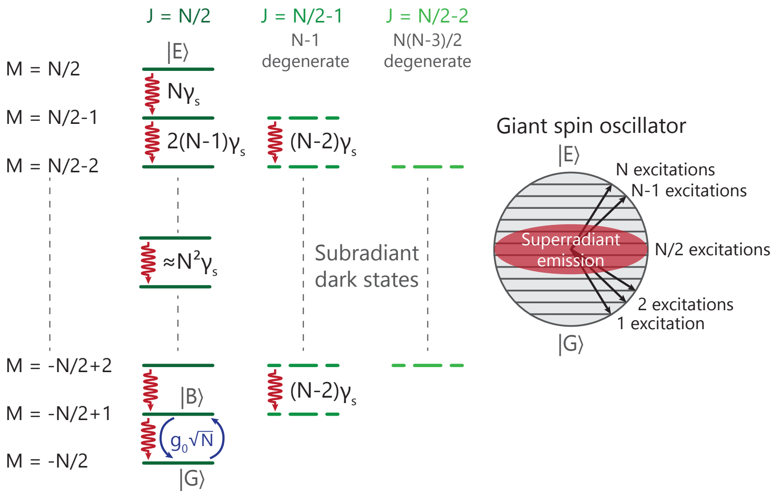

Fig. 2.8 The Dicke ladder for an ensemble of N spins, modeled as a giant spin oscillator with cooperation number $J = N/2$. The giant oscillator spin creates a ladder of symmetric radiant states, which decay with a rate of $N\gamma_\text{s}$ near the ground and excited state, respectively. In the equator region, the decay rate is collectively enhanced and so-called superradiance occurs with a decay rate proportional to $N^2\gamma_\text{s}$. Figure adapted from Ref. [76, 104].

so-called Dicke ladder is obtained (see Fig. 2.8). For large number of spins, the spin ensemble behaves like a harmonic oscillator system termed the *giant spin oscillator* [119]. Besides the states with $J = N/2$, an ensemble of N spin can also be represented by spin states with $J < N/2$, i.e. $J = N/2 - 1, N/2 - 2, \dots$. However, in contrast to the $J = N/2$ states, these states are highly degenerate with their degeneracy given by [70]:

$$\frac{(2J+1)N!}{(N/2+J+1)!(N/2-J)!} \tag{2.63}$$

For example, the states with $J = N/2-1$ have an $(N-1)$-fold degeneracy, the states with $J = N/2 - 2$ are $(N(N-3)/2)$-fold degenerate.

The decay rate between states depends on J and M and is given by [120]

$$\Gamma = \gamma_s \left(J + M\right)\left(J - M + 1\right). \tag{2.64}$$

The decay rates according to Eq. (2.64) are indicated accordingly in Fig. 2.8. Near the excited and ground state, the decay rate scales with $N\gamma_s$. If the giant spin is brought to the equator, where $M \approx N/2$, the decay rate scales accordingly with $\Gamma \approx N^2\gamma_s$. The non-linear dependence of the decay rate on N was termed *superradiance* by Dicke and describes a collectively enhanced spontaneous emission [70].For $J = N/2 - 1$ and smaller J, we obtain the subradiant dark states, which do not couple to the resonator.

In the following, we consider the case where $J = N/2$ and a single excitation is introduced into the system. Then, it can be shown that the ground state $|G\rangle$ is only coupled to the first excited state $|B\rangle$ with the coupling rate $g\sqrt{N}$, while other spin states play no role [117]. Therefore, $|B\rangle$ is called *bright* or *radiant* state. The interaction between the resonator and the spin ensemble will then lead to two polariton modes $|\pm\rangle$ with the expected splitting of $2g_{\mathrm{eff}}$ due to the coupling between $|G\rangle$ and $|B\rangle$. When the number of excitations is increased, more spon-photon states of the $J = N/2$ subspace will participate in the cooperative energy exchange [111].

Low-excitation limit and steady-state transmission

In the case of a spin ensemble coupling to a resonator with only a small number of excitations in the system, the giant spin oscillator can be treated as a simple harmonic oscillator. This "bosonization" approach is known as Holstein-Primakoff transformation [117, 121, 122]. When a spin ensemble is excited by only a small number of excitations, all spins remain more or less in their ground state, as the excitations are shared equally by all spins. Therefore, a single anharmonic spin can be replaced by a harmonic oscillator. It is then possible to map the collective spin operators defined in Eq. (2.56) by bosonic annihilation and creation operators b and $b^\dagger$ as [117]

$$J_+ = b^\dagger\sqrt{1 - b^\dagger b} \text{ and } J_z = 2b^\dagger b - 1. \tag{2.65}$$

Accordingly, the Tavis-Cummings Hamiltonian (2.61) can be rewritten as

$$\mathcal{H}_{\mathrm{TC}} = \hbar\omega_{\mathrm{r}} a^\dagger a + \hbar\omega_{\mathrm{s}} b^\dagger b + \hbar g_{\mathrm{eff}}\left(ab^\dagger + a^\dagger b\right). \tag{2.66}$$

We can now derive the steady-state transmission spectrum for the low-excitation case. The Heisenberg equations for the resonator and spin ensemble operators are given by [123]

$$\dot{a} = \frac{i}{\hbar}\left[\mathcal{H}_{\mathrm{TC}}, a\right] + \frac{i}{\hbar}\left[\mathcal{H}_{\mathrm{drive}}, a\right] - \kappa_{\mathrm{c}} a \tag{2.67}$$

$$\dot{b} = \frac{i}{\hbar}\left[\mathcal{H}_{\mathrm{TC}}, b\right] - \gamma_{\mathrm{s}} b. \tag{2.68}$$

In Eq. (2.67) we considered an additional weak driving field with frequency ω and amplitude c_{in}, which is used to probe the microwave resonator. We now make the transition to the rotating frame of reference, rotating with the probe tone frequency ω. In this rotating frame, the Hamiltonians are given by

$$\mathcal{H}_{\mathrm{TC}} = \hbar\Delta_{\mathrm{r}} a^\dagger a + \hbar\Delta_{\mathrm{s}} b^\dagger b + \hbar g_{\mathrm{eff}}\left(ab^\dagger + a^\dagger b\right), \tag{2.69}$$

$$\mathcal{H}_{\mathrm{drive}} = -i\hbar c_{\mathrm{in}}\left(a - a^\dagger\right), \tag{2.70}$$

where we introduced the resonator detuning $\Delta_{\mathrm{r}} = \omega_{\mathrm{r}} - \omega$ and the spin detuning $\Delta_{\mathrm{s}} = \omega_{\mathrm{s}} - \omega$. Evaluating Eq. (2.67) and (2.68) results in two coupled linear differential equations in the rotating frame [109]:

$$\dot{a} = (i\Delta_{\mathrm{r}} - \kappa_{\mathrm{c}})a + ig_{\mathrm{eff}} b + \sqrt{\kappa_{\mathrm{ext}}} c_{\mathrm{in}} + f_a, \tag{2.71}$$

$$\dot{b} = (i\Delta_{\mathrm{s}} - \gamma_{\mathrm{s}})b + ig_{\mathrm{eff}} a + f_b, \tag{2.72}$$

where we introduced the noise operators f_a, f_b, which conserve the commutator relations [109]. In the following, we focus on the classical

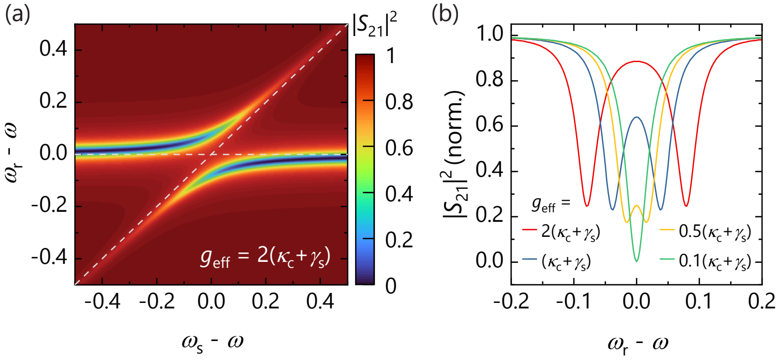

Fig. 2.9 (a) Steady-state transmission spectrum for a spin ensemble coupled to a microwave cavity. When the spin ensemble is resonantly coupled to the microwave resonator, an avoided crossing with a splitting of $2g_{\mathrm{eff}}$ can be observed. (b) Transmission spectrum for $\omega = \omega_{\mathrm{s}}$ for different values of the collective coupling rate g_{eff}. The normal mode splitting decreases with g_{eff}. For $g_{\mathrm{eff}} = 0.5(\kappa_{\mathrm{c}} + \gamma_{\mathrm{s}})$ the avoided crossing almost disappears.

average quantities, which are obtained by taking the average of Eq. (2.71) and (2.72) [108]. Solving for the steady-state, we note that $\langle f_a \rangle = \langle f_b \rangle = 0$ and we obtain for the average field in the cavity

$$\langle a \rangle_{\mathrm{st}} = -\frac{\sqrt{\kappa_{\mathrm{ext}}}\,c_{\mathrm{in}}}{i\Delta_{\mathrm{r}} - \kappa_{\mathrm{c}} + \frac{g_{\mathrm{eff}}^2}{i\Delta_{\mathrm{s}} - \gamma_{\mathrm{s}}}}. \tag{2.73}$$

Analogously to Eq. (2.37), we can calculate the microwave transmission by relating the input and the output field:

$$|S_{21}|^2 = \left|\frac{c_{\mathrm{out}}}{c_{\mathrm{in}}}\right|^2 = \left|1 + \frac{\sqrt{\kappa_{\mathrm{ext}}}}{i\Delta_{\mathrm{r}} - \kappa_{\mathrm{c}} + \frac{g_{\mathrm{eff}}^2}{i\Delta_{\mathrm{s}} - \gamma_{\mathrm{s}}}}\right|^2. \tag{2.74}$$

We calculate the steady-state transmission spectrum for a spin ensemble coupled to a microwave resonator and plot the result in Fig. 2.9 (a). We choose $\kappa_{\mathrm{ext}} = 0.5\kappa_{\mathrm{c}}$ and set the effective coupling rate to $g_{\mathrm{eff}} =$

$2(\kappa_\mathrm{c} + \gamma_\mathrm{s})$. When the spin ensemble is far detuned from the resonator, the calculated transmission spectrum corresponds to the transmission spectrum of the microwave resonator, i.e. a transmission dip at the resonance frequency of the resonator. When the spin system is on resonance with the resonator, we observe an avoided crossing. The splitting between the two polariton modes corresponds now to $2g_\mathrm{eff}$. We plot the transmission spectrum as a function of Δ_r for several values of g_eff in Fig. 2.9 (b). Here, the normal mode splitting decreases with the collective coupling rate. For $g_\mathrm{eff} = 0.5(\kappa_\mathrm{c} + \gamma_\mathrm{s})$, the avoided crossing almost disappears. For g_eff even smaller, the bare resonator transmission is observed gain.

CHAPTER 3

TECHNICAL IMPLEMENTATION

In the last chapter, we introduced the fundamental principles of electron spin resonance (ESR). In this section, we will explain the actual technical implementation of continuous-wave and pulsed ESR spectroscopy in the course of this thesis. We start with a short digression and give details about the sample preparation in Section 3.1, including the thin-film process, the Si:P crystal preparation as well as mounting the sample in the sample holder. We then continue with the microwave circuitry comprising the ESR spectrometer. In Section 3.2, we explain the inner workings of the pulsed ESR setup, which was designed and built in the course of this thesis. In Section 3.3, we explain the cryogenic microwave circuitry of the two experimental setups we used. Finally, we show characterization measurements in Section 3.4, where we verify the correct operation of the ESR spectrometer.

3.1 Sample preparation

In this thesis, we used three different samples consisting of a silicon chip containing several superconducting microwave resonators and a spin ensemble in a silicon host crystal, which is mounted in a flip-chip configuration on the microwave resonators. An overview of the different samples is given in Appendix A1.

The superconducting microwave resonators are fabricated on top of a $6 \times 10\,\mathrm{mm}^2$ high resistivity ($> 10\,\mathrm{k\Omega cm}$) silicon substrate with natural isotope composition. The substrate is cleaned from a protective resist layer in an ultrasonic bath using acetone and isopropyl alcohol. Following the cleaning procedure, a 150 nm thick niobium layer is deposited onto the substrate in a sputter process. For the resonators measured in Chapter 4 (Sample #1), an additional 10 nm aluminium capping layer is deposited on top of the niobium to prevent oxidation of the niobium.

Next, the chip is spin coated with photo resist and the resonator structure is defined either via optical (Sample #2) or electron beam lithography (Sample #1 and #3). After development, the structure is patterned into the superconducting film using a reactive ion etching (RIE) process. For Sample #1, the Al capping layer is removed by argon ion milling and chemical wet etching before the RIE step (for more details refer to Ref. [124]).

After fabrication of the microwave resonators, the chip is placed in a gold-plated copper box. A fotograph of the sample box with a mounted resonator chip is displayed in Fig. 3.1. The resonator is fixed with conductive silver glue around the edges, which at the same time forms the ground connection of the microwave resonator. SMA end launch connectors are then inserted from both ends, so that the center pin of the end launch can be connected to the coplanar waveguide using silver glue.

In Sec. 4, we investigate a phosphorus spin ensemble hosted in a Si crystal with natural isotope composition (Sample #1). The doping concentration is $[\mathrm{P}] = 2 \times 10^{17}\,\mathrm{cm}^{-3}$. The residual $^{29}\mathrm{Si}$ concentration is given by the natural abundance and is approx. 4.7 % [125]. The crystal has dimensions of $3.4\,\mathrm{mm} \times 3.4\,\mathrm{mm} \times 0.42\,\mathrm{mm}$ and is placed on top of

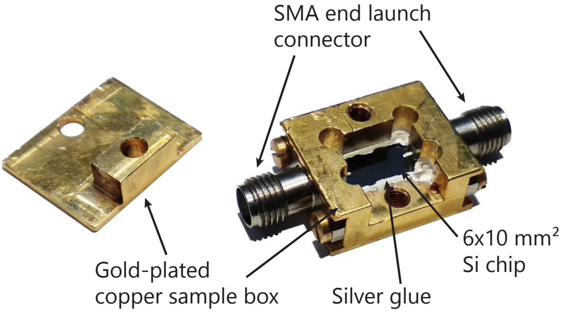

Fig. 3.1 Fotograph of the gold-plated copper sample box with a mounted resonator sample. The Si resonator chip is placed in the sample box and fixed in place with conductive silver glue. SMA end launch connectors are inserted from both ends and the center conductors are connected to the signal line of the coplanar feedline using silver glue.

the microwave resonator. It is pressed down using an copper screw, which is mounted in the lid of the sample box.

In Sec. 5, we investigate a phosphorus spin ensemble hosted in an isotopically purified ^{28}Si crystal with a donor concentration of $[\mathrm{P}] = 1 \times 10^{17}\,\mathrm{cm}^{-3}$ (Sample #2 and #3). The residual ^{29}Si concentration is 0.1 %. The ^{28}Si:P crystal has a thickness of 20 µm and was originally grown on top of a heavily boron-doped $^{\mathrm{nat}}$Si substrate ($[\mathrm{B}] = 4.5 \times 10^{19}\,\mathrm{cm}^{-3}$). An additional 500 nm thick arsenic doped $^{\mathrm{nat}}$Si layer ($[\mathrm{As}] = 4.5 \times 10^{19}\,\mathrm{cm}^{-3}$) was grown on top of the ^{28}Si:P layer. This structure effectively forms a $p^{+}n^{-}n^{+}$ diode and was used to study the influence of the Stark shift on the hyperfine interaction of the phosphorus donors [126].

The arsenic and boron doping concentration are above the metal-insulator transition and lead to a large conductivity of the silicon crystal, even at millikelvin temperatures [127]. Conductive materials in the vicinity of a superconducting microwave resonator result in significant losses due to induced eddy currents [128]. Therefore, we remove both layers enclosing the ^{28}Si:P crystal. The Si:As capping layer is removed by reactive ion etching. Afterwards, the bulk of the Si:B substrate is removed by mechanical polishing until a sample thickness of approx. 80 μm is obtained. The rest of the Si:B substrate is then again removed by reactive ion etching. The resulting 20 μm thin ^{28}Si:P flakes are then placed on top of the microwave resonator and pressed down using an additional piece of a $^{\mathrm{nat}}$Si wafer and a PTFE screw in the lid of the sample box.

3.2 Phase-sensitive microwave generation and detection

In the following, we present our measurement setup for continuous-wave and pulsed ESR spectroscopy. We implement phase-sensitive pulse generation based on an arbitrary waveform generator (AWG) and a heterodyne signal detection using a fast analog-to-digital converter (ADC). Additionally, using electro-mechanic latching switches, our setup allows to quickly switch between pulsed ESR and continuous-wave ESR experiments using a vector network analyzer (VNA). Similar AWG based pulsed ESR spectrometers are described in Ref. [129–131]. In the following we introduce the basics of IQ modulation, which is at the heart of our pulse generation and microwave detection.

3.2.1 Basics of IQ modulation

This section follows Ref. [132]. The microwave pulses generated by the measurement setup have a bandwidth of several megahertz and frequencies in the gigahertz regime. This type of signal is known as a passband signal s_p defined as

$$s_\mathrm{p}(t) = \sqrt{2}\left(A_\mathrm{I}(t)\cos\left(\omega_\mathrm{c}t\right) - A_\mathrm{Q}(t)\sin\left(\omega_\mathrm{c}t\right)\right), \tag{3.1}$$

where the real-valued functions $A_\mathrm{I}(t)$ and $A_\mathrm{Q}(t)$ are the *in-phase* and *quadrature* component of the signal. The carrier frequency ω_c typically lies in the center of the passband signal. Such a real-valued passband is equivalent to a complex baseband signal, defined as

$$s(t) = A_{\mathrm{I}}(t) + iA_{\mathrm{Q}}(t), \tag{3.2}$$

such that the relationship between the passband and complex baseband can be written as

$$s_{\mathrm{p}}(t) = \mathrm{Re}\left(\sqrt{2}s(t)e^{i\omega_{\mathrm{c}}t}\right). \tag{3.3}$$

Note that all information of this signal is contained in the complex baseband signal $s(t)$, centered around $\omega = 0$. Therefore, we can limit the treatment of the microwave pulses to the complex baseband.

We will later investigate the amplitude $A(t)$ and phase $\phi(t)$ of the generated microwave pulses, which are related to the complex baseband by the following relations:

$$A(t) = \sqrt{A_{\mathrm{I}}(t)^2 + A_{\mathrm{Q}}(t)^2}, \tag{3.4}$$

$$\phi(t) = \arctan\left(\frac{A_{\mathrm{I}}(t)}{A_{\mathrm{Q}}(t)}\right), \tag{3.5}$$

$$A_{\mathrm{I}}(t) = A(t)\cos\phi(t), \tag{3.6}$$

$$\text{and } A_{\mathrm{Q}}(t) = A(t)\sin\phi(t). \tag{3.7}$$

Frequency upconversion is achieved by multiplying the complex baseband signal with the carrier signal, as defined in Eq. 3.1. To downconvert a passband signal back to baseband, one multiplies the passband signal with the carrier signal and filters out frequency components at

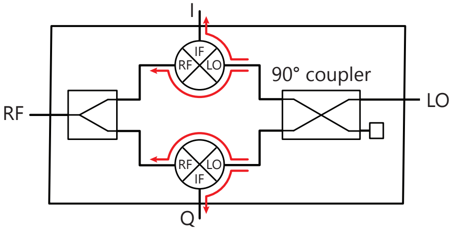

Fig. 3.2 Schematic drawing of an IQ mixer. RF signals entering the IQ mixer are split using a power divider. The signal is downconverted using two mixers, where the local oscillator of one of the mixers is shifted by 90° by a 90° coupler. The red arrows indicate leakthrough of the LO signal to the I, Q and RF ports.

$2\omega_\mathrm{c}$ using a lowpass filter:

$$\begin{aligned}\sqrt{2}s_\mathrm{p}(t)\cos(\omega_\mathrm{c}t) &= 2I(t)\cos^2(\omega_\mathrm{c}t) - 2A_\mathrm{Q}(t)\sin(\omega_\mathrm{c}t)\cos(\omega_\mathrm{c}t) \qquad (3.8)\\ &= A_\mathrm{I}(t) + A_\mathrm{I}(t)\cos(2\omega_\mathrm{c}t) - A_\mathrm{Q}(t)\sin(2\omega_\mathrm{c}t)\\ &\approx A_\mathrm{I}(t),\\ \sqrt{2}s_\mathrm{p}(t)\sin(\omega_\mathrm{c}t) &= 2I(t)\cos(\omega_\mathrm{c}t)\sin(\omega_\mathrm{c}t) - 2A_\mathrm{Q}(t)\sin^2(\omega_\mathrm{c}t) \qquad (3.9)\\ &= A_\mathrm{Q}(t) + A_\mathrm{Q}(t)\cos(2\omega_\mathrm{c}t) - A_\mathrm{I}(t)\sin(2\omega_\mathrm{c}t)\\ &\approx A_\mathrm{Q}(t).\end{aligned}$$

The device performing the frequency up- and downconversion is called IQ mixer. A schematic drawing of an IQ mixer is shown in Fig. 3.2. The carrier signal, here called local oscillator (LO), at frequency ω_LO enters the IQ mixer at the LO port. A 90° coupler is used to generate the sine and cosine carrier term in Eq. (3.8) and (3.9). If a baseband signal is fed into the I and Q port of the device, the two mixers multiply the baseband signal with the LO signal. A power combiner then forms the passband signal by adding the signal of the two mixers. Similarly, the device can be used for downconversion. Here, the RF signal entering the device is split by the power combiner and fed into the two mixers. After multiplication with the LO signal, the two components of the baseband signal can be extracted from the I and Q port. Note that an additional lowpass filter at the I and Q port is necessary to remove components at twice the carrier frequency.

Due to the non-perfect isolation between the ports, signal from the LO port can leak to the other ports (indicated as red arrows in Fig. 3.2). Typical values for the isolation between the LO and IF port are in the order of 20 – 30 dB. This LO leakthrough leads to an additional signal with a frequency ω_{LO} in the upconverted passband signal or a DC component in the downconverted baseband signal, respectively. As an IQ mixer internally uses two separate mixers, runtime differences can lead to a deviation of the 90° phase difference between the I and Q ports. Additionally, the conversion loss of the two mixers can differ, leading to different amplitudes at the I and Q port, respectively. These phase and amplitude imbalances lead to a distortion of the waveform. A good overview of IQ imbalances and their correction can be found in Refs. [133].

To circumvent the issues of LO leakthrough, we use the IQ mixer as a single sideband mixer. We use Eq. (3.6) and (3.7) and set $\phi(t) = \phi_0 + \omega_{\mathrm{IF}} t$. Using Eq. 3.1, we find for the passband signal

$$s_{\mathrm{p}}(t) = A(t) \cos\left((\omega_{\mathrm{LO}} + \omega_{\mathrm{IF}})t + \phi_0\right) . \tag{3.10}$$

The IQ mixer therefore generates a passband signal at a frequency of $\omega_{\mathrm{LO}} + \omega_{\mathrm{IF}}$. Any IQ imbalances will lead to the generation of an unwanted sideband at a frequency of $\omega_{\mathrm{LO}} - \omega_{\mathrm{IF}}$. The baseband signals $A_{\mathrm{I}}(t)$ and $A_{\mathrm{Q}}(t)$ are generated by an arbitrary waveform generator at a fixed intermediate frequency of $\omega_{\mathrm{IF}} = 62.5\,\mathrm{MHz}$. In this configuration, the LO leakthrough at frequency ω_{LO} as well as the unwanted sideband at frequency $\omega_{\mathrm{LO}} - \omega_{\mathrm{IF}}$ are far detuned from the ESR resonance at $\omega_{\mathrm{LO}} + \omega_{\mathrm{IF}}$. Additionally, we assume that the IQ imbalances do not vary a lot over the bandwidth of a pulse. Therefore, we do not employ any correction for IQ imbalances in our measurement setup.

Microwave pulses can be shaped by modulating the envelope $A(t)$ of the pulse. The phase ϕ_0 can be used to shift the phase of individual pulses (see for example Sec. 3.4.3). This allows the generation of arbitrarily shaped microwave pulses, for example to implement adiabatic [134–136] or optimal control pulses [137, 138]. Now that we have introduced the basics of IQ modulation, we present the microwave circuitry used in this thesis in the following.

3.2.2 Overview of the microwave circuitry

The microwave circuitry of our ESR spectrometer is shown in Fig. 3.3. It is similar to other spectrometers based on an arbitrary waveform generator (AWG), see for example Refs. [129–131].

We use an AWG (Keysight M8190A, sample rate set to 8 GS/s) to generate the in-phase and quadrature component of the baseband signal at $\omega_{\mathrm{IF}} = 62.5\,\mathrm{MHz}$. The generated pulses are bandpass filtered (Mini-Circuits SIF-70+, 58 – 82 MHz passband), before being passed to the I and Q port of a vector modulated frequency source (Rhode & Schwarz SGS100A). We use a vector source instead of a discrete IQ mixer, as it internally minimizes IQ imbalances and also offers controllable amplification of the generated RF signal. The upconverted microwave pulses are then amplified using a low-noise high-gain amplifier (Advanced Microwave WPA413PA, 40 dB gain, max. 1 W output power), before entering the cryostat. The microwave signal emerging from the cryostat is then passed into the analog downconversion setup (see next section). Using electromechanical latching switches (Keysight 8765D), we can switch the cryostat input and output between the pulse generation and detection setup and a vector network analyzer (VNA), respectively. We use a VNA (Rhode & Schwarz ZVA8) for continuous-wave microwave transmission measurements.

The LO signal is generated by a signal generator with low phase-noise (Agilent 8257D PSG signal generator). It is further split using a Wilkinson power divider (Marki Microwave PD0220) to provide the

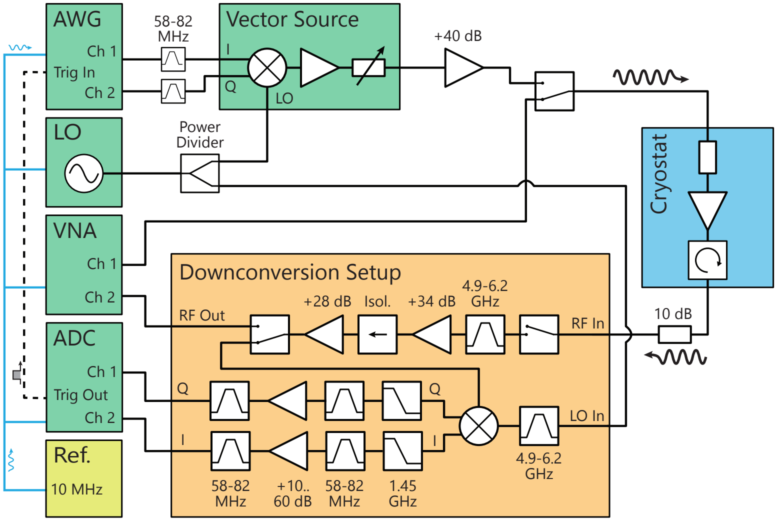

Fig. 3.3 Schematic drawing of the microwave circuitry used in this thesis. A electromechanical latching switch allows to perform either continuous-wave ESR experiment using a vector network analyzer (VNA) or perform downconversion using an IQ mixer. Shaped pulses are generated at an intermediate frequency using an arbitrary waveform generator (AWG). Before entering the cryostat, the pulses are converted to the desired resonance frequency using a vector source. The downconversion box is used to first amplify and then downconvert the low-power signal from the cryostat.

LO signal for both frequency up- and downconversion. The output power of the signal generator is 18 dBm to compensate the insertion loss and power splitting of the power divider in order to obtain a LO power of approx. 13 dBm at the input of the downconversion IQ mixer.

Signal acquisition is initiated by a TTL trigger pulse from the ADC to the AWG. The ADC sends out this trigger pulse as soon as it is in the *armed* state and ready to digitize a signal. This allows an easy integration of signal averaging, as the AWG is automatically triggered for each repetition. To ensure a stable phase relation between all devices, we connect the output of a 10 MHz rubidium frequency standard (Stanford

Research Systems FS725) to the reference clock input of the devices (indicated by a blue line in Fig. 3.3.

The programming of the waveforms and pulse sequences into the AWG is accomplished using a Python software, which was developed during the course of this thesis[1]. It offers a TCP/IP server, such that it can be interfaced with the common LabVIEW measurement software ("Doll Rotate") used at the Walther-Meissner-Institute.

Bandwidth considerations

As can be seen from the schematic diagram above, we use bandpass filters with a passband of 58 – 82 MHz in the IF paths of the setup. Together with the IF frequency of 62.5 MHz, this poses bandwidth limitations on the generated pulse shapes. Microwave pulses with a bandwidth larger than 9 MHz are limited by the bandpass filters ($2 \cdot (62.5\,\mathrm{MHz} - 58\,\mathrm{MHz}) = 9\,\mathrm{MHz}$). In our experiments, we use Gaussian pulses with a pulse length of 1 μs and 2 μs (full width at half maximum), corresponding to pulse bandwidths in the order of 1 – 3 MHz, i.e. well below the bandpass limitation. Moreover, for our measurements, the limiting factor is the bandwidth of the microwave resonator, which is typically in the order of 1 MHz.

3.2.3 Analog downconversion setup

The microwave signals emerging from the cryostat have frequencies in the order of several GHz. As the bandwidth of our digitizer is only 300 MHz, the microwave signals are downconverted to the intermediate frequency using a homebuilt downconversion setup (orange rectangle in Fig. 3.3). To optimize the performance of the downconversion setup and shield it from external microwave noise, the microwave components are placed into a rack-mountable case made from aluminium. The 3 mm thick aluminium bottom plate additionally serves as a heat sink for the microwave amplifiers.

---

[1] The software is available as free software at https://gitlab.com/stwe/awgcontrol.git.

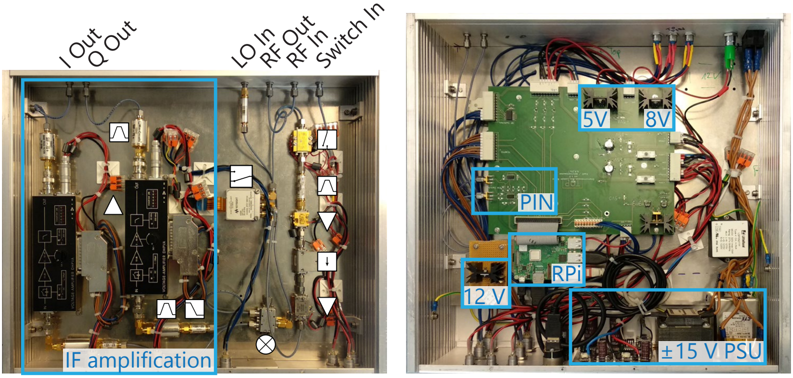

Fig. 3.4 Fotograph of the downconversion setup (left) and electronic control setup (right). Both setups are placed in individual aluminium cases in order to shield them from external microwave noise. A schematic of the downconversion setup is shown in Fig. 3.3. The electronic control setup generates all necessary voltages for the amplifiers and controls the video amplification as well as the PIN and latching electromechanical switches.

Before the signal enters the downconversion box, it passes a 10 dB attenuator to reduce the signal level. This is necessary to avoid driving the microwave amplifiers and IQ mixer into the non-linear regime (see Sec. 3.4.5 for details). The signal then passes through a fast, high-isolation microwave PIN switch (Hittite HMC-C019), which isolates the sensitive microwave amplifiers from the high-energy microwave pulses. Signal is transmitted through the switch only during the time window when an echo signal is expected. This time window is controlled by the sample marker output of one of the AWG channels. To suppress any switching transients, the signal is bandpass filtered (MiniCircuits VBFZ-5500+) before being amplified by two low-noise microwave amplifiers (Agile AMT-0284, 34 dB gain, and AMT-0033, 28 dB gain). An isolator (Ditom D3I4080) is used to suppress any reflections between the two amplifiers. Using an electromechanical switch, the amplified signal is either passed to the input port of the VNA or is further passed into the downconversion part of the microwave circuitry. This way, we can use the room-temperature amplifier chain both for continuous-wave transmission measurements as well as for pulsed measurements.

Following the switch, we use a double-balanced IQ mixer (Marki microwave MLIQ0218L) to downconvert the signal to a complex baseband signal. The LO signal is bandpass filtered (MiniCircuits VBFZ-5500+) before entering the IQ mixer. The resulting IF in-phase and quadrature signals pass through a bandpass filter as well as a lowpass filter (MiniCircuits VLF-1450+) with a cutoff frequency of 1.45 GHz to further suppress LO leakthrough. We use a variable gain voltage amplifier (FEMTO DHPVA-200) with 10 – 60 dB gain and configurable AC/DC coupling to amplify the IF signals to a power level that utilizes the full dynamic range of the ADC. The I and Q signal are then passed to a PCIe digitizer card (Spectrum M4i.4451-x8), where they are digitized with a sample rate of 500 MS/s and a resolution of 14 bit.

In cooperation with C. Kastl, we developed an electronic control circuit based on a Raspberry Pi microcomputer. The control circuit is responsible for the generation of stabilized voltages (5 V, 8 V, 12 V and ±15 V) for the PIN switch and the amplifiers. It further includes a circuit which shifts between the 1.6 V level of the AWG sample marker output and the required 5 V TTL control level of the PIN switch. Additionally, the gain, bandwidth and coupling of the IF amplifiers can be controlled via a digital control interface. The electronic circuit also controls the electromechanical latching switches. The electronic control setup is placed in a separate aluminium case. Front panel buttons allow to switch between pulsed ESR and continuous-wave ESR for hands-on experiments. Both boxes are connected using shielded cables. Fig. 3.4 shows the components of both aluminium cases with schematic symbols and labels. We developed a Python software, running on the Raspberry Pi, which offers a TCP/IP interface to control the switches and IF amplifier settings[2].

---

[2] The software is available as free software at https://gitlab.com/stwe/receiver-box.git.

3.3 Cryogenic microwave setup

The experiments in this thesis are performed at cryogenic temperatures between 50 mK to 10 K in two different setups. The lowest temperatures required for experiments on strongly coupled spin-photon hybrid systems (see Chapter. 5 are obtained using a cryogen-free dilution refrigerator. The measurements presented in Chapter 4 are obtained in a helium gas-flow cryostat, which allows to control the temperatures in a range of 1.5 – 300 K.

Cooling down the samples is required to operate our microwave resonators in the superconducting state. At the same time, reducing the temperature of the spin ensemble increases the thermal spin polarization and leads to an increase of the signal strength. Additionally, when cooling samples to temperatures in the order of millikelvin, the thermal energy is less than the ground state energy of the microwave resonator and the spin ensemble,

$$k_{\mathrm{B}}T < \hbar\omega_{\mathrm{r}}, g_{\mathrm{e}}\mu_{\mathrm{B}}B_0. \tag{3.11}$$

This allows to perform measurements with both the resonator and the spin ensemble in their quantum mechanical groundstate. However, extra care must be taken to shield the sample from thermal microwave noise from the room temperature microwave setup. In the following, we describe the cryogenic microwave circuitry in both measurement setups.

3.3.1 Dilution refrigerator setup

We use a dilution refrigerator (Oxford Triton 400) to cool the samples to a temperature in the range of 50 – 850 mK. The system is based on a cryogen-free pulse-tube cooler, which pre-cools a dilution unit to 3.5 K. A closed ^{3}He/^{4}He cycle then allows to continuously cool the sample stage to a base temperature of 50 mK. We show a fotograph of the dilution refrigerator in Fig. 3.5 (a) (fotograph taken by C. Zollitsch [139]).

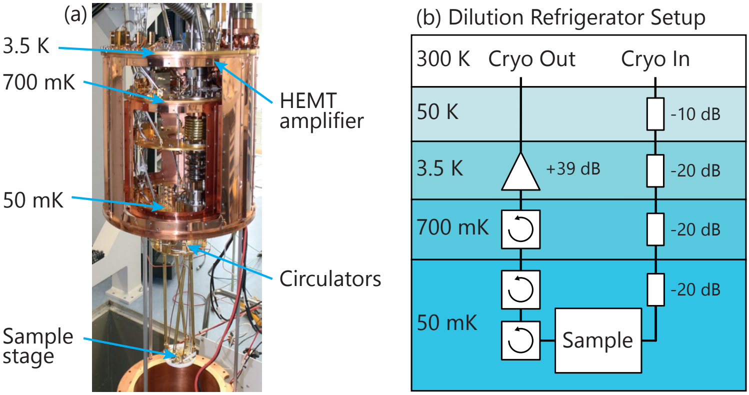

Fig. 3.5 (a) Fotograph and (b) schematic drawing of the dilution refrigerator setup used in this work. In the dilution refrigerator setup the sample is cooled to a base temperature of 50 mK. The microwave input line is attenuated by 70 dB to shield the sample from the microwave noise created by the room-temperature microwave circuitry. The output line is shielded from the microwave noise of the HEMT amplifier at the PT1 stage using cryogenic circulators on the still and mixing chamber stage. The fotograph of the cryostat has been taken by C. Zollitsch [139].

More details on the dilution refrigeration process can be found in Ref. [140].

The cryostat contains a three-dimensional superconducting vector magnetic. A large solenoid with a maximum field of 6 T along the vertical direction and two smaller Helmholtz coil pairs with a maximum field of 1 T can be used to apply a magnetic field in an arbitrary spatial direction. We mount the sample box containing the microwave resonator and the ^{28}Si:P spin sample in the center of the magnetic field. To ensure a good thermalization we connect the sample to the mixing chamber plate with silver wire.

We show the microwave setup inside the dilution refrigerator in Fig. 3.5 (b). Inside the cryostat, microwave components are mounted at the different temperature stages. For our experiments, we use two coaxial microwave cables for signal input and output. The input line is attenuated by a total of 70 dB at the various temperature stages. The attenuators are connected rigidly to the various temperature stages to ensure a proper thermal anchoring. This effectively reduces the incoming room temperature microwave noise photons impinging on the resonator to ≈ 0.01, assuming a resonator bandwidth of 10 MHz at a frequency of 5 GHz [141]. Note that the attenuation is distributed along the different temperature stages, as the cooling power decreases for lower temperatures.

At the output side of the sample box, we are not able to use attenuators to shield the sample from the noise output line, as we do not want to attenuate the low-power signals emerging from the sample box. Here, we use cryogenic circulators (Quin Star Technology CTH04080KCS) to achieve the same goal. The circulators are connected in such a way that the low-power signal from the sample can pass through, but incoming noise from temperature stages above are absorbed by thermally-anchored 50 Ω terminators. At the 3.5 K stage, we use a low-noise high-electron mobility transistor (HEMT) amplifier (Low Noise Factory LNC4_8A) to amplify the signal. The amplifier has a gain of 39 dB with a noise temperature of only 2 K. From the output of the cryostat the signals are then passed to the analog downconversion setup.

3.3.2 Helium gas-flow cryostat with variable temperature insert

Measurements at higher temperatures in the order of $1.5-10$ K are performed in a helium gas-flow cryostat equipped with a superconducting solenoid. The sample is mounted at the cold end of a cryostat dip stick and is inserted into a variable temperature insert (VTI). By reducing the pressure in the VTI, temperatures down to 1.5 K can be reached. The bottom part of the dip stick with the mounted sample is shown in Fig. 3.6 (a). By controlling the helium gas flow as well as the power of a heater mounted on the dipstick, the temperature of the

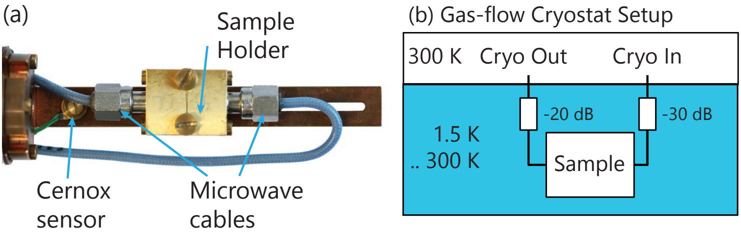

Fig. 3.6 (a) Fotograph of the bottom end of the cryostat dip stick. The sample is connected using blue Minibend cables. A Cernox sensor and a heater (not shown) is used for temperature control of the sample. (b) Microwave circuitry inside the gas-flow cryostat. We place attenuators with 30 dB and 20 dB in the output and input microwave path to reduce thermal microwave noise on the sample.

dip stick can be precisely controlled. Note that there might be a slight deviation of the sample temperature and the dip stick temperature, as the Cernox sensor is mounted at a distance of $\approx 2\,$cm to the sample. More details about the dip-stick can be found in Ref. [142].

Due to space constraints it is not possible to install a cryogenic amplifier in the flow cryostat setup. Additionally, the use of circulators is not possible due to the large magnetic field applied in the vertical direction. In order to shield the sample from room temperature microwave noise and avoid saturation of the ESR line, we insert microwave attenuators with an attenuation factor of 30 dB and 20 dB in the input and output microwave path.

3.4 Spectrometer characterization

In the following, we present characterization and calibration measurements of the spectrometer. In particular, we show how we analyze microwave transmission measurements of the resonator as well as measurements regarding the microwave pulse generation and detection. We also discuss how to calibrate the pulse duration of the pulses in a spin echo sequence.

3.4.1 Transmission calibration and resonator fitting

Before performing any pulsed ESR measurement, it is first necessary to determine the resonance frequency of the microwave resonator as well as identifying the ESR transitions at a given magnetic field. Both of these goals are achieved using continuous-wave measurements using a VNA. The VNA sends out a microwave probe signal and phase-sensitively detects the transmitted signal. The result of this measurement is the so-called scattering parameter S_{21}, which is a complex quantity.

The analysis of the resonator transmission is based on Ref. [143] and [144]. For our resonators, we use a *notch-type* geometry, where a resonator is coupled capacitively or inductively to a microwave transmission line. When measuring the transmission S_{21}, the resonator is visible as a dip in the spectrum. We show the magnitude as well as the phase S_{21} of a exemplary dataset in Fig. 3.7 (a) and (c), respectively. The measurement was conducted in the dilution refrigerator cryostat at $T = 50\,\mathrm{mK}$. From this measurement, it is possible to extract both the resonance frequency and the quality factor (half-width at half maximum) of the resonator. Additionally, it is possible to determine the internal as well as the external or coupling quality factor (see Sec. 4.1 for more details).

The line shape of a notch-type resonator can be asymmetric due to impedance mismatches in proximity of the resonator [143]. Another way to visualize this is that the asymmetry stems from interference between the microwave signal from the transmission line and the microwave signal emerging from the microwave resonator [139]. This asymmetry is taken into account by assuming a complex external quality factor, which describes the coupling,

$$Q_{\mathrm{ext}} = |Q_{\mathrm{ext}}| e^{-i\phi}, \tag{3.12}$$

where ϕ is a measure of the impedance mismatch.

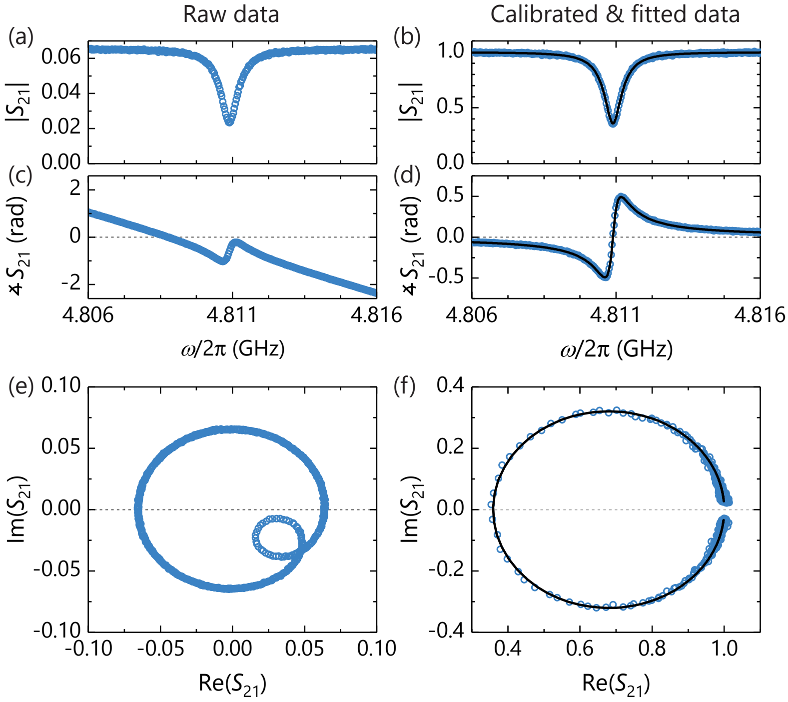

Fig. 3.7 Resonator fitting procedure using an exemplary dataset of a microwave resonator. (a), (c) and (e) show the magnitude, phase and IQ-diagram of the measured raw data. Additional phase shift due to the measurement setup and the finite length of the cables lead to a distortion of the ideal resonance circle. Panel (b), (d) and (f) show the calibrated microwave transmission (data points), where the cable delay has been removed. The solid black line is a fit of Eq. (3.13) to the data. For more details see text.

In general, the complex S_{21} scattering parameter of a notch-type resonator is given by [144]

$$S_{21}(\omega) = a_0 e^{i\alpha} e^{-i\omega\tau} \left(1 - \frac{(Q/|Q_{\mathrm{ext}}|)e^{i\phi}}{1 + 2iQ\left(\omega/\omega_{\mathrm{r}} - 1\right)}\right). \tag{3.13}$$

Here, the second term describes an ideal resonator with resonance frequency ω_{r}, a total quality factor Q, the external quality factor $|Q_{\mathrm{ext}}|$ as well as an impedance mismatch quantified by ϕ.

The first term describes all contributions of the environment of the resonator by introducing three additional parameters. The amplitude factor a_0 and phase shift α describe additional attenuation or gain as well as phase shifts due to the measurement setup. The electronic delay τ is caused by the finite length of the cables and introduces an additional, frequency-dependent phase shift. This phase shift causes a distortion of the ideal resonance circle when the data is plotted in the IQ phase space, as can be seen in Fig. 3.7 (e).

Probst et al. [144] describe a fitting routine which allows to remove the cable delay. Fig. 3.7 (b), (d) and (f) show the magnitude and phase as well as the IQ phase space of the microwave transmission after removal of the electronic delay. In particular, the ideal resonance circle is obtained again (panel (f)). The solid black line shows a fit of Eq. (3.13). From this fit, we can determine the resonance frequency as well as the quality factors of the microwave resonator.

3.4.2 Digital downconversion

Using the setup described above, we digitize the signal at an intermediate frequency $\omega_{\mathrm{IF}} = 62.5\,\mathrm{MHz}$. After digitalization, the microwave signals are downconverted from the IF frequency to a baseband signal at $\omega = 0$ using digital downconversion. We first calculate the complex signal $s_{\mathrm{IF}} = A_{\mathrm{I}}(t) + iA_{\mathrm{Q}}(t)$ and then multiply by a complex sinusoidal to downconvert to the baseband:

$$s(t) = s_{\mathrm{IF}}(t) \cdot e^{i(\omega_{\mathrm{IF}} t + \phi_{\mathrm{rec}})}, \tag{3.14}$$

where ϕ_{rec} is the so-called receiver phase. In a simple way, changing ϕ_{rec} allows to shift the spin echo response to either one of the two quadratures. We will discuss below how to determine the optimal receiver phase.

After downconversion, we apply a lowpass filter (digital Butterworth filter of 5th order) with a cutoff frequency of 10 MHz. As the microwave resonators used in this thesis typically have a linewidth in the order of 1 MHz, we do not loose any information by that operation. Furthermore, this allows to re-sample the signal at a sample rate of 20 MS/s (i.e. twice the lowpass frequency to fulfill the Nyquist-Shannon theorem) to reduce the file size of the measured signals.

The receiver phase depends on possible phase deviations of the IQ mixer as well as a frequency-dependent phase shift due to the finite cable lengths. It is therefore necessary to find the correct receiver phase when changing the microwave pulse frequency. To perform this calibration, we apply a microwave signal with the desired frequency and record both quadratures. Afterwards we determine the receiver phase using an optimization procedure. We perform the downconversion according to Eq. (3.14). We vary ϕ_{rec} as to minimize the cost function

$$R = \sum_i \left|A_{\mathrm{Q}}(t_i)\right|^2 - \sum_i \left|A_{\mathrm{I}}(t_i)\right|^2 . \tag{3.15}$$

This effectively shifts the signal to the in-phase component while minimizing the signal in the quadrature component. We define the phase determined with this procedure as the receiver phase.

We plot the determined receiver phase as a function of the LO frequency in Fig. 3.8. The general trend shows a linear decrease of the receiver phase with increasing ω_{LO}. This is due to the frequency-dependent

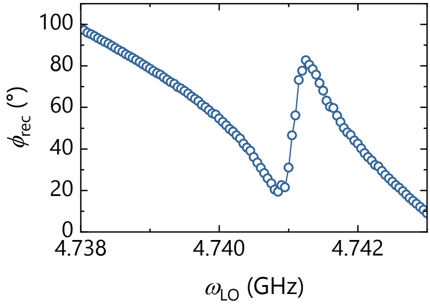

Fig. 3.8 Dependence of the optional receiver phase on the applied LO frequency. The general linear decrease of ϕ_{rec} with increasing LO frequency is caused by a phase shift due to finite cable lengths. The phase jump at $\omega_{\mathrm{LO}} \approx 4.741\,\mathrm{GHz}$ occurs because the probe tone at $\omega = \omega_{\mathrm{LO}} + \omega_{\mathrm{IF}}$ is in resonance with a microwave resonator.

phase accumulation caused by the finite cable lengths in the setup. For $\omega_{\mathrm{LO}} \approx 4.741\,\mathrm{GHz}$ the microwave probe tone at frequency $\omega = \omega_{\mathrm{LO}} + \omega_{\mathrm{IF}}$ is in resonance with a microwave resonator, resulting in a phase jump.

In order to facilitate the digital downconversion and in particular the optimization procedure, we have developed a Python program[3]. The software allows to load a measurement file and perform the receiver phase optimization. Of course, it can also be used to downconvert actual measurements using the previously determined receiver phase.

3.4.3 Microwave pulse generation and phase cycling

Once the optimal receiver phase is obtained, it is kept fixed for the actual pulsed ESR experiments. This is necessary to implement so-called *phase cycling*. Phase cycling is an established technique in NMR [145, 146] and ESR [13, 147] and can be used to suppress artifacts and undesired echos [23, 148].

---

[3] The software is available as free software at https://gitlab.com/stwe/echo-demodulator.git.

In the ESR and NMR community, the different pulse phases are denoted with a shorthand notation. The terms $+x, -x, +y, -y$ correspond to phases of 0°, 180°, 90° and 270°, respectively, and indicate the corresponding axis in the rotating frame around which the magnetization rotates during the nutation. Note that the phase of the pulse is always to be seen relative to the receiver phase. In terms of the detected microwave signal, $+x$ and $+y$ correspond to the in-phase and quadrature component of the downconverted signal.

We now exemplarily show a four-step phase cycle experiment of a standard spin echo pulse sequence. The measurements were conducted in the dilution refrigerator setup, using Sample #3. The sample temperature was $T = 75\,\mathrm{mK}$ and the magnetic field was tuned to the resonance field of the $\mathrm{Pb}_0/\mathrm{Pb}_1$ defects.

First, we test the correct phase relation of the generated microwave pulses. We generate a spin echo pulse sequence, where the first pulse has a fixed $+x$ phase. The phase of the second phase is varied in a $+x, -x, +y, -y$ cycle. We record the microwave pulses and perform the downconversion with the previously determined receiver phase. We show the in-phase and quadrature component of the downconverted signal in Fig. 3.9 (left panels). The amplitudes are shown in arbitrary units, normalized to one. As can be seen from the traces, the second pulse exhibits the correct phase in relation to the first pulse. For example, a relative phase shift of 90° moves to second shift to the Q quadrature, while a phase shift of 180° inverts the sign of the second pulse.

In a next step, we recorded the spin echo signal of the $\mathrm{Pb}_0/\mathrm{Pb}_1$. We perform single-shot measurements, where no signal averaging is performed. The spin echo signal is shown in the right panels for each phase combination. Note that the microwave pulses and echo signals are recorded with a different microwave pulse power and amplifier gain. Therefore, the noise visible in the graphs is not comparable. The echo for all phase cycling steps appears in the quadrature component

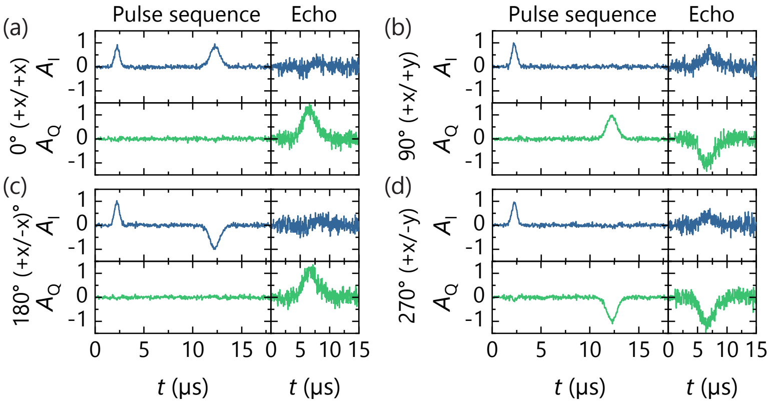

Fig. 3.9 Microwave pulses and corresponding echo for a spin echo sequence with a relative phase shift between the first and second pulse. We show the in-phase (I) and quadrature (Q) signal in arbitrary units for spin echo sequences with a relative phase shift of (a) 0°, (b) 90°, (c) 180° and (d) 270°. Note that the microwave pulses and corresponding echo are recorded at different microwave input power and amplification settings. The experiments were conducted with the magnetic field set to the resonance field of the Pb_0/Pb_1 defects.

of the downconverted signal, i.e. out-of-phase of the initial pulse. This can be visualized by considering the resonant spins after the first pulse. A $\pm x$ pulse rotates the spins in the yz plane of the rotating frame. As they do not acquire an additional phase during the free evolution time and the second pulse, they never leave that plane and are accordingly detected in the quadrature component of the signal [148].

For a relative phase shift of 0° and 180°, i.e. a $+x/\pm x$ phase cycle, we observe a spin echo signal with a positive sign. The associated rotations of this sequence are depicted schematically in Fig. 3.10 (a). During the first microwave pulse the magnetization rotates around the x axis, such that after the pulse it lies along the $-y$ axis. The second pulse then rotates the magnetization again around the x axis by 180° and the spin echo is detected along the $+y$ direction. As the rotation direction during the second pulse plays no role, we do not observe a sign change between the $+x/+x$ and $+x/-x$ phase cycle. For relative phase shifts

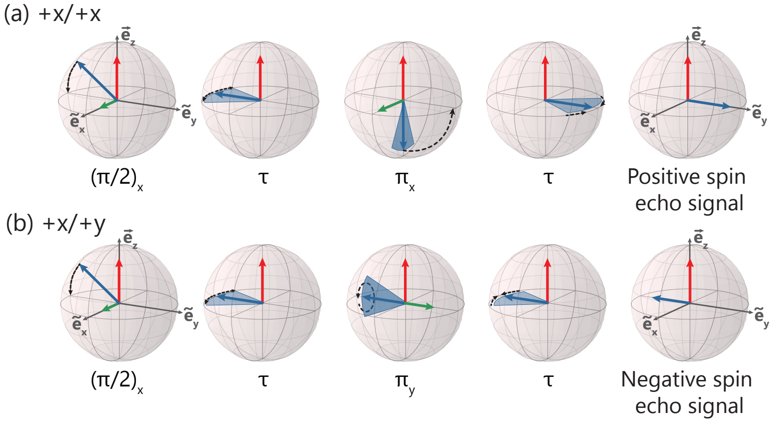

Fig. 3.10 Sign convention of the spin echo signal when applying (a) a $+x/+x$ pulse sequence and (b) a $+x/+y$ pulse sequence. In both cases, the magnetization is rotated to the $-y$ axis with the first pulse. The second pulse, however, rotates the magnetization either around the x or y axis. This leads to a spin echo signal with a opposite sign. The time points of the individual panels corresponds to Fig. 2.3.

of 90° and 270°, the second pulse rotates the magnetization around the y axis (cf. Fig. 3.10 (b)). Therefore, the magnetization remains along the $-y$ axis and we consequently observe a sign change for the $+x/\pm y$ phase cycle compared to the $+x/\pm x$ cycle.

In order to suppress artifacts (or unwanted echos for more complicated pulse sequences), the different echo signals are now added together. This step is generating the actual phase cycling signal. Here, it is important to consider the correct linear combination coefficients before adding the individual signals. For a two-pulse echo experiment as shown here, the $+x/\pm y$ echos have to be added with an inverse sign [148]. This four-step phase cycle is also known as EXORCYCLE in NMR [149, 150]. We show the results of a standard two-pulse spin echo experiment with no phase cycling ("one step") as well as phase cycling with two and four steps in Fig. 3.11.

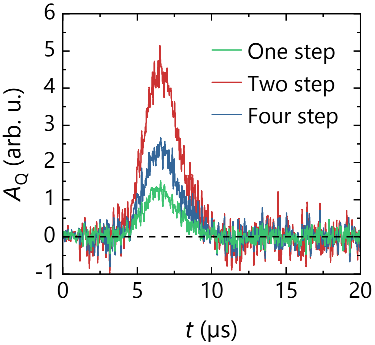

Fig. 3.11 Comparison of a standard spin echo experiment with no phase cycling (“one step”) as well as phase cycling with two and four steps. The signal amplitude as well as the signal-to-noise ratio increases with the number of steps. Additionally, the two- and four-step phase cycling remove potential DC offsets as well as unwanted signals.

The signal amplitude as well as the signal-to-noise ratio (SNR) increases with the number of steps. Additionally, the two-step $+x/\pm x$ phase cycle removes a potential receiver DC offset and unwanted signals (e.g. due to detected FID of the last pulse). In this simple two-pulse experiment, the four-step phase cycle does not remove any additional artifacts [148]. However, it leads to an increase of the SNR, as it effectively results in a signal averaging with four averages instead of two.

3.4.4 Pulse length calibration and echo integration

As a last step in the calibration measurements, the length of the microwave pulses have to be determined to induce rotations with a defined flipping angle. The flipping angle of a spin according to Eq. (2.14) is given by

$$\theta = \frac{g_e \mu_B}{\hbar} \int_0^{t_p} |B_1(t)| \,\mathrm{d}t. \tag{3.16}$$

In a spin echo sequence the two pulses should rotate the magnetization by 90° and 180°, respectively. However, due to the inhomogeneity of our microwave resonators (see Sec. 4.4.2 for details) we do not induce a perfect 90° and 180° rotation, as spins at different location in the sample experience a different B_1 field. Therefore, we define the optimal pulse duration as the pulse duration where the echo area is maximum, which corresponds to a mean B_1 field amplitude.

The echo area or echo intensity is obtained by numerically integrating the echo signal in a rectangular integration window with length Δt, centered on the echo maximum [8]. We choose the window width in such a way that the integration window contains the whole echo. For the spin coherence and life time measurements presented in Section 5.3 we choose a window length that corresponds to the width of the longest pulse. This promises the largest SNR when integrating the echo [8]. Most of the pulsed ESR experiments (such as spin coherence and life time measurements) rely on this echo detection, i.e. the intensity of the spin echo is recorded as a function of one or two variables (magnetic field, echo delay τ, relative phase shift, etc.).

For the pulse length calibration, we apply a series of standard spin echo pulse sequences, where we simultaneously vary the duration of the two microwave pulses, $t_{\pi/2}$ and t_{π}. We set $t_{\pi} = 2t_{\pi/2}$ and keep the echo delay τ fixed. In Fig. 3.12 (a), we exemplarily show the quadrature signal of the echo for a duration of the first pulse of 0.2 μs, 0.6 μs and 1.0 μs. For short pulse durations, the tipping angle is small and the magnetization remains more or less aligned along the z axis. As the spectrometer is only sensitive to the xy components of the magnetization, the corresponding echo signal is small. For increasing pulse length, the magnetization is rotated further and further away from the z axis. At the optimal pulse length, the induced mean rotation angle of the spins is closest to 90° and 180° and the echo signal is the largest. If the pulse lengths is then further increased, the magnetization rotates too far and the echo signal decreases accordingly.

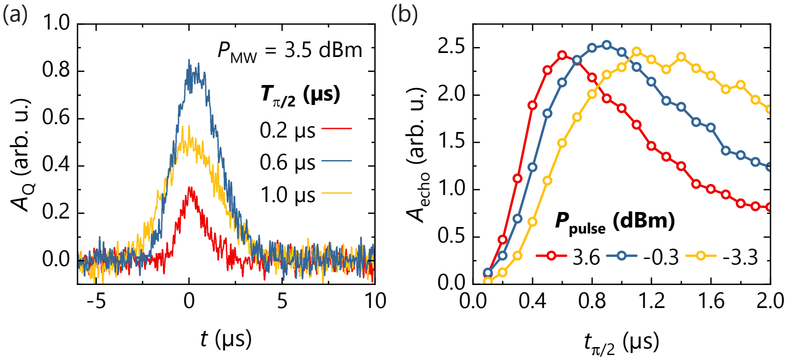

Fig. 3.12 Calibration procedure of the microwave pulse duration for a spin echo sequence. (a) We vary $t_{\pi/2}$ and set $t_\pi = 2t_{\pi/2}$. The echo amplitude as well as the echo area is the greatest for an intermediate pulse duration of 0.6 µs/1.2 µs. (b) Systematic evaluation of A_echo as a function of $t_{\pi/2}$ allows to determine the optimal pulse length for a given microwave power.

In order to extract the optimal pulse length, we integrate the echo signal. We plot A_echo as a function of the pulse duration in Fig. 3.12 (b) for several applied microwave powers. At the largest input power of 3.6 dBm, we obtain the an ideal pulse duration of $t_{\pi/2} = 0.6$ µs. The peak position then shifts to longer $t_{\pi/2}$ with decreasing microwave power, as the mean B_1 field also decreases. The pulse length calibration should be conducted for each resonator at the desired microwave pulse power.

3.4.5 Spectrometer nonlinearities

During normal operation of the spectrometer, the microwave components (in particular the amplifiers and IQ mixer) should be operated in the linear regime. Here, linear regime means that increasing the microwave power at the input of the device leads to a corresponding increase of the microwave power at the output of the device by the same amount. However, for high input powers, both device types show a nonlinear correlation between the input and the output power.

The threshold input power, when nonlinear behavior sets in, is characterized by the 1 dB compression point, $P_{1\mathrm{dB}}$. At this input power, the deviation between the real and expected (linear) output power is 1 dB. In order to circumvent nonlinearities we stay 6 dB below the respective 1 dB compression point.

In the following we determine the linear regime of the amplifier used for pulse amplification as well as for the amplifier chain and IQ mixer in the downconversion setup. To test the power amplifier at the cryostat input, we use the AWG to generate a constant sinusoidal signal at the intermediate frequency and feed it into the I and Q port of the vector source. We generate a LO signal such that the upconverted signal is at 5 GHz. We then amplify the upconverted signal and measure the microwave power at the output of the power amplifier as a function of the vector source power output using a power sensor (Rohde & Schwarz NRP-Z31). The corresponding data is displayed in Fig. 3.13.

The microwave power behaves linearly for a vector source power in the range of −55 to −15 dBm. We fit a linear function (black solid line) with a fixed slope of 1 to the linear region of the data in order to determine the 1 dB compression point. The onset of nonlinearity occurs due to the limited output power of the vector source, while the power amplifier still operates in the linear regime. The 1 dB compression point occurs at $P_{1\mathrm{dB}} = -12\,\mathrm{dB}$. We therefore use a maximum output power of the vector source of −18 dBm, which results in a microwave power after the power amplifier of approx. 25 dBm.

In a second test, we verify the linear regime of the downconversion setup. To test the microwave amplifier chain in the downconversion setup, we apply a constant microwave signal ($\omega = 5\,\mathrm{GHz}$) at the RF input port and measure the power at the RF output port. We vary the microwave power at the input and plot the measured output power in Fig. 3.14 (a). For an input power in the range of −65 to −45 dBm, the amplifier chain works in the linear regime. We again fit a linear function with a fixed slope to the data (solid black line). The 1 dB

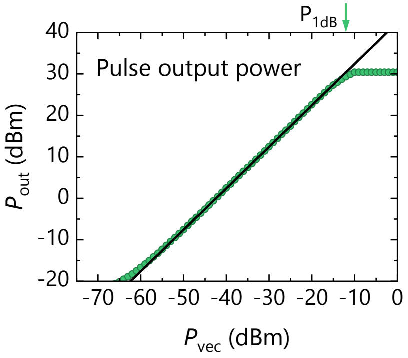

Fig. 3.13 Microwave power output after the amplifier used to amplify the generated microwave pulses as a function of the vector source power level. The 1 dB compression point (indicated by an arrow) is determined using a linear fit with a fixed slope of one (black solid line).

compression point is at $P_{1\mathrm{dB}} = -44\,\mathrm{dBm}$. Therefore, the power at the input of the downconversion box should not exceed −50 dBm[4].

To test the IQ mixer, we apply the same microwave signal as above to the RF input port. Additionally, we apply a LO signal with a frequency $\omega_{\mathrm{LO}} = 4.9375\,\mathrm{GHz}$, so that the downconverted signal is at a intermediate frequency of 62.5 MHz. We again vary the RF input power and measure the power output of the "I Out" port (the LO power is fixed). We conduct this measurement for three different video amplifier gain settings. The corresponding data is displayed in Fig. 3.14 (b). We again fit a linear function to the data (black solid line) to extract the 1 dB compression point.

As expected, the video gain amplifier amplifies the outgoing signal and the curves are shifted corresponding to the respective gain setting. For a video gain of 10 dB and 20 dB, both curves are qualitatively similar. Linear behavior occurs for an input power in the range of −80 to −50 dBm with a 1 dB compression point of $P_{1\mathrm{dB}} = -49\,\mathrm{dBm}$. As the

---

[4] We place a 10 dB attenuator at the input of the downconversion setup for this purpose. See Sec. 3.2 for details.

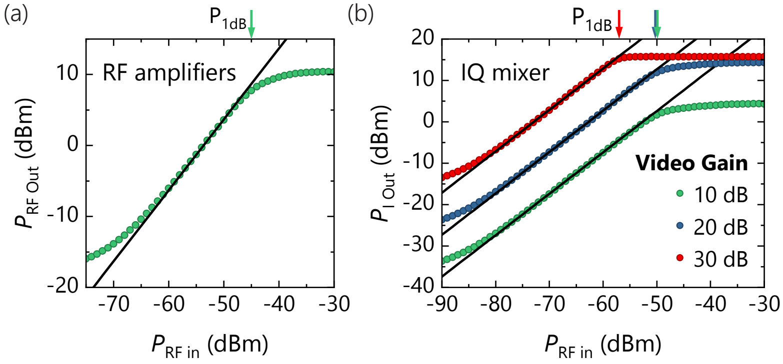

Fig. 3.14 (a) Power output at the "RF Out" port of the downconversion setup as a function of the RF input power. The black line is a linear fit with a forced slope of 1 to extract the 1 dB compression point. (b) Power output at the "I Out" port of the downconversion setup as a function of the RF input power. The measurement is performed for three different video amplification gain settings. For a video gain of 30 dB the video amplifier is driven into saturation, which leads to a reduced 1 dB compression point.

begin of the nonlinear regime is the same regardless of the video gain, the nonlinearity is caused by the IQ mixer. For a video gain of 30 dB, the linear regime extends only to approx. −60 dBm and then drops off ($P_{1\mathrm{dB}} = -57$ dBm). At this power, the video amplifier saturates and enters the nonlinear regime. In order to avoid nonlinear behavior of the IQ mixer, the input power at the downconversion setup input should be less than −55 dBm for a video gain of 10 – 20 dB. For a video gain of 30 dB, the maximum input power should be less than −63 dBm.

CHAPTER 4

SUPERCONDUCTING MICROWAVE RESONATORS

Microwave resonators are a key component of any ESR experiment. They create the microwave magnetic field B_1 at the sample location, enhance its field amplitude and increase the sensitivity for inductive detection of magnetization [12, 13]. Conventional ESR resonators are often based on three-dimensional (3D) microwave cavities, which is essentially a hollow metallic box. Inside the metallic box, a standing wave is forming, giving rise to the resonantly enhanced microwave magnetic field. Cavities provide a homogeneous microwave magnetic field over a large sample volume. However, their dimensions are determined by the wavelength of the desired resonance frequency, which is in the order of centimeters in the microwave regime. For samples of small volumes or thin geometries, this leads to small filling factors and, therefore, a low sensitivity.

For these kind of samples, it is therefore advantageous to use planar microresonators, which substantially reduce the mode volume by confining the electromagnetic wave in at least one dimension to a volume much smaller than the wavelength. Depending on the sample size and geometry, they offer an increased filling factor and therefore an enhanced sensitivity compared to 3D cavities [151, 152]. Additionally, when performing experiments at low temperatures, superconducting materials can be used. This reduces microwave losses and offers extraordinarily high quality factors up to 10^7 [153]. However, due to shielding of magnetic fields from their inside, simple three-dimensional cavity resonators cannot be used for ESR applications. Here, planar resonators allow the combination of large magnetic fields and superconducting materials. A plethora of different microwave geometries [154–156] have been developed and are applied in different fields of research.

In the area of ultra-sensitive ESR, superconducting planar microwave resonators are tailored to increase the coupling strength between the spin ensemble and the microwave resonator in order to enhance the read-out sensitivity of the measurements [48, 49]. However, so far a quantitative analysis of planar resonator designs regarding the achievable collective coupling rate is still missing. Furthermore, it is desirable to improve the homogeneity of the generated microwave magnetic field to enable coherent control of spin systems. In this chapter, we employ finite-element (FEM) simulations of different microwave resonator geometries to calculate the spatial distribution of the microwave magnetic field. We use the simulated data to characterize the spatial field distribution and find that one resonator designs offers an increased homogeneity compared to the other designs. Finally, we show that the simulated 3D field distribution allows to quantitatively calculate the expected collective coupling rate g_{eff}.

In the following, we first introduce the concept of lumped element microwave resonators and present fundamental design considerations. In Section 4.2 we derive an expression for the collective spin-photon coupling strength in the presence of an inhomogeneous B_1 field. We introduce the three different planar resonator structures used in this thesis in Section 4.3. In Section 4.4 we present our simulation setup and analyze the 3D field distribution of the resonators. We analyze the single-spin coupling rate and compare the FEM simulations to experimental data. In Section 4.5 we investigate the sensitivity of the microwave resonators to temperature and magnetic field changes and show how the robustness can be improved. In the final Section 4.6, we present continuous-wave ESR measurements on a phosphorus-doped silicon sample and present a quantitative modeling of the collective coupling rate based on our FEM simulations.

Parts of this chapter are based on the master project of Petio Natzkin [124], whom I supervised during his thesis. The main results of this chapter were published in Physical Review Applied [SW1].

4.1 Introduction

Microwave resonators can be understood as a LC circuit, consisting of an inductance L connected in parallel to a capacitance C[1]. A coplanar waveguide resonator (CPWR) is constructed by introducing two cuts in the signal line of a CPW (cf. Fig. 4.1) (a), effectively modifying the boundary for the microwave. Analogously to a 3D cavity, this allows the formation of standing wave patterns along the signal line, where the length of the wire determines the frequency of the fundamental mode [38]. For a CPWR, the inductance and capacitance is distributed along the whole wire.

In contrast to that, a lumped element resonator (LER) consists of a discrete inductance L and capacitance C [39, 157, 158], as presented in Fig. 4.1 (b). For a LER, the electric and magnetic fields are spatially separated in the capacitor and inductor [157]. By embedding the LER in the ground plane of a CPW, in the vicinity of the signal line, microwave signal can be coupled into the LER. This coupling can be either capacitive or inductive, depending on the relative location of the resonator to the anti-nodes of the electric and magnetic field of the

---

[1] We neglect a possible resistive component here.

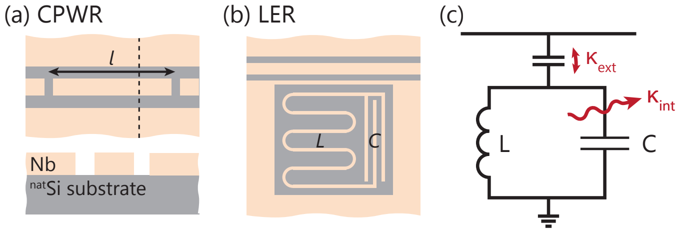

Fig. 4.1 Schematic drawing of planar microwave resonators. The metallized areas are shown in beige, the silicon substrate is shown gray. (a) The CPWR is fabricated by introducing two cuts at a distance l in the signal line of a coplanar waveguide, thereby modifying the boundary conditions of the electromagnetic wave. (b) The LER is a parallel LC circuit consisting of an inductance L and capacitance C. (c) Electrical schematic of a LER. The LC circuit is coupled capacitively to a microwave feedline. The loss rates κ_{ext} and κ_{int} describe the external and internals losses (for details, see text).

feedline. A schematic of a capacitively coupled LC circuit is shown in Fig. 4.1 (c).

The resonance frequency of a LER (or any parallel LC circuit) is given by [12]

$$\omega_\mathrm{r} = \frac{1}{\sqrt{LC}}. \tag{4.1}$$

Since the geometry of the inductance and capacitance are independent of the microwave wavelength, it is possible to design more compact resonators compared to CPWR. While a CPWR supports a fundamental and higher harmonic modes, a LER is limited to a single microwave mode. However, due to the small outline, several LER with a different resonance frequency can be placed along a single CPW to enable a multi-frequency read-out.

The losses of a microwave resonator are characterized by the quality factor Q. It is the ratio of the energy stored in the electromagnetic mode and the energy lost in each cycle [12]. It is related to the resonance frequency via

$$Q = \frac{\omega_\mathrm{r}}{2\kappa_\mathrm{c}}, \tag{4.2}$$

where κ_c is the loss rate of the resonator. The loss rate can be extracted as the half-width-half-maximum from the resonator spectrum (measured in angular frequency) as described in Sec. 3.4.1. The quality factor is comprised of internal and external contributions, which add up reciprocally:

$$\frac{1}{Q} = \frac{1}{Q_{\mathrm{int}}} + \frac{1}{Q_{\mathrm{ext}}}. \tag{4.3}$$

Internal quality factors include dielectric, resistive and radiative losses [38]. Additionally, superconducting microwave resonators suffer losses through quasiparticle excitation and coupling to two-level systems (TLS) [159–161]. The external quality factor describes the coupling strength of the LER to the "environment", which is in our case the microwave feedline. Both the internal and external quality factor can be related to external and internal loss rates,

$$Q_{\mathrm{int}} = \frac{\omega_r}{2\kappa_{\mathrm{int}}}, Q_{\mathrm{ext}} = \frac{\omega_r}{2\kappa_{\mathrm{ext}}}, \tag{4.4}$$

such that the total loss rate consists of the two individual loss rates,

$$\kappa_c = \kappa_{\mathrm{int}} + \kappa_{\mathrm{ext}}. \tag{4.5}$$

The microwave resonators presented here are typically operated in the overcoupled regime, i.e. $Q_{\mathrm{ext}} \gg Q_{\mathrm{int}}$ [38]. Therefore, the total quality factor Q is dominated by the external quality factor and can be accordingly tuned by geometry.

In an ESR application, the microwave resonator is used to excite and detect ESR transitions in an electron spin ensemble. In a continuous-wave ESR experiment, the detected signal at resonance depends on the amount of microwave power absorbed by the sample [12]. The resonance absorption will lead to a decrease of the quality factor of the microwave resonator, which can be expressed as an additional loss term $1/Q_{\mathrm{spin}}$ in Eq. (4.3). Q_{spin} is the ratio of microwave power stored in the overall resonator mode volume V_m and the power dissipated in the sample [12]:

$$Q_{\mathrm{spin}} = \frac{\frac{1}{2}\mu_0 \int_{\mathrm{cavity}} B_1^2 \,\mathrm{d}V}{\frac{1}{2}\mu_0 \int_{\mathrm{sample}} \chi'' B_1^2 \,\mathrm{d}V}, \tag{4.6}$$

where χ'' is the RF susceptibility of the sample. χ'' describes the response of the spin system to an externally applied oscillating B_1 field. Eq. (4.6) can be written as $Q_{\mathrm{spin}} = (\chi'' \nu)^{-1}$ in terms of a filling factor

$$\nu = \frac{\int_{\mathrm{sample}} B_1^2(\vec{r}) \,\mathrm{d}V}{\int_{\mathrm{cavity}} B_1^2(\vec{r}) \,\mathrm{d}V}. \tag{4.7}$$

4.2 Spin-photon coupling in inhomogeneous B_1 fields

In the following we discuss the spin-photon coupling in the context of an inhomogeneous B_1 field distribution. From Eq. (2.60), which defines g_{eff} via the individual coupling rates of the spins to the resonator field, we derive an expression for the collective coupling strength of an ensemble with N spins:

$$g_{\mathrm{eff,hom}} = \frac{g_{\mathrm{e}} \mu_{\mathrm{B}}}{2\hbar} \sqrt{\frac{1}{2} \mu_0 \rho_{\mathrm{eff}} \hbar \omega_{\mathrm{r}} \nu}. \tag{4.8}$$

Here, $\rho_{\mathrm{eff}} = \rho V P(T)$ is the effective spin density, with the sample volume V and the thermal spin polarization $P(T)$. For a homogeneous B_1 field, the filling factor reduces to $\nu = V/V_m$ and describes the ratio between the sample volume V and the mode volume V_{m}.

Eq. 4.8 assumes a homogeneous distribution of the microwave magnetic field B_1 over the sample volume. However, the planar resonators used in this thesis typically have a spatially dependent microwave field distribution which leads to a spatially dependent coupling distribution. Furthermore, the equation does not take into account the orientation of the static magnetic field $\vec{B}_0$ relative to the $\vec{B}_1$ field required for exciting

ESR transitions. From the Bloch equations (2.9)–(2.11) it is clear that the direction of the oscillating magnetic field has to be perpendicular to the direction of the static magnetic field, i.e. $\vec{B}_0 \perp \vec{B}_1$ [12].

Eq. (4.8) can be generalized by taking the driving field amplitude B_1 into account when computing the filling factor according to Eq. 4.7. For planar microwave resonators, the filling factor is limited to $\nu \leq 0.5$, as typically only the half-space above the resonator surface can be filled with the spin ensemble. The filling factor is additionally reduced if components of the generated magnetic field are aligned parallel to $\vec{B}_0$.

Our FEM simulations allow us to calculate the filling factor for a given sample and resonator geometry. We simulate the microwave magnetic field distribution for the desired resonator geometry (see Sec. 4.4.2 for details). We export the computed microwave magnetic field in discrete volume elements with volume ΔV. In order to calculate the integrals in Eq. (4.7), we change the integrals to sums over all volume elements and obtain for the inhomogeneous filling factor

$$\nu \longrightarrow R_{yz} = \frac{\sum_V \left| B^{yz}_{1,\mathrm{sim}}\left(\vec{r}\right) \right|^2}{\sum_{V_\mathrm{m}} \left| B^{xyz}_{1,\mathrm{sim}}\left(\vec{r}\right) \right|^2}, \tag{4.9}$$

In the nominator, we sum over all volume elements in the sample volume V and take into account only magnetic field components in the yz plane[2], $\left|B_1^{yz}\right| = \sqrt{\left(B_1^y\right)^2 + \left(B_1^z\right)^2}$. The denominator is a normalization factor and adds up the total magnetic field amplitude B_1^{xyz} over the whole sample volume.

Combining Eq. (4.8) and (4.9), we obtain for the collective coupling strength in the presence of an inhomogeneous microwave magnetic

---

[2] The static magnetic field in our experiment is parallel to the x axis, $B_0 \parallel \hat{x}$.

field[3]

$$g_{\mathrm{eff,inhom}} = \frac{g_{\mathrm{e}}\mu_{\mathrm{B}}}{2\hbar}\sqrt{\frac{1}{2}\mu_0\hbar\omega_{\mathrm{r}}\rho_{\mathrm{eff}}\frac{\sum_V |B^{yz}_{1,\mathrm{sim}}\left(\vec{r}\right)|^2}{\sum_{V_{\mathrm{m}}} |B^{xyz}_{1,\mathrm{sim}}\left(\vec{r}\right)|^2}}. \tag{4.10}$$

Using Eq. (4.10), we can calculate and theoretically predict the collective coupling strength of spin ensemble and an arbitrary microwave resonator, as long as the microwave magnetic field distribution is known from simulations. In Sec. 4.6 we calculate g_{eff} for the three resonator geometries presented in the following and compare our calculations to experimentally determined values.

4.3 Microwave resonator geometries

In this section, we present the resonator geometries studied in the following. The generic device layout is presented in Fig. 4.2 (a) with the most important geometry parameters being listed in Table 4.1.

The central feature of the sample is a microwave feedline in coplanar waveguide (CPW) geometry [162]. The signal line width $s = 20\,\mu\mathrm{m}$ and signal-to-groundplane separation $w = 12\,\mu\mathrm{m}$ are chosen such that the impedance of the CPW is approximately matched to $50\,\Omega$ [163]. At the edges of the sample, enlarged connection pads enable the electrical connection to the external microwave circuitry via SMA end launch connectors (see Sec. 3.1 for more details on the sample mounting). A high-frequency electromagnetic wave passing through the CPW generates an electromagnetic field, which couples capacitively or inductively to resonators placed in the vicinity of the feedline (indicated by the dashed rectangle in Fig. 4.2 (a)).

The three different resonator geometries are presented in Fig. 4.2 (b)–(d), namely (b) a capacitively-shunted meander resonator (CR), (c) a meander resonator (MR), and (d) a spiral resonator (SR). The local coordinate

---

[3] See Appendix A2.2 for an alternative derivation taking into account the average spin density in a volume element ΔV.

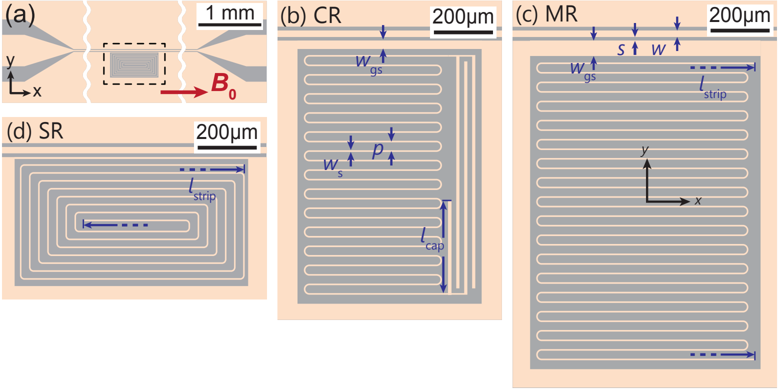

Fig. 4.2 Schematic drawing of the planar resonator geometries studied in the following. (a) Generic sample layout with a central coplanar waveguide (CPW). The microwave resonators are excited by placing them in a pocket in the ground plane, near the feedline (dashed rectangle). (b) The capacitively-shunted meander resonator (CR) consists of a meandering inductor shunted by a interdigitated capacitor. (c) The meander resonator (MR) omits the interdigital capacitor and compensates the reduced capacitance by increasing the meander wire, acting effectively as a half-wavelength resonator. (d) The spiral resonator (SR) is a derivate of the MR, where the meander wire is arranged in a two-dimensional coil-like structure .

Table 4.1 Geometry parameters of the resonators. For a definition of the parameters, see text and Fig. 4.2. s and w are chosen such that the impedance of the CPW is approximately 50 Ω. The meander wire width w_s and distance p between wires were kept constant for all resonators. Varying l_strip and l_cap allows to tune the resonance frequency of the MR/SR and CR, respectively. The coupling to the feedline is varied by changing the width w_gs of the metal strip between the resonator and the signal line.

Parameter	Value	Parameter	Range
s	20 µm	l_strip	10 – 24 mm
w	12 µm	l_cap	0 – 0.7 mm
w_s	5 µm	w_gs	10 – 80 µm
p	20 µm		

system is chosen such that the x axis points along the CPW, the y axis is perpendicular to the CPW and the z axis is the out-of-plane direction. The origin of the coordinate system is in the center of the resonator.

The CR is a lumped element microwave resonator, where the inductance L and capacitance C are provided by a meander-shaped inductor and an interdigital capacitor. The resonance frequency is given by Eq. 4.1 and can be tuned by varying either the inductance or capacitance. In our case, we change the length of one of the capacitor fingers, l_cap, to change the resonance frequency (see Sec. 4.4.5 for more details). However, an analysis of this tuning behavior revealed that a significant contribution (up to 50 %) to the capacitance is provided by the meandering structure. This led to the development of the MR, where the interdigital capacitor is omitted. Instead, the reduced capacitance is compensated by increasing the total length of the meander structure. The meander resonator effectively works as a $\lambda/2$-resonator, where a standing wave is excited [164]. Indeed, the resonance frequency of the MR can be approximated by assuming a wavelength twice the length of the meander-shaped strip and a reduced dielectric constant $\epsilon_\mathrm{r} = (\epsilon_\mathrm{Si} + \epsilon_\mathrm{air})/2 \approx 6.35$.

Due to the meander-shaped wire of the CR and MR, the AC current flows anti-parallel in neighboring meander strips. This leads to a destructive interference of the electromagnetic field and consequently to a fast decay of the microwave magnetic field B_1 along the z direction, i.e. out of plane of the microwave resonator. The characteristic decay length along the z direction of the microwave magnetic field depends on the distance p between adjacent wires. In our work we keep this distance constant at $p = 20\,\mu\mathrm{m}$.

The anti-parallel current flow also causes a significant inhomogeneity of the B_1 field near the resonator surface. For most pulsed ESR experiments, which use rectangular pulse excitation schemes, a large B_1 inhomogeneity is undesired, as it leads to a non-coherent evolution of the magnetization. Several techniques have been proposed to compensate the B_1 inhomogeneity, e.g. adiabatic pulse shapes [134–136] or optimal control pulses [137, 138]. However, these pulse schemes are only able to compensate the B_1 inhomogeneity to a certain point and, additionally, require the use of high-bandwidth resonators.

In order to improve the inherent B_1 inhomogeneity of the MR, the SR is based on a two-dimensional coil-like arrangement of the wire. Here, the current in two adjacent wires flows parallel and the generated electromagnetic field overlays constructively. This leads to an improved B_1 homogeneity as well as a slower decay of the microwave magnetic field along the z direction (see Section 4.4.2 for details). Here, the characteristic decay length is in the order of the lateral dimensions of the resonator, which is one order of magnitude larger than the distance p between adjacent wires.

As mentioned earlier, the resonance frequency of the microwave resonators can be tuned by changing various geometry parameters. The frequency range under consideration is given by physical as well as experimental limitations. A lower boundary of the resonance frequency is given by the requirement of cooling the resonator to its quantum mechanical ground state, i.e. $\hbar\omega_\mathrm{r} \gg k_\mathrm{B}T$. For $T = 50\,\mathrm{mK}$, $k_\mathrm{B}T/\hbar \approx 2\pi \cdot 1\,\mathrm{GHz}$. The upper frequency boundary is given by the superconducting energy gap Δ. Irradiation with microwaves above this energy leads to quasiparticle excitation and thereby to significant losses [165]. Additionally, the surface impedance scales with ω^2 [166], so in order to minimize losses, a low resonance frequency is desirable. For our measurements, the available frequency range is additionally limited by the bandwidth of the cryogenic amplifiers and low noise amplifiers to 4–8 GHz.

We tune the design resonance frequency of the CR by varying the length l_{cap} of one of the capacitor fingers. The resonance frequency of the MR and SR is changed by varying the total strip length l_{strip} of the meander wire. This allows to tune the resonance frequency for all resonators in the desired frequency range. The external quality factor is controlled by the width w_{gs} of the metal separation strip between the signal line and the resonator. As the resonator is operated in the overcoupled regime, this changes the total quality factor. Table 4.2 summarizes the geometric parameters as well as the simulated resonance frequency and quality factors of the resonators presented in this work. The detailed tuning behavior as well as a comparison to FEM simulations is presented in Sec. 4.4.5.

4.4 Finite element simulations

In order to get a better understanding of the different resonator geometries, we first implement finite element simulations using the commercial simulation package CST Microwave Studio 2016 [167]. We first describe how the simulations are implemented (Sec. 4.4.1). In the next section, we compare the simulations to experimental results followed by a discussion of the field homogeneity of the different resonator geometries (Sec. 4.4.2).

4.4.1 Simulation setup

In our modeling approach, we take the entire chip into account. The model is parameterized to allow us to efficiently explore the influence of the individual parameters on the resonator performance. We start with the definition of a silicon substrate with dimensions of 6×10×0.525 mm^3. On top of the substrate, we model the superconductor by a 150 nm thick layer of perfect electrical conductor (PEC). In this simplified approach, we do not take surface impedance or kinetic inductance into account [166, 168]. We also neglect the 10 nm thick Al capping layer (see Sec. 3.1) in the simulations. We implement the CPW and resonator by implementing a suitable layout file in the program.

In the ESR experiments presented in Sec. 4.6, a spin ensemble hosted in a silicon crystal is placed on top of the resonator, where it interacts with the microwave magnetic field of the resonator. As this alters the effective dielectric environment of the resonator, we also include a silicon body with the sample dimensions of $3.4 \times 3.4 \times 0.42\,\mathrm{mm}^3$ in the simulations. The microwave signal is applied to the structure via one of two waveguide ports, defined at both ends of the feedline. The dimensions of the waveguide ports have to be chosen carefully to achieve an optimal excitation of the microwave feedline[4]. The power applied to the waveguide ports is 0.5 W. Note that the simulation only considers the linear response regime. Non-linear excitations, as they occur in experiments for elevated microwave powers, are not accounted for.

The simulations are performed by a frequency-domain solver. First, the 3D model is divided into tetrahedral mesh cells with a minimum edge length of 0.15 μm. In a second step, the Maxwell equations are solved using a finite-element method (FEM) on the tetrahedral mesh. During the simulation, the mesh is adapted further to increase its quality, until the S-parameter deviation between subsequent simulation runs falls below a convergence threshold.

---

[4] A good overview and a rule of thumb for choosing the correct waveguide port dimension is given in the CST Microwave Studio help file. For simpler structures, the waveguide port dimension can also be calculated using an included macro (choose "Macro→Solver→Port→Calculate port extension coefficient").

Table 4.2 Parameters for the three resonator geometries, extracted from finite element simulations. The mode volume is estimated as the volume where the magnetic field amplitude decays to 0.5 % of its maximum value. l_{decay} is the characteristic decay length of the $|B_1^{yz}$ magnitude along the z axis.

Res.	Dimensions (μm^2)	V_{m} (μm^3)	w_{gs} (μm)	$\omega_{\mathrm{r}}/2\pi$ (GHz)	Q_{ext}	l_{decay} (μm)
SR	770 × 410	1.88×10^7	60	4.874	40643	103.3 ± 0.3
MR	760 × 1000	1.52×10^7	60	5.689	12981	13.7 ± 0.5
CR	580 × 800	1.41×10^7	4	5.317	4920	12.5 ± 0.3

We obtain two different types of results from the simulation: (i) the scattering parameters S_{ij} as well as (ii) the microwave magnetic field distribution. The microwave magnetic field distribution is discretized and exported as the average magnetic field in a volume element with dimensions $1\times1\times1$ μm^3 (SR: $1.5\times1.5\times1.5$ μm^3). Table 4.2 summarizes the extracted parameters as well as the tuning parameter for the three resonator geometries. The mode volume is estimated as the volume where the magnetic field amplitude decays to 0.5 % of its maximum value. The resonance frequency as well as the quality factors are extracted using the fitting routine described below.

The maximum microwave field amplitude not only depends not only on the applied microwave power but also on the quality factor (or linewidth) of the resonator. We match the simulated field amplitude B_1^{sim} to the experimental conditions by rescaling B_1^{sim} to the same average number of photons in the resonator as in the simulations. To this end, we calculate the photon numbers n_{sim} and n_{exp} using Eq. 2.39 for both the simulation and experiment and rescale the microwave magnetic field amplitude according to

$$B_1 = B_1^{\mathrm{sim}} \cdot \sqrt{n_{\mathrm{exp}}/n_{\mathrm{sim}}}. \tag{4.11}$$

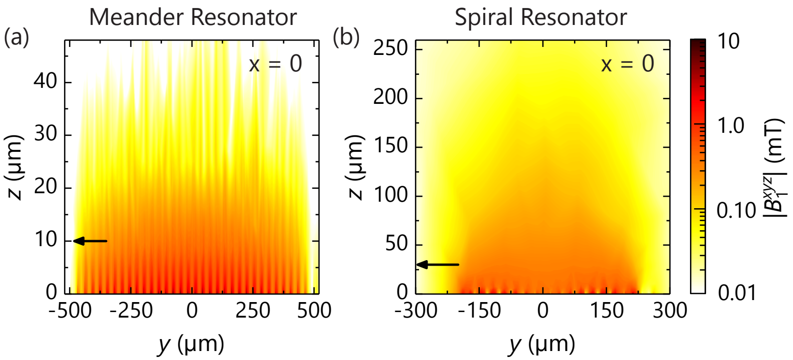

Fig. 4.3 Simulated magnetic field distribution $|B_1^{\mathrm{yz}}|$ for the (a) MR and (b) SR in the yz-plane. Anti-parallel current flow in adjacent wires results in a highly inhomogeneous field for the MR, while parallel current flow leads to a more homogeneous field for the SR. Arrows indicate the z position of the horizontal cuts displayed in Fig. 4.4.

4.4.2 B_1 magnetic field homogeneity

We first investigate the microwave magnetic field amplitude as well as the homogeneity of the meander and spiral resonator. For a quantitative comparison regardless of the different quality factors of the two resonators, we rescale the magnetic field amplitude to to an average photon number of 10^{12} This corresponds to an applied power of $-19\,\mathrm{dBm}$ for the SR and $-14.5\,\mathrm{dBm}$ for the MR.

Due to our choice of the static field direction along the x axis, the y and z components of $\vec{B}_1$ are able to drive ESR transitions, while the dynamic magnetic field along the x direction cannot be used for ESR experiments. We therefore plot the magnetic field magnitude $|B_1^{\mathrm{yz}}|$ in the yz-plane ($x = 0$) for the MR and SR in Fig. 4.3 (a) and (b), respectively.

The presented data shows a qualitative difference between the two resonator geometries. In the MR, the microwave current in adjacent wires flows anti-parallel. This results in an opposing microwave magnetic field that interferes destructively in the far field and thus leads to a fast decay as well as a pronounced inhomogeneity of the microwave magnetic field. In contrast, the microwave current in the SR flows in a parallel fashion in the two halves of the resonator, resulting in an improved B_1 homogeneity. Furthermore, the microwave magnetic field does not cancel in the far field and thus decays slower than for the MR (note the different scale on the vertical axes). We extract the decay length along the z axis in the center of the resonator and give the values in Table 4.2. The decay length of the SR is larger than for the MR and CR by a factor of approximately 8.

For a more quantitative comparison, we plot the components of the microwave magnetic field B_1^y and B_1^z as well as the magnitude $|B_1^{yz}|$ along the x and y direction in Fig. 4.4. The complementary coordinates are specified in the respective panels. The microwave magnetic field along the y axis (panel a) generated by the MR exhibits a periodic modulation of B_1^y and B_1^z and accordingly $|B_1^{yz}|$, which is related to the distance p between adjacent wires. Directly above the meander wire, the in-pane B_1^y component is maximum and the out-of-plane B_1^z component is zero. Between two adjacent meander wires, B_1^z is maximal and B_1^y is zero. This behavior is also reflected in Fig. 4.4 (c) for a cut along the x direction. The data presented in this figure is taken at a position in between two adjacent wires. Again, the out-of-plane component is maximal, while the in-plane component is zero.

The magnetic field components of the SR are shown in Fig. 4.4 (b) and (d). Along the y axis (panel a), the in-plane component B_1^y exhibits a sign-change at $y = 0$ due to the anti-parallel current flow in the two resonator halves, while the out-of-plane component exhibits a maximum at $y = 0$. However, the overall magnitude $|B_1^{yz}|$ is homogeneous over a region of $\approx 400\,\mu\mathrm{m}$. Along the x direction (panel d), the in-plane component is roughly zero, as the field cut is taken between two meandering wires.

When discussing the homogeneity of the MR and SR, two further import aspects should be taken into account. First, both designs

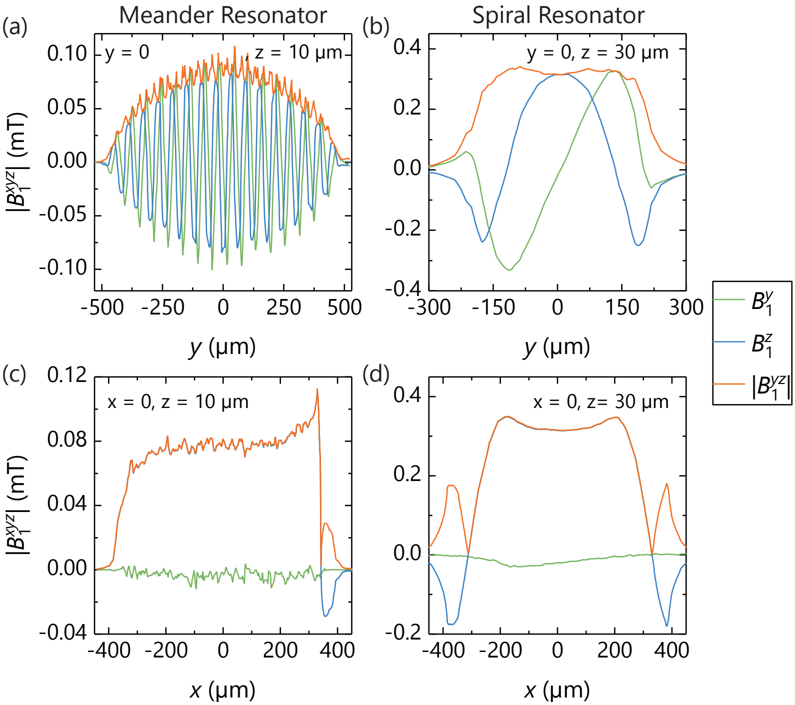

Fig. 4.4 Magnetic field components B_1^y, B_1^z as well as the magnitude $|B_1^{yz}|$ at fixed distance for the (a,c) MR and (b,d) SR along the y and x axis. The oscillatory behavior of the microwave magnetic field of the MR is clearly observable, while the SR generates a more homogeneous magnetic field.

show an inhomogeneous B_1 distribution directly above the resonator due to the discrete structure of the resonator wire. For the MR, this inhomogeneity persists throughout the mode volume, while for the SR, the inhomogeneity cancels in a distance z above the resonator that corresponds roughly to the wire distance p. Secondly, the homogeneity along the z direction is much more favorable for the SR due to the longer decay length. By inserting a thin Polyimid (Kapton) spacer between the resonator and the sample, the B_1 inhomogeneities in the near-field of the SR can be avoided.

In the following we discuss two different sample geometries: (i) a bulk sample with dimensions much larger than the lateral dimensions of the resonators and a thickness large compared to the decay length of the resonators and (ii) a thin sample with lateral dimensions of $300 \times 300\,\mu\text{m}^2$ and thickness 1 µm, placed in the center of the resonator. In particular, we find for the small sample at a distance of 30 µm above the SR, an extended region of 20 µm thickness, where the homogeneity is better than 10 %.

4.4.3 Conversion factor

The data presented in Fig. 4.4 suggests a difference in the conversion factor of the two resonances. The conversion factor relates the incident microwave power P_S to the mean $|B_1^{yz}|$ magnitude generated by the resonator. It is defined as [12]

$$C_\text{conv.} = \frac{\left|B_{1,\text{mean}}^{yz}(z)\right|}{\sqrt{QP_\text{S}}}, \tag{4.12}$$

where Q is the quality factor of the resonator. In order to calculate the conversion factor, we use the mean magnetic field in a slice with 1 µm thickness (1.5 µm for the SR). We plot the conversion factor C calculated for a small, thin sample ($300 \times 300 \times 1\,\mu\text{m}^3$, dashed lines) as well as for a bulk sample ($3.4 \times 3.4 \times 0.42\,\text{mm}^3$, solid lines) in Fig. 4.5.

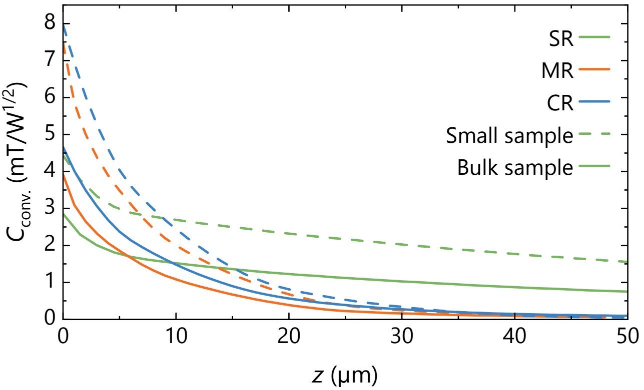

Fig. 4.5 Conversion factor C of the different resonators as a function of distance above the resonator for two different sample geometries (see text). MR and CR show larger maximum values but decrease faster with increasing distance compared to the SR.

Close to the resonator surface, the MR and CR show the highest conversion factors with maximum values up to $8\,\mathrm{mT}/\sqrt{\mathrm{W}}$. This value is about one order of magnitude larger than the conversion factors is achieved in commercial microwave resonators [169].

For an increasing distance to the resonator, the conversion factor significantly decreases. At a distance $z \approx 10\,\mu\mathrm{m}$ the longer decay length of the B_1 field of the SR comes into effect and subsequently the SR provides a larger microwave magnetic field. In general, the conversion factors for the bulk sample are lower than for the small sample. For the bulk sample, the microwave magnetic field at the edges of the mode volume is small, therefore the average magnetic field which is considered in the calculation, is reduced.

4.4.4 Single spin-photon coupling distribution

The 3D microwave magnetic field distribution can also be used to calculate the single spin-photon coupling constant distribution. To this

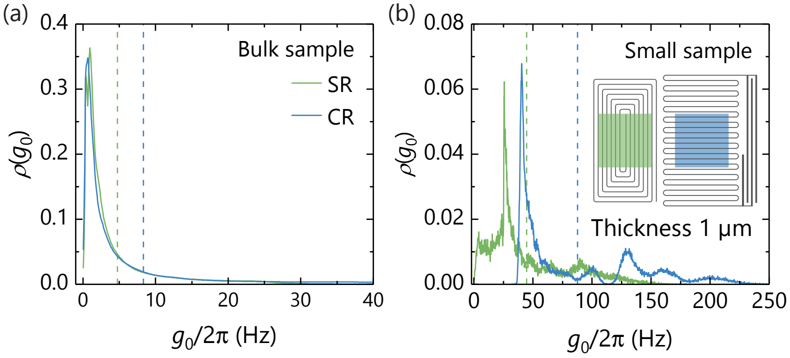

Fig. 4.6 Distribution of the single spin-photon coupling constant $g_0/2\pi$ for the (a) bulk and (b) small sample. Dashed lines indicate the average single spin-photon coupling constant for each resonator. The schematic drawing in (b) indicates the position of the investigated sample region relative to the resonator.

end, we normalize the microwave magnetic field to an average photon number of 0.5, so that the B_1 amplitude corresponds to the vacuum fluctuations in the resonator. We calculate the single spin-photon coupling constant g_0 using Eq. (2.49):

$$g_0/2\pi = \frac{g_e \mu_B}{2\hbar} \left| B_{1,0}\left(x, y, z\right) \right|, \tag{4.13}$$

where $\left|B_{1,0}\left(x, y, z\right)\right|$ is the mean vacuum magnetic field amplitude of the volume element at position x, y, z. We plot the histogram of g_0 in Fig. 4.6 for the (a) bulk sample and (b) small sample. The dashed line indicates the average single spin-photon coupling constant for each resonator type.

The coupling distribution $\rho\left(g_0\right)$ for the bulk sample in panel (a) is qualitatively the same for both the SR and CR with a sharp peak at $g_0/2\pi \approx 1\,\mathrm{Hz}$ and average coupling rates of 4.74 Hz and 8.33 Hz, respectively. Spins located at the edge of the mode volume are coupled weakly to the resonator, while spins closer to the resonator surface are coupled more strongly. However, the number of spins close to the resonator is much smaller then the number of spins at the edge of the mode volume, resulting in the peak at low coupling rates.

In contrast to the bulk sample, the spins in the small sample are all located close to the resonator surface. This results in a peak at 25.9 Hz and 40.4 HZ and average coupling rates of 44.7 Hz and 87.7 Hz for the SR and CR, respectively. The coupling rates of the CR are in general larger than for the SR, as the B_1 field is more confined in the vicinity of the resonator surface (see Sec. 4.4.2). Additionally, the sample is placed near the magnetic field anti-node in the center of the meander inductor of the CR.

4.4.5 Comparison of the resonator parameters: experiments vs. finite element simulations

In the previous sections we exclusively presented results extracted from the FEM simulations. In this section, we now compare the simulations with actual experimental data. To this end, we fabricated two nominally identical sample chips, each containing eight CR. For each resonator, the length l_{cap} of one of the interdigital capacitor fingers was varied as well as the width w_{gs} of the metal strip separating the resonator from the signal line. The experiments were conducted in the flow-cryostat (see Chapter 3 for more details). The samples were cooled to $T = 1.5\,\mathrm{K}$ in zero field and the microwave transmission was measured. The resonance frequency as well as the external and internal quality factors are extracted with the previously described fitting method. As the resonators were measured without a silicon spin sample on top, the simulations were also performed without the additional silicon body on top of the resonator.

In Fig. 4.7, we plot the (a) magnitude $|S_{21}|^2$ as well as the (b) phase $\measuredangle S_{21}$ of the microwave transmission signal, relative to the resonance frequency of the resonator. We applied an additional phase shift of $e^{i\pi/1.2}$ to obtain a good agreement between the measured and simulated

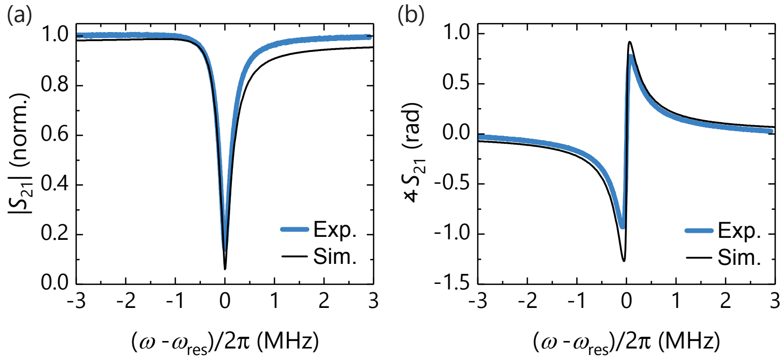

Fig. 4.7 Comparison of the simulated (black) and experimentally measured (blue) transmission spectrum of a CR. The experimental data has been calibrated using the algorithm described in Sec. 3.4.1. An additional phase shift of $e^{i\pi/1.2}$ was applied to the simulation data to obtain a good agreement with the experimental data.

phase signal. The simulation qualitatively reproduces the line shape of the absorption dip, including the line shape asymmetry.

Next, we compare the geometric tuning of the resonance frequency and the quality factor between simulations and experiments. In Fig. 4.8 (a), we plot the extracted resonance frequency $\omega_r/2\pi$ as a function of the capacitor finger length l_{cap}. By increasing l_{cap}, the total capacitance of the CR increases and therefore the resonance frequency decreases. The simulations (solid line) reproduce the measured results quantitatively within 1.6 % of the resonance frequency. We attribute the overestimation of the resonance frequency in the simulations to our modeling approach. In the finite element simulations, we neglect the effects of kinetic inductance as well as the finite penetration depth of the microwave current.

In Fig. 4.8 (b), we plot the external coupling rate $\kappa_{ext}/2\pi$ as a function of w_{gs}. As our microwave resonators are operated in the overcoupled regime (i.e. $\kappa_{ext} \gg \kappa_{int}$, the total loss rate and therefore the total quality factor is determined by κ_{ext}. Reducing w_{gs} leads to an increase of

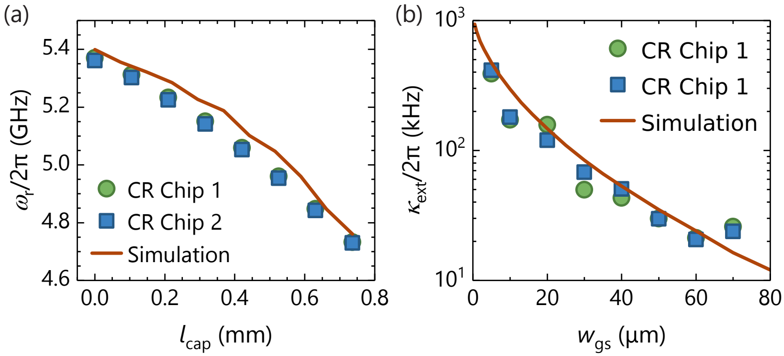

Fig. 4.8 Comparison of two chips containing several capacitively-shunted resonators (CR) with finite element simulations. Filled squares and circles represent experimental data. The solid orange lines are obtained from FEM. (a) Tuning of the resonance frequency by adjusting the length l_{cap} of one of the fingers of the capacitor. The resonance frequency drops with increasing length l_{cap}. (b) Tuning of external coupling κ_{ext} between resonator and feedline by changing the width w_{gs} of the small metal strip, separating the resonator from the signal line.

the coupling, as the microwave electromagnetic field of the feedline is screened less effectively. The reduction scales roughly exponential with w_{gs} and allows to tune the coupling over almost two orders of magnitude. As before, we find an excellent qualitative agreement between the experimental and the finite element model.

In summary, the simulations show an excellent agreement with the experimental data within a systematic offset. Finite element simulations allow a good estimation of the crucial resonator parameters and should therefore be the first step when tailoring microwave resonators for specific applications.

4.5 Temperature- and magnetic field robustness

In this section, we investigate the sensitivity of the microwave resonators in regard to temperature and magnetic field changes. As the resonators are used in the context of high-sensitivity ESR measurements, it is of importance that the resonance frequency as well as the linewidth remains constant over a large temperature and magnetic field range. We use Sample #1 without the phosphorus-doped silicon crystal for the measurements.

The resonance frequency of a superconducting microwave resonator depends on its inductance L and capacitance C. While the capacitance depends purely on geometry, the inductance consists of a magnetic inductance L_m and a kinetic inductance L_k. L_m is solely determined by the geometric inductance of the resonator and is associated with the energy stored in the magnetic field, while L_k is associated with the kinetic energy of the charge carriers due to their inertial mass [170].

The kinetic energy density of the superconducting charge carriers (cooper pairs) with density n_s is given by

$$E_\mathrm{kin} = \frac{1}{2} n_\mathrm{s} m_\mathrm{s} v_\mathrm{s}^2 = \frac{1}{2} \frac{m_\mathrm{s}}{n_\mathrm{s} q_\mathrm{s}^2} J_\mathrm{s}^2, \tag{4.14}$$

where $m_\mathrm{s} = 2m_\mathrm{e}$ is the mass of a cooper pair. In the last term we substituted the drift velocity v_s of the cooper pairs with the superconducting current density $J_\mathrm{s} = -n_\mathrm{s} q_\mathrm{s} v_\mathrm{s}$.

We can obtain an expression for the kinetic inductance per unit length L_k by equating Eq. 4.14 with an inductive energy as [171, 172]

$$\frac{1}{2} L_\mathrm{k} I^2 = \frac{1}{2} \frac{m_\mathrm{s}}{n_\mathrm{s} q_\mathrm{s}^2} \int_S J_\mathrm{s}^2 \, \mathrm{d}S = E_\mathrm{kin}, \tag{4.15}$$

where the second term includes a surface integral over the conductor cross sections. Introducing the London penetration depth $\lambda^2 = m_\mathrm{e}/\left(2\mu_0 n_\mathrm{s} e^2\right)$ [173] with the electron mass m_e and elementary charge e results in the expression

$$\frac{1}{2} L_\mathrm{k} I^2 = \frac{\mu_0 \lambda^2}{2} \int_S J_\mathrm{s}^2 \,\mathrm{d}S. \tag{4.16}$$

In general, the current density inside a superconductor is non-uniform, as it only penetrates the surface to a depth λ. For certain geometries, e.g. CPWs or striplines, the current distribution can be calculated using a conformal mapping method and an analytical expression for the kinetic inductance can be specified [171, 174]. The geometry of the CR, MR and SR can be well approximated by a straight, rectangular wire with width w, thickness d and length l. We can solve Eq. 4.16 for the following ases [175]:

- *Bulk conductor ($w \gg d \gg \lambda$)*: Here, the width w and thickness d is larger than the penetration depth. The current only flows in a narrow region near the surface. The cross-sectional area of the current flow is given by $2(w + d)\lambda \approx 2w\lambda$ (the small current density along the edges is ignored since $w \gg d$). L_k is then given by
$$L_\mathrm{k} = \frac{1}{2} \frac{\mu_0 \lambda}{w}. \tag{4.17}$$
- *Thin film ($w \gg \lambda \gg d$)*: For a thin film with a thickness much smaller than the penetration depth, we can assume a homogeneous current distribution $J_\mathrm{s} = I/(wd)$. The kinetic inductance per unit length is then given by
$$L_\mathrm{k} = \frac{\mu_0 \lambda^2}{wd}. \tag{4.18}$$
- *General case ($d \approx \lambda$)*: The film thickness of the resonators used in this thesis is often in the intermediate range, where the two limits

discussed above do not hold. In this case, the surface integral of the current density has to be calculated. The result is [175]

$$L_\mathrm{k} = \frac{\mu_0 \lambda}{w} \left[\coth\left(\frac{d}{2\lambda}\right) + \left(\frac{d}{2\lambda}\right) \operatorname{cosec}^2\left(\frac{d}{2\lambda}\right) \right]. \tag{4.19}$$

The temperature dependence of L_k can be related to changes of the magnetic field penetration depth λ. When the temperature of the superconductor increases, more and more quasiparticles are excited. The decrease of the cooper pair density in turn increases the penetration depth λ and thereby L_k. Empirically, the temperature dependence of the penetration depth is given by the Gorter-Casimir two-fluid model as [173]

$$\lambda(T) = \lambda(0) \left[1 - \left(\frac{T}{T_\mathrm{c}}\right)^4 \right]^{-1/2}, \tag{4.20}$$

where $\lambda(0)$ is the penetration depth for $T \to 0$. Assuming a homogeneous current distribution[5], we obtain an expression for the temperature dependence of the kinetic inductance

$$L_\mathrm{k}(T) = \frac{L_\mathrm{k}(0)}{1 - (T/T_\mathrm{c})^4}, \tag{4.21}$$

with $L_\mathrm{k}(0) = \mu_0 \lambda(0)/(wd)$.

When applying a magnetic field B_0 to the superconducting film, a screening current of

$$I_\mathrm{sc} \approx B_\perp \frac{w}{L_\mathrm{sc}} \tag{4.22}$$

is induced [177], which allows to link the applied magnetic field to the kinetic inductance. $B_\perp$ describes the magnetic field component of B_0 perpendicular to the film plane, w is the width of the superconducting wire and L_sc is the effective geometric inductance per unit length. For

---

[5] When comparing Eq. (4.18) and (4.19), assuming a homogeneous current distribution results in a deviation of less than 1 % for a penetration depth $\lambda = 90\,\mathrm{nm}$ and a wire thickness of $d = 150\,\mathrm{nm}$ [176].

small screening currents, the kinetic inductance scales quadratically with the screening current [178]

$$L_{\mathrm{k}}(I_{\mathrm{sc}}) \approx L_{\mathrm{k}}(0)\left[1 + \left(\frac{I_{\mathrm{sc}}}{I^*}\right)^2\right], \tag{4.23}$$

where I^* is a characteristic current on the order of the critical current. A similar relation can be derived when considering the field variation of the penetration depth λ [179–181].

In the following we analyze the temperature and magnetic field robustness of our resonators. The resonator sample (without a silicon spin sample) is cooled to the temperature T. We measure the microwave transmission $|S_{21}|^2$, while applying a static magnetic field B_0 in-plane of the superconducting film, parallel to the microwave feedline (see Sec. 3 for details).

4.5.1 Robustness of the resonance frequency

In the first part, we investigate the stability of the resonance frequency in regard to temperature and magnetic field changes. The resonance frequency is given by

$$\omega_{\mathrm{r}} = \frac{1}{\sqrt{LC}} = \frac{1}{\sqrt{C\,(L_{\mathrm{m}} + L_{\mathrm{k}})}}. \tag{4.24}$$

Assuming a change of the kinetic inductance that is small compared to the total inductance ($\Delta L_{\mathrm{k}} \ll L_{\mathrm{k}} + L_{\mathrm{m}}$), we can calculate the change of the resonance frequency using a Taylor expansion (see Appendix A2.1) in ΔL_{k} as

$$\frac{\omega_{\mathrm{r}}(L_{\mathrm{k}} + \Delta L_{\mathrm{k}})}{\omega_{\mathrm{r}}(L_{\mathrm{k}})} = 1 - \frac{1}{2}\frac{L_{\mathrm{k}}(0)}{L_{\mathrm{k}}(0) + L_{\mathrm{m}}}\left(1 - \frac{L_{\mathrm{k}}(T, B_0)}{L_{\mathrm{k}}(0)}\right). \tag{4.25}$$

Here, $L_{\mathrm{k}}(T, B_0)$ describes the kinetic inductance under the influence of temperature or magnetic field changes. The ratio $\alpha = \frac{L_{\mathrm{k}}(0)}{L_{\mathrm{k}}(0)+L_{\mathrm{m}}}$

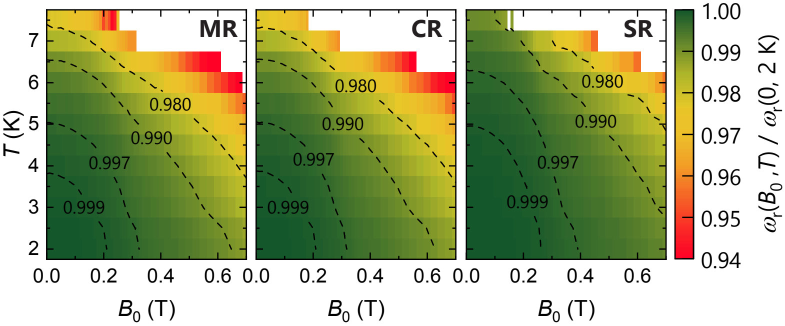

Fig. 4.9 Magnetic field and temperature robustness of the MR, CR and SR. The relative change of the resonance frequency compared to $T = 2\,\mathrm{K}$ and no applied magnetic field is encoded in the color-scale. The MR and CR are less robust at elevated temperatures and magnetic fields compared to the SR.

describes the kinetic inductance participation ratio at base temperature and zero-magnetic field, respectively.

Inserting the temperature dependence of the kinetic inductance (Eq. 4.21) results in

$$\frac{\omega_r(T)}{\omega_r(0)} = 1 - \frac{\alpha}{2}\left(1 - \frac{L_k(T)}{L_k(0)}\right). \tag{4.26}$$

We extract the resonance frequency of the MR, CR and SR from the measured microwave transmission $|S_{21}|^2$ and plot the relative frequency change $\omega_r(B_0, T)/\omega_r(0\,\mathrm{T}, 2\,\mathrm{K})$ as a function of magnetic field and temperature in Fig. 4.9. White regions in the plot correspond to measurements where no meaningful resonance dip could be fitted.

On a first glance, all three resonators show a qualitatively similar picture. The resonance frequency decreases when the magnetic field or temperature is increased. Additionally, the magnetic-field dependent shift is larger for elevated temperatures due to the temperature dependence of the critical field H_{c1} and H_{c2}. When comparing the contour lines (dashed lines) in Fig. 4.9, a quantitative difference between the SR and the MR/CR can be observed. For the SR, the decrease in

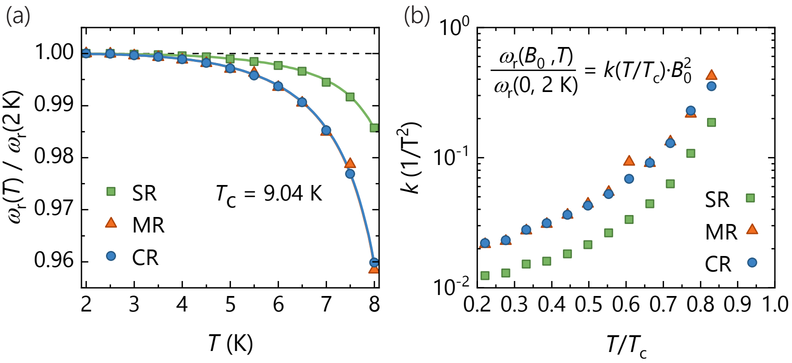

Fig. 4.10 Temperature dependence of the resonance frequency and a microwave resonator specific scaling factor. Data is extracted from Fig. 4.9 at $B_0 = 0$. Panel (a) shows the temperature dependence of the normalized resonance frequency indicating a characteristic drop close to T_c. Eq. 4.26 describes this behaviour quantitatively and allows to determine the contributions of the various inductances. (b) Temperature dependence of the scaling factor k, extracted from fitting Eq. 4.28 to the data with $B_0 < B_{c1}$. k describes the influence of the static magnetic field on the resonance frequency of the microwave resonator according to the equation shown in the panel.

resonance frequency sets in for $T \gtrapprox 5\,\mathrm{K}$ at zero-field and $B_0 \gtrapprox 0.3\,\mathrm{T}$ at low temperatures. For the CR and MR, these values are decreased to $T \gtrapprox 4\,\mathrm{K}$ and $B_0 \gtrapprox 0.2\,\mathrm{T}$.

We perform a more quantitative analysis by extracting the relative frequency change at zero-field as a function of temperature. We plot the extracted values in Fig. 4.10 (a). Again, the resonance frequency of the SR is more robust to temperature changes than for the MR or CR. We fit Eq. 4.26 simultaneously to all three datasets with T_c being a shared parameter and individual kinetic-inductance participation ratios α_i. From the fit we obtain $T_c = (9.04 \pm 0.03)\,\mathrm{K}$, which is comparable to literature values of bulk Nb and Nb thin films [176, 182–184].

For the participation ratio, we obtain for the CR $\alpha_{\mathrm{CR}} = 0.0509 \pm 0.0015$, for the MR $\alpha_{\mathrm{MR}} = 0.0512 \pm 0.0015$ and for the SR $\alpha_{\mathrm{SR}} = 0.0183 \pm 0.0061$. While for the MR and CR the kinetic inductance contributes ≈ 5.1 %

to the total inductance, the SR shows a much smaller contribution of 1.8 %. This difference in α is the reason for the more robust behavior, because the increase of the kinetic inductance with magnetic field and temperature has less impact to the total inductance.

The smaller kinetic inductance participation ratio for the SR can be explained by the contributions to the total inductance,

$$L = L_\mathrm{m} + L_\mathrm{k} = L_\mathrm{self} \pm L_\mathrm{mutual} + L_\mathrm{k}. \tag{4.27}$$

The geometric inductance L_m consists of the self-inductance L_self and the mutual inductance L_mutual. The self-inductance scales with the total wire length, its width and thickness. The mutual inductance is caused by the voltage induced by a neighboring strip. Depending on the current direction of neighboring strips, the mutual inductance can contribute positively or negatively to the total inductance. For the SR, the current flows parallel in adjacent strips in the two halves of the resonator, such that L_mutual is positive. For the MR and CR, the anti-parallel current flow leads to a negative contribution of L_mutual. Therefore, the total geometric inductance (which is temperature independent) of the SR is larger than for the MR and CR, leading to a more robust reaction to temperature changes.

We further analyze the magnetic field robustness of the resonators. Using Eq. (4.22) and (4.23), we obtain an expression for the frequency change due to an applied magnetic field [177]

$$\frac{\omega_\mathrm{r}(B)}{\omega_\mathrm{r}(0)} \approx 1 - k(T)B_0^2, \tag{4.28}$$

with the temperature-dependent scaling factor $k(T)$.

We fit Eq. (4.28) to the data presented in Fig. 4.9 and extract the scaling factor. We plot k as a function of $t = T/T_\mathrm{c}$ in Fig. 4.10 (b). The critical temperature is extracted from the fit of Eq. (4.26). The scaling factor shows a non-linear behavior and increases by more than one order of magnitude when the sample temperature approaches the critical temperature of the superconductor. Non-linear scaling factors $k(T/T_c)$ with values in the same order of magnitude have been reported for ceramic Type-II superconductors [185, 186]. The scaling factor of the SR is smaller than for the MR and CR by approximately a factor of 2 over the whole temperature range, indicating that the SR is more robust to field changes than the other two resonators. Again, this can be explained by the lower kinetic inductance participation ratio.

4.5.2 Robustness of the internal quality factor

In the second part, we analyze the stability of the internal quality factor of the resonator when the temperature and applied magnetic field changes. In order to maintain a high sensitivity in ESR spectroscopy, it is important that the quality factor of the resonator remains constant over a wide field and temperature range.

The internal microwave losses in superconducting resonators are caused by several effects that are microwave power and temperature dependent. At low microwave power, the coupling of the resonator to two-level systems (TLS) at the various interfaces of the superconductor are the main contributor to the microwave losses [160, 161]. This regime, however, is only reached when the microwave resonator is cooled to its quantum mechanical groundstate. In the temperature regime where our experiments are performed, the dominating loss source is quasiparticle generation by thermal activation [159]. This mechanism becomes relevant at temperatures $T \gtrapprox 0.1T_c$ [187]. The conductivity of the superconducting material in this regime is described by the *Mattis-Bardeen* theory [159, 168].

From the measured microwave transmission $|S_{21}|^2$ at zero-field, presented in Fig. 4.9, we extract the internal quality factor Q_{int}. We plot Q_{int} as a function of temperature in Fig. 4.11. At $T = 2\,\text{K}$, we obtain the largest $Q_{\text{int}} = 35000$ for the SR. The CR shows a comparable quality factor above 25000, while the MR shows a drastically reduced $Q_{\text{int}} = 7000$.

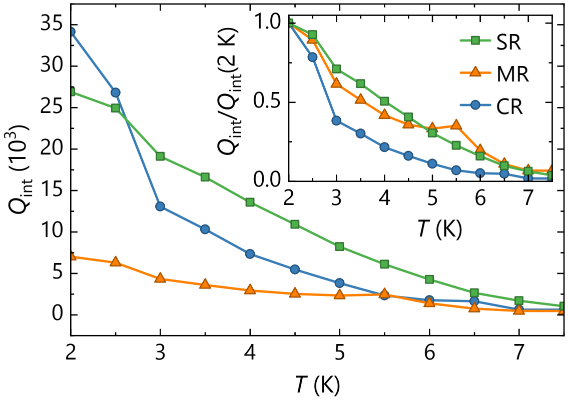

Fig. 4.11 Temperature robustness of the internal quality factor Q_{int}. The data is obtained from the microwave transmission $|S_{21}|^2$ at zero-field, presented in Fig. 4.9. The inset shows the relative change $Q_{\mathrm{int}}/Q_{\mathrm{int}}(T = 2\,\mathrm{K})$ compared to the value at 2 K.

As the resonators are patterned on the same sample chip, quasiparticle generation or dielectric losses are not responsible for this reduction, as it would affect all resonators. One possible origin of the reduced internal quality factor of the MR could be the increased wire length, as an increased area where the electric field is stored, leads to an increase in resistive losses [158]. As the temperature approaches T_c, Q_{int} decreases drastically and approaches zero, rendering the extraction of resonator parameters close to T_c virtually impossible.

For increasing temperature, the quasiparticle generation increases and thereby the Q_{int} decreases. As the external quality factor is fixed by the geometry, the total quality factor decreases accordingly. The inset in Fig. 4.11 shows the relative change $Q_{\mathrm{int}}/Q_{\mathrm{int}}(T = 2\,\mathrm{K})$. Here, the SR shows the most robust behavior, while the internal quality of the CR decreases rapidly with temperature. For the SR, a reduction by 50 % is obtained, when the temperature increases to 4 K. For the MR and CR this point is at 3.5 K and 2.9 K, respectively.

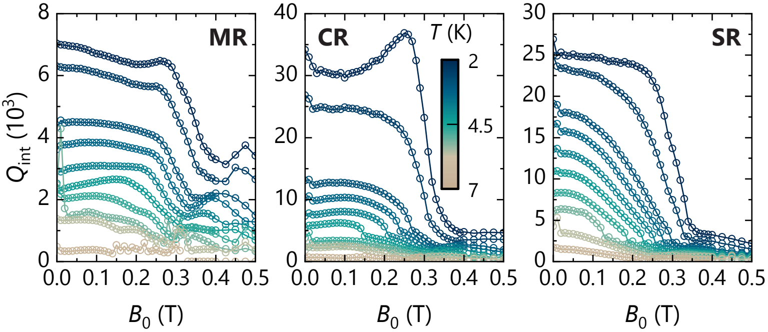

Fig. 4.12 Field robustness of the internal quality factor for the three different resonators. The CR and the SR show the largest internal quality factor up to approximately 3.5×10^4. Q_{int} decreases drastically for magnetic fields $B_0 > B_{\mathrm{c1}} \approx 0.3\,\mathrm{T}$.

The field robustness of the internal quality factor is analyzed in Fig. 4.12. We plot Q_{int} for the three resonators as a function of the applied in-plane magnetic field for several temperatures between 2 K and 7 K.

For small magnetic fields, the internal quality factor remains constant for all resonators. However, at a magnetic field of approximately 0.3 T, Q_{int} drastically reduces for all three resonators. We attribute this reduction of Q_{int} to flux vortices penetrating the superconducting film, i.e. the superconducting being in the Shubnikov phase. Even a very small number of flux vortices in the vicinity of a microwave resonator can substantially reduce the quality factor [188–190]. The first critical field of bulk Niobium at $t = T/T_{\mathrm{c}} = 2\,\mathrm{K}/9.04\,\mathrm{K} \approx 0.22$ is $B_{c1} = 0.13\,\mathrm{T}$ [184]. However, if the magnetic field is applied parallel to a superconducting film with a thickness d in the order of the penetration depth λ, the critical field is increased according to [191]

$$\frac{B_{c1\parallel}}{B_{c1}} = \frac{2\sqrt{6}\lambda}{d}. \tag{4.29}$$

With this equation, we obtain $B_{c1\|} \approx 0.34\,\mathrm{T}$ for $\lambda = 80\,\mathrm{nm}$ [176], which is in good agreement to our measurement data. We additionally observe a peak of the internal quality factor at $T = 2\,\mathrm{K}$ at magnetic fields smaller than H_{c1} for the MR and CR. The origin of this effect is still unclear.

4.5.3 Out-of-plane magnetic field

We performed additional experiments where the magnetic field is applied in the out-of-plane direction. In Fig. 4.13 (a) and (c) we plot $\omega_{\mathrm{r}}/2\pi$ and Q_{int} as a function of the applied out-of-plane magnetic field, normalized to their values at zero-field. The dashed line indicates the first critical field B_{c1}. We see again a similar picture as previously: The resonance frequency as well as the internal quality factor decrease with increasing magnetic field. The SR shows a smaller change of the resonance frequency compared to the MR and CR. The internal quality factor of all three resonators shows a similar behavior. For fields $B < B_{\mathrm{c1}}$, Q_{int} remains constant (MR, CR) or decreases only slightly (SR), while for fields exceeding the critical fields, Q_{int} drops drastically and approaches zero.

The data in Fig. 4.13 (b) and (d) is recorded by applying a fixed magnetic field $B_{\mathrm{oop}} = 10\,\mathrm{mT}$, which is then rotated from the out-of-plane ($\theta = 0, 180°$) to the in-plane ($\theta = 90°, 270°$) direction. For the change of the resonance frequency, we observe a sinusoidal signal, as the out-of-plane component of the magnetic field is responsible for flux penetration. Again, the SR is less sensitive to changes of the applied magnetic field compared to the MR and CR. The data of the internal quality factor is less clear. For the SR and MR we again obtain a sinusoidal signal, while the data of the CR is less pronounced.

Measurements with a magnetic field along the out-of-plane direction are a crucial benchmark for superconducting resonators. In the out-of-plane orientation, magnetic flux vortices can penetrate the superconducting film more readily, therefore the critical field $B_{\mathrm{c1}} = 19\,\mathrm{mT}$

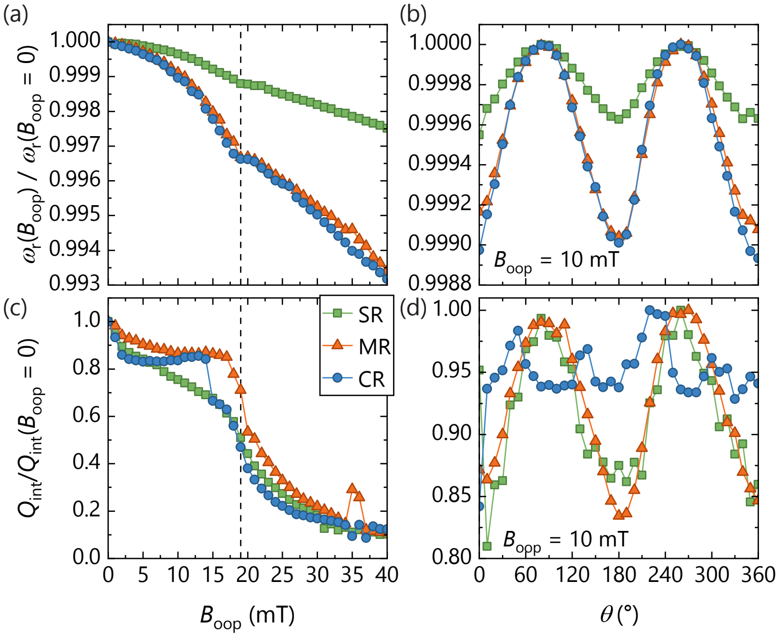

Fig. 4.13 Field robustness of the resonance frequency $\omega_r/2\pi$ (a, b) and internal quality factor Q_{int} (c, d) when a static magnetic field is applied in the out-of-plane direction (perpendicular to the film). In panel (a) and (c) the out-of-plane field B_{oop} is increased up to 40 mT. In (b) and (d), a fixed magnetic field of B_{oop} = 10 mT is rotated from the out-of-plane ($\theta = 0, 180°$) to the in-plane direction ($\theta = 90°, 270°$).

(dashed line) is more than one order of magnitude smaller than for the in-plane direction. When applying moderate in-plane fields of 0.3 T, a misalignment between the film plane and the magnetic field direction of 5° would result in an out-of-plane component of 26 mT. A careful sample alignment is therefore of utmost importance.

4.5.4 Further improvements of the resonator performance

The results presented in this section describe the robustness of superconducting microwave resonators with respect to magnetic field and temperature changes. However, our resonator designs are only a first attempt and further optimizations are possible.

The first and obvious possibility to increase the magnetic field and temperature robustness is to change the superconducting material to a material with higher critical field and critical temperature. For our resonators, we used Niobium as the superconducting material. Superconducting resonators fabricated from high-temperature ceramic superconductors allow operation up to a temperature of 70 K and magnetic fields of 7 T [192]. Resonators fabricated from NbTiN show good performance up to magnetic fields of 6 T parallel to the film surface and 0.5 T perpendicular to the film surface [193, 194]. Additionally, the larger critical temperature up to $T_\mathrm{c} \approx 16\,\mathrm{K}$ [195, 196] enables operation at even more elevated temperatures. Note that an increase of the critical temperature in general also leads to an increase of the kinetic inductance [178]. Therefore, it is not clear if the increased critical temperature and kinetic inductance also leads to an increased robustness.

Furthermore, the resonator geometry can be optimized. Increasing the cross-sectional area of the superconducting wires decreases the kinetic inductance participation ratio [172]. The magnetic field robustness can be improved by controlling the penetration and movement of flux vortices in the superconducting film. For example, artificial defects (holes) in the ground plane of a superconducting CPWR pin the flux vortices in the ground plane [194, 197]. Another approach is to reduce the area of the ground planes of a CPWR to reduce flux focusing [198].

Of course, the inverse process is also possible: By increasing the kinetic inductance participation ratio, the sensitivity of the resonator in regard to an externally applied magnetic field is used to tune the resonance frequency in-situ [177, 199]. Here, the material and geometry of the resonator is optimized to achieve kinetic inductance participation ratios up to 70 % [177]. Another possibility to tune the inductance of a superconducting resonator is to directly inject a DC current [172, 200]. Tunable microwave resonators can also be instructed by including a nano-SQUID, effectively creating a magnetic field-controllable inductance [201].

4.6 Quantitative modeling of the collective spin-resonator coupling

In the following section, we employ our finite element simulations to quantitatively predict the collective spin-photon coupling rate g_{eff} between a spin ensemble and the microwave resonator. The experiments in this section are conducted using Sample #1. We first present continuous-wave ESR measurements to demonstrate the feasibility of our resonators for ESR, followed by an analysis of the collective coupling. In the last part, we present measurements on a power-dependent saturation effect and show that our modeled prediction confirms the computed microwave magnetic field distribution.

The experimental data in this section is recorded at $T = 1.5\,\mathrm{K}$, i.e. the resonator is not in its quantum ground state. As we will show, the number of photons in the resonator, n_{ph}, is small compared to the number of spins, N. Chiorescu *et al.* demonstrated that the transition to the classical resonance mechanism only occurs for $n_{\mathrm{ph}} > N$. Therefore, by taking the thermal spin polarization into account [56] our modeling approach is also applicable to ultra-sensitive ESR measurements, where the resonator is in its quantum ground state (see Sec. 5).

4.6.1 Continuous-wave spectroscopy

We conduct continuous-wave ESR spectroscopy by applying a continuous microwave signal to probe the microwave transmission through the sample and simulatenously varying the applied magnetic field. The change of the microwave absorption then yields the ESR spectrum of the spin system. In our experiments, this is accomplished by extracting the resonator linewidth as a function of the magnetic field. From these spectra, information about the spin system (e.g. g-factor, hyperfine interactions) can be obtained [12]. Furthermore, we can extract the collective coupling rate between the spin system and the microwave resonator from these spectra.

For our experiments, we place a phosphorus doped $^{\mathrm{nat}}$Si:P sample with dimensions of $3.4 \times 3.4 \times 0.42\,\mathrm{mm}^3$ and a donor density of $\rho = 2 \times 10^{17}\,\mathrm{cm}^{-3}$ in flip-chip geometry on top of the microwave resonators of the sample chip. The sample is cooled to $T = 1.55\,\mathrm{K}$. The microwave power applied to the sample is $P_{\mathrm{S}} = -100\,\mathrm{dBm}$. The input and output lines are attenuated at low temperature by 30 dB and 20 dB, respectively, to avoid saturation by thermal noise photons generated at room temperature.

Fig. 4.14 (a) displays the normalized microwave transmission $|S_{21}|^2$ as a function of the probe frequency ω and the static applied magnetic field B_0, relative to the center resonance field B_{res}. When the probe tone is in resonance with the capacitively-shunted resonator (CR), the transmission drops to 0.35. The resonance frequency shifts throughout the displayed magnetic field range due to the magnetic field dependence of the kinetic inductance (see previous section).

We observe two distinct features at $\pm 1.7\,\mathrm{mT}$, which we attribute to the hyperfine transitions of phosphorus donors in silicon. The observed hyperfine splitting of 3.4 mT is smaller than the expected literature

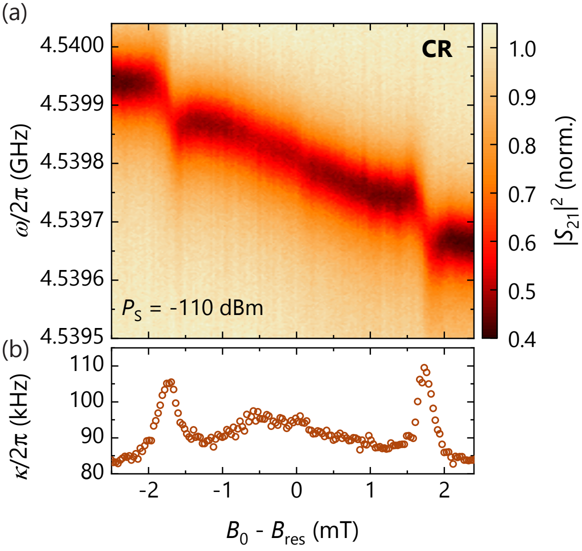

Fig. 4.14 (a) Transmission $|S_{21}|^2$ as a function of frequency and applied magnetic field. The frequency-dependent absorption dip corresponds to the resonator, while the two distinct features indicate the phosphorus hyperfine transitions. (b) Extracted linewidth $\kappa/2\pi$ (HWHM) as a function of the magnetic field. The two peaks correspond to the hyperfine transitions. The features at intermediate fields are compatible with Pb_0/Pb_1 dangling bond defects and P_2 dimers. (See text for details)

value of 4.2 mT [81]. We attribute this reduction to the presence of strain [83, 85, 86], caused by the different thermal expansion coefficients of the silicon crystal and the copper sample box.

A more detailed analysis is possible by extracting the linewidth $\kappa/2\pi$ of the microwave resonator for each applied magnetic field. This is analogous to a conventional continuous-wave ESR experiment, where the absorption signal of the microwave resonator is measured [12]. We plot $\kappa/2\pi$ as a function of the applied magnetic field in Fig. 4.14 (b). Here, we again observe two distinct peaks, corresponding to the two hyperfine transitions of the phosphorus donors. Additionally, we observe several broad features in the magnetic field range between the two peaks:

1. A broad peak at a field of ≈ -0.5 mT, which is compatible with dangling bond defects at the Si/SiO$_2$ interface, known as Pb$_0$/Pb$_1$ defects [202, 203].

2. A sharp peak at a field of ≈ 0 mT (*central pair line*), which we attribute to exchange-coupled donor pairs forming P$_2$ dimers [87, 88].

3. A broad background signal, underlying the two previous features, known as *broad center line* (BCL). The BCL is caused by interactions between higher-order clusters (three or more donors) [98].

Note that we specify the resonance fields of these features relative to the center magnetic field between the two hyperfine transitions. The static magnetic field in the experiments presented in this section is generated by a large superconducting solenoid, which introduces a significant offset in the applied magnetic field in the order of 10 mT. However, as the absolute magnetic fields are only of subordinate interest, we decided to plot the magnetic fields relative to the center magnetic field.

The applied microwave power of $P_S = -100$ dBm or 100 fW used in Fig. 4.14 corresponds to a photon number of $n \approx 7.8 \times 10^4$ for $\omega = \omega_r$. Event at these low powers, we already observe the onset of saturation when driving the hyperfine transitions. Although the analysis of the collective coupling in the presence of power saturation (cf. Sec. 4.6.3) is possible, we choose a dataset of the CR, where the microwave power is decreased to $-110\,\mathrm{dBm}$ ($n \approx 2.5 \times 10^3$). This allows a more simple and pedagogical analysis of the collective coupling in the following. We also note the importance of the additional attenuators mounted on the sample stage of the experimental setup to suppress thermal noise photons generated at room temperature. Without this attenuation, we already observe saturation effects at the lowest microwave power applied to the sample and no measurement in the unsaturated regime would be possible.

4.6.2 Analysis of the collective coupling

A detailed analysis of the microwave transmission in the vicinity of the ESR transition allows to determine the effective coupling strength. Here, we will exemplarily show such an analysis of the high-field hyperfine transition of the phosphorus donors using a CR resonator. We further extract the collective coupling rate and compare it to theoretical calculations, taking into account the three-dimensional microwave magnetic field distribution.

In a first step, we analyze the microwave transmission at each magnetic field step using the fitting method described in Sec. 3.4.1. In Fig. 4.15 (a), we plot the extracted linewidth $\kappa/2\pi$ against the applied static field, relative to the resonance field of the high-field hyperfine transition. The applied microwave power to the sample is set to $P_\mathrm{S} = -110\,\mathrm{dBm}$ in order to avoid saturating the ESR transition.

The exact line shape of the ESR transition depends on the residual ^{29}Si concentration in the sample [97]. For small ^{29}Si concentrations, the line shape is given by a Lorentzian, while for a large concentration the line shape can be described by a Gaussian. The transition point between the two line shapes occurs at a concentration of $\approx 5\,\%$. In our experiments, we use Si with a natural abundance of ^{29}Si nuclei of

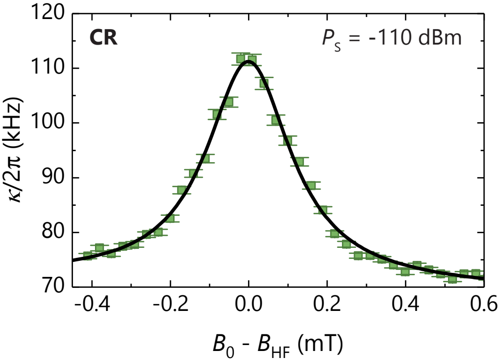

Fig. 4.15 Measured linewidth $\kappa/2\pi$ of the capacitively-shunted resonator for the high-field hyperfine transitions of phosphorus donors in $^{\mathrm{nat}}$Si. The solid line is a fit to Eq. (4.30) to extract $g_{\mathrm{eff}}/2\pi$, $\kappa_c/2\pi$ and $\gamma_{\mathrm{s}}/2\pi$.

4.67 % [125]. The exact line shape of the ESR transition is therefore not immediately clear.

To this end, we use a Pseudo-Voigt profile to fit the peak, which is a linear combination of a Lorentzian and a Gaussian:

$$\kappa(\Delta B) = \eta \cdot L(\Delta B) + (1-\eta) \cdot G(\Delta B). \tag{4.30}$$

L and G are the Lorentzian and Gaussian line shapes, respectively, and are given by [204]

$$L(\Delta B) = \kappa_c + \frac{g_{\mathrm{eff}}^2 \gamma_{\mathrm{s}}}{\gamma_{\mathrm{s}} + \Delta B^2}, \tag{4.31}$$

$$G(\Delta B) = \kappa_c + \frac{g_{\mathrm{eff}}^2}{\gamma_{\mathrm{s}}} \exp\left(\frac{-\Delta B^2}{2\gamma_{\mathrm{s}}^2}\right), \tag{4.32}$$

with the magnetic field detuning $\Delta B = \frac{g_{\mathrm{e}}\mu_{\mathrm{B}}}{\hbar}(B_0 - B_{\mathrm{HF}})$. This function can be used to extract the collective coupling g_{eff}, the spin linewidth γ_{s} as well as the off-resonant linewidth κ_c of the microwave resonator.

We fit Eq. 4.30 in combination with a linear background to the data presented in Fig. 4.15 (a) (solid line). We obtain a coefficient $\eta = 0.93$, indicating that the line shape is primarily given by a Lorentzian. We extract a collective coupling rate $g_{\mathrm{eff}}/2\pi = (438 \pm 32)\,\mathrm{kHz}$. The resonator linewidth at $\Delta B = 0.49\,\mathrm{mT}$ is $\kappa_c/2\pi = (72.4 \pm 0.5)\,\mathrm{kHz}$. The inhomogeneously broadened spin linewidth (half-width at half maximum) is $\gamma_{\mathrm{s}}/2\pi = (3.67 \pm 0.13)\,\mathrm{MHz}$, corresponding to a magnetic field linewidth $\delta B = (131.1 \pm 4.6)\,\mu\mathrm{T}$.

From the extracted coupling and loss parameters, the cooperativity is given by

$$C = \frac{g_{\mathrm{eff}}}{\kappa_{\mathrm{c}}\gamma_{\mathrm{s}}} = 0.72, \tag{4.33}$$

allowing to put the observed coupling in the weak coupling regime. This justifies our simplified approach of extracting the coupling rate via Eq. 4.30.

Sources of inhomogeneous broadening

There are several sources responsible for the inhomogeneous broadening of phosphorus-doped $^{\mathrm{nat}}\mathrm{Si}$. An inhomogeneous static external magnetic field B_0 results in a variation of the Larmor frequencies across the spin sample [13]. Additionally, unresolved hyperfine splittings due to a strain-induced shift of the hyperfine interaction [83, 85, 86] or due to abundant $^{29}\mathrm{Si}$ nuclei can lead to inhomogeneous broadening.

In our experiment, the magnetic field inhomogeneity of the superconducting solenoid is specified to be smaller than 10×10^{-4} over the sample volume of $1\,\mathrm{cm}^3$. At a maximum magnetic field of 200 mT, this would result in an additional broadening of less than 20 μT. An inhomogeneity of the static magnetic field is therefore not responsible for the measured linewidth.

The reduced hyperfine interaction of 3.4 mT compared to the literature value of 4.2 mT (cf. Section 4.6.1) suggests that the Si:P crystal is subject to excessive strain due to the different thermal expansion coefficients of the silicon crystal and the sample copper box. However, in order for the strain to result in a inhomogeneous broadening, a strain distribution across the Si:P crystal has to be present [13]. The Si:P crystal is pressed onto the resonator chip with a screw. As the cross-section area of the screw head is one order of magnitude larger than the average resonator cross-section area and due to the presence of a piece of tape acting as a buffer layer, we assume that the strain exerted on the sample is homogeneous. Furthermore, an inhomogeneous strain distribution would also lead to asymmetrical lines in the ESR spectrum, which we do not observe. We therefore conclude that a strain-induced hyperfine splitting is not responsible for the inhomogeneous broadening.

Therefore, we assume the dominant source of inhomogeneous broadening in our experiment is indeed the hyperfine interaction between the phosphorus electron spin and the nuclear spin of abundant ^{29}Si nuclei. Indeed, the measured linewidth of $(131.1 \pm 4.6)\,\mu$T is in agreement with literature values for $^{\mathrm{nat}}$Si with a natural abundance of 4.7 % ^{29}Si nuclei [97].

Calculation of g_{eff}

Using the formalism described in Sec. 4.2, we can now give a theoretical estimate of g_{eff}. To this end, we assume an effective spin density $\rho_{\mathrm{eff}} = 0.5\rho$, as the total number of spins contribute equally to each hyperfine transition. At $T = 1.55\,$K and with the magnetic field on resonance, the thermal spin polarization is 1.9 %, further reducing the number of spins participating in the coupling. Using Eq. 4.10 together with the simulated microwave magnetic field distribution, we obtain a theoretical coupling rate for the CR of $g_{\mathrm{eff,inhom.}} = 645.1\,$kHz. This over-estimates the measured value by more than 40 %. We attribute this deviation to a finite gap between the resonator and the spin ensemble, reducing the effective filling factor [56].

Using the simulated microwave magnetic field distribution, we are able to calculate the filling factor R_{yz} in the presence of a small gap

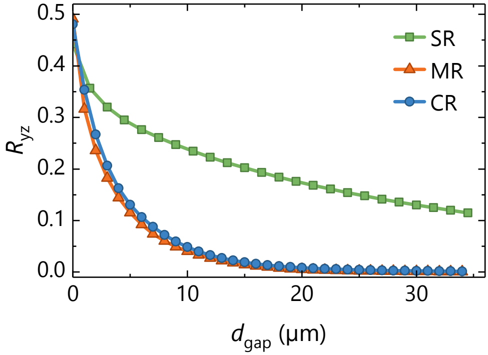

Fig. 4.16 Dependence of the filling factor R_{yz} on a finite gap d_{gap} between the resonator and the spin sample. A reduction of R_{yz} from the ideal value (dashed line) is due to magnetic field components parallel to the static magnetic field. The CR and MR show a more significant decrease compared to the SR due to the short decay length of the dynamic magnetic field.

using Eq. (4.7). We plot R_{yz} as a function of the gap width d_{gap} in Fig. 4.16.

The filling factor exhibits a qualitative difference between the CR/MR and the SR due to the different decay lengths of the microwave magnetic field. The CR and MR are very sensitive to a small gap due to the short decay length. In contrast, the SR is less sensitive due to the larger mode volume and decay length. This suggests the use of the SR for a flip-chip sample mounting, where small gaps in the order of a few micrometer are common. Note that the calculation of R_{yz} also takes the excitation condition for an ESR transition into account, i.e. magnetic field components along the x direction do not contribute to the filling factor. This results in different maximum filling factors $R_{yz,\text{max}}$ for the three different resonator designs, listed in Table 4.3. The SR offers the lowest maximum filling factor due to the wires running along the y axis.

Table 4.3 Summary of the collective coupling parameters extracted for the three resonator geometries. The collective coupling rates g_{eff} are extracted at $T = 1.55\,\mathrm{K}$ using the formalism described in the text. The theoretical values are calculated using Eq. 4.10. The gap width is determined using the data in Fig. 4.16. The $T_1 T_2^*$ product is determined from the power saturation behavior, see Sec. 4.6.3.

Resonator	$R_{yz,\mathrm{max}}$	P_{S} (dBm)	$g_{\mathrm{eff,exp.}}$ (kHz)	$g_{\mathrm{eff,theo.}}$ (kHz)	d_{gap} (µm)	$T_1 T_2^*$ $1 \times 10^{-10}\,\mathrm{s}^2$
SR	0.44	-115	438 ± 32	511.2	2.86 ± 1.16	0.13 ± 0.09
MR	0.49	-115	461 ± 32	627.6	2.23 ± 0.19	1.07 ± 0.31
CR	0.48	-110	384 ± 8.4	658.0	1.78 ± 0.08	5.75 ± 0.65

The data presented in Fig. 4.16 allows to estimate the nominal gap between the spin sample and the resonator plane. The measured collective coupling rate of (384.0 ± 8.4) kHz is in correspondence with a gap of $d_{\mathrm{gap,CR}} = (1.78 \pm 8.40)\,\mu\mathrm{m}$. The same analysis was performed for the other two geometries and the results are listed in Table 4.3. The extracted gap widths for the SR and MR agree within the error bars, but are longer than the value for the CR. The reason for this deviation might be that the measurement used for the analysis of the CR was performed at a larger microwave power than for the SR and MR. A possible weak power saturation might reduce the measure collective coupling rate, which in the end leads to an underestimation of the gap width.

Number of addressed spins

The measured collective coupling rate in combination with the single spin-photon coupling distribution can be used to estimate the number of spins addressed in the measurement. The collective coupling rate is given by Eq. (2.60) as

$$g_{\mathrm{eff}} = \sqrt{N_{\mathrm{spin}}} g_0, \tag{4.34}$$

where N_{spin} is the number of spins and g_0 is the single spin-photon coupling rate. In Sec. 4.4.4, we estimated the mean single-spin photon coupling rate $g_{0,\mathrm{mean}}$ for the CR from our finite element simluations. With the numerical values of $g_{\mathrm{eff}} = 384\,\mathrm{kHz}$ (see Table 4.3) and $g_{0,\mathrm{mean}} = 8.33\,\mathrm{Hz}$, we can solve Eq. (4.34) for N and obtain for the number of probed spins of the high-field hyperfine transition

$$N_{\mathrm{spin}} = \frac{g_{\mathrm{eff}}^2}{g_{0,\mathrm{mean}}^2} = 2.125 \times 10^9. \tag{4.35}$$

The number of spins addressed in the measurement can be used to quantify the spin sensitivity. It is defined as the minimum number of spins, which is still detectable by the spectrometer, and is given by [12]

$$N_{\mathrm{min}} = \frac{N_{\mathrm{spin}}}{\mathrm{SNR}}, \tag{4.36}$$

where SNR is the signal-to-noise ratio. We calculate the signal-to-noise ratio as the ratio between the signal amplitude and the standard deviation of the baseline noise of the data presented in Fig. 4.15 and obtain a signal-to-noise ratio SNR = 29.54. With this, the minimum number of spins is given as $N_{\mathrm{min}} = 7.2 \times 10^7$, which is about two order magnitude smaller than for commercially available ESR spectrometers [205].

We now compare the number of probed spins to the number of photons in the resonator. For the applied probe power of $P_{\mathrm{S}} = -110\,\mathrm{dBm}$ we obtain a photon number $n_{\mathrm{ph}} = 2.5 \times 10^3$ using Eq. (2.39). Since our measurements are still in the low-excitation regime with $N_{\mathrm{CR}} \gg n_{\mathrm{ph}}$, our modeling of the collective coupling rate is valid, even though the resonator is not in its quantum ground state [111]. Applying this method to measurements in the regime of ultra-sensitive EPR is therefore possible simply by taking the temperature dependent spin polarization into account. Assuming a spin polarization of 100 %, which is achieved for temperatures in the millikelvin range, we expect a collective coupling rate of $g_{\mathrm{eff},\,100\,\%} = 2.785\,\mathrm{MHz}$ and a cooperativity[6]

---

[6] We use the values of κ_{c} and γ_{s} determined at 1.5 K for the calculation of the cooperativity.

$C_{100\,\%} \approx 29$, indicating strong coupling between the spin ensemble and the microwave resonator.

4.6.3 Power saturation

Saturation effects in continuous-wave ESR experiments are a well-known phenomenon and have been used to extract the coherence and energy relaxation time prior to the advance of pulsed ESR. Saturation effects can be understood as a competition between the applied microwave power saturating the ESR line and the spin-lattice relaxation restoring the excess spin population [206]. The ESR signal is proportional to the polarization, which is the difference between the two populations of the two states of a spin transition [13]. For large microwave powers and long relaxation times, the probability of the spins populating each state becomes equal and thus the polarization decreases to zero. We then speak of a saturation of the ESR signal, as no population difference is present anymore.

With increasing microwave power levels, more spins are driven into saturation. This effectively reduces the number of spins N, which participate in the coupling, leading to a decoupling of the spin system from the microwave resonator [69]. In the following, we derive the so-called *saturation factor* S allowing us to describe the reduction of the collective coupling rate, based on the seminal work by Portis [207] and Castner [206]. The saturation factor depends on the microwave magnetic field amplitude B_1, therefore it is also subject to spatial variations of the microwave magnetic field of our resonators. In the following, we calculate S based on the simulated 3D microwave magnetic field distribution. The results in this section serve as a further validation of the simulated microwave magnetic field distribution.

In the following, we derive the saturation factor for the general case of a $S = 1/2$ system. We start with the population difference, $n = N_- - N_+$, where N_- and N_+ describe the number of spins in the lower-energy and higher-energy spin state. The ratio N_+/N_- is given by a Boltzmann distribution [56, 207]

$$\frac{N_+}{N_-} = \exp\left(-\hbar\omega_\mathrm{s}/k_\mathrm{B}T\right), \tag{4.37}$$

where $\omega_\mathrm{s} = g\mu_\mathrm{B}B_0/\hbar$ is the Larmor frequency and T is the sample temperature in thermal equilibrium. The rate of change of n is given by

$$\frac{\mathrm{d}n}{\mathrm{d}t} = \left(\frac{\mathrm{d}n}{\mathrm{d}t}\right)_\mathrm{rf} + \left(\frac{\mathrm{d}n}{\mathrm{d}t}\right)_\mathrm{sl}. \tag{4.38}$$

The two terms on the right-hand side describe the change of the population difference due to (i) interaction with the microwave radiation field and (ii) spin-lattice relaxation. They are given by [206]

$$\left(\frac{\mathrm{d}n}{\mathrm{d}t}\right)_\mathrm{rf} = -\pi\gamma^2 B_1^2 g(\omega-\omega_\mathrm{s})n, \tag{4.39}$$

$$\left(\frac{\mathrm{d}n}{\mathrm{d}t}\right)_\mathrm{sl} = \frac{(n_0-n)}{T_1}, \tag{4.40}$$

where $g(\omega-\omega_\mathrm{s})$ is the normalized shape function of the ESR transition [207], n_0 is the thermal equilibrium value of the population difference and $\gamma = g_\mathrm{e}\mu_\mathrm{B}/\hbar$ is the gyromagnetic ratio. In the steady-state, $\mathrm{d}n/\mathrm{d}t = 0$ and therefore

$$n = \frac{n_0}{1+\gamma^2 B_1^2 g(\omega-\omega_\mathrm{s})T_1}. \tag{4.41}$$

The rate at which power is absorbed from the microwave radiation field is $P = \frac{1}{2}\hbar\omega(\mathrm{d}n/\mathrm{d}t)_\mathrm{rf}$ [207]. At the same time, the absorption susceptibility χ'' is related to the absorbed microwave power by $P = \frac{1}{2}\chi'' B_1^2$ [12]. Combining this with Eq. (4.41) results in an expression for the absorption susceptibility

$$\chi''(\omega-\omega', B_1) = \frac{1}{2}\chi_0\omega_\mathrm{s}\frac{\pi g(\omega-\omega')}{1+\pi\gamma^2 B_1^2 T_1 g(\omega-\omega')}, \tag{4.42}$$

with the static susceptibility $\chi_0 \gamma^2 \hbar n_0 / 2\omega_0$.

So far, we described the saturation behavior of a homogeneously broadened transition. In the case of an inhomogeneous broadening, the ESR transition consists of several overlapping homogeneously broadened spin packets, precessing at different Larmor frequencies [207]. The total absorption of an ESR line is then given by [208]

$$A_{\mathrm{inh}}(\omega, B_1) = \int_0^\infty \chi''(\omega - \omega', B_1) \cdot h(\omega' - \omega_{\mathrm{s}})\,\mathrm{d}\omega', \tag{4.43}$$

where the integral includes all homogeneously broadened spin packets centered around ω' and $h(\omega' - \omega_{\mathrm{s}})$ is the envelope function of the inhomogeneously broadened line centered around ω_{s} and normalized so that the area under the curve is 1.

If the homogeneous width of the spin packets is small compared to the inhomogeneous broadening, $g(\omega - \omega')$ is only non-zero in the vicinity of $\omega \approx \omega'$. As $h(\omega' - \omega_{\mathrm{s}})$ varies only slowly in this frequency regime, it can be replaced by $h(\omega - \omega_{\mathrm{s}})$ and the integral in Eq. (4.43) can be separated [208]:

$$A_{\mathrm{inh}}(\omega, B_1) = h(\omega - \omega_{\mathrm{s}}) \cdot \int_0^\infty \chi''(\omega - \omega', B_1)\,\mathrm{d}\omega'. \tag{4.44}$$

Assuming that the line shape of the individual spin packet is Lorentzian, the shape function will be [207]

$$g(\omega - \omega') = \frac{T_2^*}{\pi} \frac{1}{1 + T_2^{*2}(\omega - \omega')^2}, \tag{4.45}$$

and the integral in Eq. (4.44) evaluates to the saturation factor [206]

$$S = \frac{S_0}{\left(1 + \gamma^2 B_1 T_1 T_2^*\right)^{1/2}}, \tag{4.46}$$

where S_0 includes all B_1 independent contributions. As S depends on the microwave magnetic field amplitude B_1, it is also spatially dependent in the case of an inhomogeneous B_1 distribution. Furthermore, the saturation factor can be used to extract the product $T_1T_2^*$ [206].

In a continuous-wave ESR experiment, the signal strength increases with B_1, but is reduced by the saturation factor S [12]. We obtain a new expression for the filling factor (cf. Eq. (4.9)) given by

$$R_{\mathrm{yz,sat}} = \frac{\sum_V \left| S\left(B_{1,\mathrm{sim}}^{yz}\left(\vec{r}\right)\right) \cdot B_{1,\mathrm{sim}}^{yz}\left(\vec{r}\right)\right|^2}{\sum_{V_\mathrm{m}} \left|B_{1,\mathrm{sim}}^{xyz}\left(\vec{r}\right)\right|^2}, \tag{4.47}$$

where we added the additional term $S\left(B_{1,\mathrm{sim}}^{yz}\left(\vec{r}\right)\right)$ to the sum in the numerator.

In our experiments, we observe saturation effects. To quantify this, we analyze spectra similar to Fig. 4.15 for various microwave excitation powers and extract g_{eff} for each of those spectra. In Fig. 4.17, we plot the extracted collective coupling rate g_{eff} as a function of the applied microwave power at the sample input. The SR and MR exhibit similar collective coupling rates, reaching up to 450 kHz at low microwave powers. The unsaturated regime is obtained for microwave powers up to −105 dBm. For applied powers larger than this threshold value, g_{eff} decreases in a non-linear fashion to almost zero. At −40 dBm the signal-to-noise ratio was too small to extract a meaningful coupling rate.

We can describe the data presented in Fig. 4.17 using Eq. (4.10), which describes the collective coupling rate in the presence of an inhomogeneous microwave magnetic field distribution, expressed in the filling factor R_{yz}. We replace R_{yz} by the expression given in Eq. 4.47 and take the microwave power P_S into account by rescaling the magnetic field amplitude according to $B_1 \propto \sqrt{P_\mathrm{S}}$. The resulting expression is fitted to the data with the product $T_1T_2^*$ as the only fit parameter. This allows a

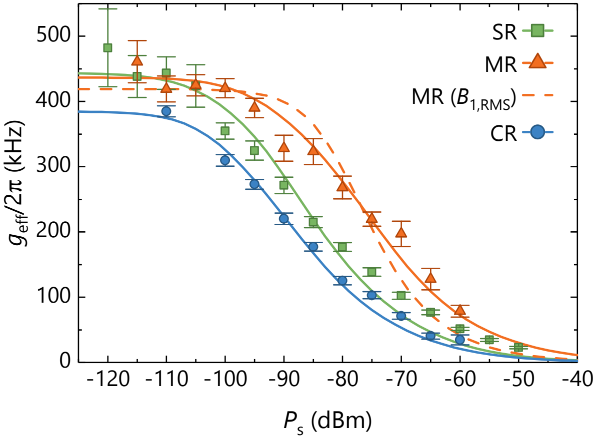

Fig. 4.17 Effective coupling rate g_{eff} as a function of the applied microwave power to the sample P_{S}. The effective coupling rate g_{eff} decreases with increasing microwave power, indicating a power-dependent saturation effect. The solid lines are fits to Eq. (4.47), taking the simulated magnetic field distribution into account. The dashed line is a calculation using the mean field amplitude $B_{1,\text{rms}}$ of the MR.

cross-check with pulsed ESR measurements. The obtained $T_1 T_2^*$ products are displayed in Table 4.3. They vary over one order of magnitude for the three resonator types and exhibit individual fitting uncertainties of up to 72 %, and are therefore inconclusive. Using data from pulsed experiments (see Appendix A3.1) $T_1 = 48\,\mathrm{ms}$ and $T_2^* = 1/\gamma_\mathrm{s} = 272\,\mathrm{ns}$, we expect $T_1 T_2^* \approx 13 \times 10^{-9}\,\mathrm{s}^2$. We attribute the deviation between the calculated and measured $T_1 T_2^*$ product to our assumption of purely Lorentzian line shapes, which is not completely true in our case. To account for a mixture of Lorentzian and Gaussian line shapes, the $T_1 T_2^*$ product in Eq. 4.46 has to be modified to $s T_1 T_2^*$, where s is a correction factor. s can take values $s \ll 1$ [206]. A correction factor in the order of 0.01 can explain the deviation between the $T_1 T_2^*$ products from the saturation experiments and pulsed experiments.

The solid lines in Fig. 4.17 were obtained by incorporating the full 3D microwave magnetic field distribution from our simulations. When we use the root-mean square amplitude $B_{1,\mathrm{rms}}$ of the microwave magnetic field without a spatial dependence in Eq. 4.47, we obtain a significantly worse agreement between the theoretical and experimental data (dashed line). Additionally, the value of $T_1 T_2^* = 6 \times 10^{-14}\,\mathrm{s}^2$ determined from the fitting procedure deviates by several orders of magnitude from the value determined by pulsed ESR. This serves as a further point that the full 3D microwave magnetic field has to be taken into account to obtain meaningful results. Additionally, these results are a further proof of the validity of our simulations and confirms our understanding of the spatial extent of the simulated microwave magnetic field distribution.

4.7 Discussion and conclusion

In this section, we presented the three different resonator geometries studied in this thesis. All three of them offer distinct advantages and disadvantages. Choosing the appropriate resonator geometry therefore depends on the intended application.

Experiments involving planar superconducting resonators and spin ensemble can be grouped by their respective sample mounting method. In our thesis, we use the flip-chip configuration, however, one can also directly structure the resonator onto a crystal containing a spin ensemble. In the following, we present both methods with their advantages and disadvantages and discuss afterwards the implications of each mounting method on the resonator design.

1. *Direct resonator structuring*: In the most direct approach, the superconducting film is deposited directly onto a substrate which already contains a spin ensemble (cf. Ref. [48–50, 67, 114]). As the resonator is structured directly next to the spins to be investigated, this approach promises the largest spin-photon coupling rates. The disadvantage of this approach is that the different thermal expansion coefficients and lattice constants of the substrate and superconducting material can cause strain-induced shifts of the spin resonance frequency [209] or hyperfine interaction [85, 86].
2. *Flip-chip configuration*: In the flip-chip configuration, the spin sample is placed on top of the resonator, while the resonator itself is structured onto a separate substrate (cf. Ref. [51, 52, 54–56, 66, 68] and this work). The advantage of the flip-chip configuration is a greater experimental flexibility, as the resonator fabrication and sample placement is independent. Additionally, this allows to measure samples which are irregularly shaped or too small to directly fabricate a microwave resonator on top. However, due to the flip-chip geometry, a small gap between the microwave resonator and the spin ensemble is highly likely, which is the case in the present work.

We can draw two main conclusions from our simulation and experimental results: First, the SR offers advantages when a homogeneous excitation of the spin ensemble is required, as demonstrated by the simulated field distribution. A homogeneous excitation of the spin ensemble is desired for pulsed ESR experiments in order to control the spin ensemble in a coherent fashion, e.g. for quantum memory applications, where it is important to rotate the complete spin ensemble to a certain point on the Bloch sphere. Although B_1 inhomogeneities can be compensated by adiabatic [135, 136, 210] or optimal control pulses [137, 138, 211], the application of these pulses poses requirements to the resonator bandwidth, which are detrimental to the long storage of quantum information.

A homogeneous field distribution is also favorable for a flip-chip configuration, as the slow microwave magnetic field decay along the z direction offers a spin excitation through the whole sample, even for bulk samples and in the presence of a small gap between the microwave resonator and the spin sample. In order to control this gap size even more precisely, a thin Polyimid (Kapton) spacer can be inserted between the microwave resonator and the sample to avoid the large near-field inhomogeneities in the vicinity of the wires [154]. From the field distribution of the SR we find 20 μm thick region above the resonator, where the achieved field homogeneity is better than 10 %. This value is comparable to commercial microwave resonators.

Second, in order to achieve high single-spin coupling rates, a resonator with a meander geometry should be patterned directly on top of a substrate, containing the spin ensemble in a thin layer near its surface. Due to the localization of the microwave magnetic field near the surface of the resonator, large filling factors can be achieved, as long as the resonator dimensions are small enough. In particular, using the CR design with a large finger capacitor and small inductance results in a high current density and delivers a large B_1 field, increasing the single-spin coupling rate [49]. Additionally, the regular arrangement of the meandering wire can be exploited to emit microwave with a specific wave vector. This technique is widely used in spin wave spectroscopy, where excitation at a non-zero wave vector is required [212].

In conclusion, we have analyzed three geometries for superconducting planar lumped element resonators using FEM simulations and experiments. The FEM simulations allow the extraction of relevant resonator parameters (e.g. resonance frequency and quality factor) and additionally provide the magnetic field distribution of the resonator. Here, the SR offered an increased homogeneity of the microwave magnetic field compared to the other two designs. We analyzed the sensitivity of the microwave resonators to magnetic field and temperature changes. Again, the SR shows a higher robustness compared to the other two designs due to the reduced kinetic inductance participation ratio. In the last section, we performed continuous-wave ESR spectroscopy of a phosphorus spin ensemble in $^{\mathrm{nat}}\mathrm{Si}$. We used the simulated microwave magnetic field distribution in order to calculate the collective coupling rate and found a good agreement between the model and the extracted collective coupling rates from the experiment. In the last part, we measured the power-saturated collective coupling rate and used our model to calculate this saturation behavior as a further proof of the validity of the simulated field distribution.

CHAPTER 5

DYNAMICS OF STRONGLY COUPLED SPIN-PHOTON HYBRID SYSTEMS

In the last part of this thesis, we investigate the dynamics of the coupled spin-photon system. In particular, we are discussing the temporal evolution of the system after being simulated by a standard two-pulse spin echo sequence. This sequence is key to refocus the information contained in the spin ensemble. Understanding the spin echo sequence in the context of strong coupling is therefore a key requirement for the realization of quantum memory applications. Moreover, it is also crucial for the implementation of ultra-sensitive ESR spectroscopy.

This chapter is organized as follows: In Section 5.1 we characterize the sample consisting of a superconducting microwave resonator and a ^{28}Si:P crystal using continuous-wave ESR spectroscopy. We identify two different spin systems and extract their respective collective coupling and relaxation rates. In Section 5.2, we investigate the dynamics of the strongly coupled spin-photon hybrid system and find that a single two-pulse spin echo sequence gives rise to a whole series of echo signals, which we term an *echo train*. In the last part, in

Section 5.3, we employ pulsed ESR spectroscopy to measure the spin life time and spin coherence time of the two spin systems.

The experiments in this chapter are performed using a capacitively-shunted meander resonator (CR), as they promise the largest coupling rates between the spin ensemble and the microwave resonator. We use Sample #2 in this part of the thesis (see Section 3.1 for details). A 20 μm thin slab of [100] oriented ^{28}Si:P is mounted in a flip-chip configuration onto the microwave resonator. The doping concentration is $[P] = 1 \times 10^{17}\,\mathrm{cm}^{-3}$. The ^{28}Si:P piece is held in-place by a $^{\mathrm{nat}}$Si wafer, which is pressed onto the flake and the resonator with a PTFE screw in the lid of the sample box. This sample is then mounted on the mixing chamber stage of a dilution refrigerator and cooled to $T = 50\,\mathrm{mK}$. A static magnetic field B_0 is applied in-plane of the superconducting film. For more details of the cryogenic microwave setup, the reader is referred to Section 3.3.

5.1 Continuous-wave spectroscopy

We begin the experimental part of this chapter with continuous-wave ESR spectroscopy to characterize the phosphorus donor and P_2 dimer spin ensemble. We measure the microwave transmission $|S_{21}|^2$ as a function of the frequency and the applied external field. The microwave power applied to the sample is $P_\mathrm{S} = -122\,\mathrm{dBm} = 0.63\,\mathrm{fW}$. We plot the normalized microwave transmission in Fig. 5.1 (a). A decrease in the transmission is linked to the excitation of a microwave field in the CR, appearing as red color. We observe the bare resonator transmission when the phosphorus hyperfine transition frequencies are far detuned from the resonance frequency. We observe two distinct avoided crossings at $B_0 = 170.1\,\mathrm{mT}$ and $B_0 = 174.3\,\mathrm{mT}$, which can be identified with the resonance field of the hyperfine transitions of phosphorus donors in silicon. The field splitting of 4.2 mT matches the expected hyperfine splitting of phosphorus donors in Si [81].

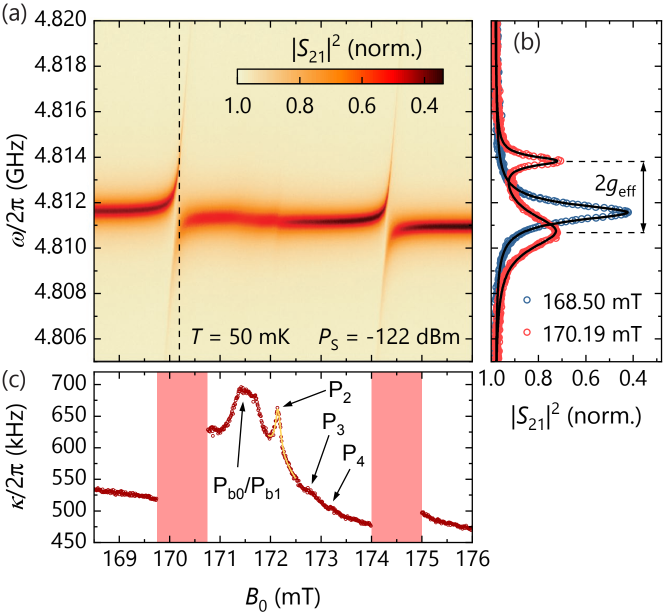

Fig. 5.1 (a) Microwave transmission $|S_{21}|^2$, normalized to unity, as a function of probe frequency and magnetic field. Two avoided crossings are visible, indicating strong coupling between the microwave resonator and the hyperfine transitions of the isolated phosphorus donors. (b) Microwave transmission $|S_{21}|^2$ at fixed magnetic fields of $B_0 = 168.5\,\mathrm{mT}$ and $B_0 = 172.19\,\mathrm{mT}$, corresponding to the bare resonator transmission and the degeneracy point of the strongly coupled low-field hyperfine transition, respectively. (c) The extracted linewidth $\kappa/2\pi$ (HWHM) as a function of the applied magnetic field. Additional spectroscopic feature are visible, including P_{b0}/P_{b1} dangling bond defects and exchange-coupled P_2 dimers (see text for more details).

For a more detailed analysis of the coupling parameters, we plot vertical cuts along the frequency axis at fixed magnetic fields of 168.5 mT and 172.19 mT (dashed line) in Fig. 5.1 (b). For $B_0 = 168.5\,\mathrm{mT}$, we observe the bare resonator. We analyze the resonance dip with the fitting routine describe in Section 3.4.1 (solid line). We find a bare resonance frequency $\omega_\mathrm{r} = 4.8116\,\mathrm{GHz}$ and a linewidth $\kappa_\mathrm{c}/2\pi = (534.85 \pm 2.58)\,\mathrm{kHz}$. This corresponds to a total quality factor $Q = \omega_\mathrm{r}/(2\kappa_\mathrm{c}) \approx 4500$. The coupling rate of the microwave resonator to the feedline is $\kappa_\mathrm{ext} = (304.11 \pm 3.20)\,\mathrm{kHz}$. Similarly, we extract the spin relaxation rate γ_s of the phosphorus donors by a Lorentzian fit along the field axis, far detuned from the resonator. We find a value of $\gamma_\mathrm{s} = (365.11 \pm 70.31)\,\mathrm{kHz}$.

The avoided crossings in the microwave transmission spectrum suggest strong coupling of the spin ensemble and the microwave resonator. In the microwave transmission spectrum for $B_0 = 172.19\,\mathrm{mT}$ (corresponding to the low-field hyperfine transition), we observe a vacuum Rabi splitting, which is a characteristic hallmark of the strong coupling regime [111]. Using a double Lorentzian fit (solid line), we extract a collective coupling rate $g_\mathrm{eff} = (1.54 \pm 0.01)\,\mathrm{MHz}$. This results in a cooperativity $C = g_\mathrm{eff}^2/(\kappa_\mathrm{c}\gamma_\mathrm{s}) = 12.2$, confirming the presence of strong coupling. Note that the vacuum Rabi splitting shown in Fig. 5.1 (b) shows two different linewidths for the two peaks. This phenomenon has been observed before and a possible explanation could be an incoherent coupling of the spin ensemble to a photon bath [139, 213, 214].

To obtain information about further spin species present in the sample we analyze the resonator linewidth $\kappa/2\pi$ as a function of the applied magnetic field. To this end, we extract the linewidth from the frequency-dependent transmission spectrum for each magnetic field step using the fitting routine described in Section 3.4.1. We plot $\kappa/2\pi$ in Fig. 5.1 (c). The shaded area marks the region of strong coupling, where the fitting routine does not return valid results. In the field region between the two avoided crossings we observe further spectroscopic signatures (cf. Section 4.6.1):

1. A broad structure at $B_0 = 171.5\,\mathrm{mT}$, which we attribute to dangling bond defects at the Si/SiO$_2$ interface (Pb$_0$/Pb$_1$ defects [202, 203]).
2. A sharp peak at $B_0 = 172.2\,\mathrm{mT}$, which is compatible to exchange-coupled donor pairs (P$_2$ dimers) [87, 88, 99, 100]. Note that the concentration of the P$_2$ dimers is much smaller than the individual phosphorus donor concentration, i.e. $[\mathrm{P}_2] \ll [\mathrm{P}]$. We also observe weak signals of higher-order clusters consisting of three (P$_3$) and four (P$_4$) phosphorus electron spins, respectively.
3. Underlying both of these features is a broad background signal (broad center line, BCL) due to an interaction between higher-order clusters [98].

We analyze the P$_2$ dimers transition with the methodology presented in Section 4.6.2. The yellow line in Fig. 5.1 (c) is a fit using the Lorentzian part of Eq. 4.30. We obtain a collective coupling rate $g_{\mathrm{eff},\mathrm{P}_2} = (0.35 \pm 0.01)\,\mathrm{MHz}$ and a spin relaxation rate $\gamma_{\mathrm{s},\mathrm{P}_2} = (1.74 \pm 0.09)\,\mathrm{MHz}$. In combination with the bare resonator linewidth, this results in a cooperativity $C_{\mathrm{P}_2} = 0.13$, which puts the P$_2$ dimer ensemble in the weak coupling regime. This is expected due to the $\sqrt{N}$ scaling of g_{eff} and the much lower $[\mathrm{P}_2]$ concentration.

A summary of the extracted coupling parameters is presented in Table 5.1. The two spin ensembles present in our sample allow for a direct comparison of the dynamics of the weak and strong coupling regime under the same experimental conditions, e.g. temperature and microwave noise.

Table 5.1 Coupling parameters of the two spin ensembles present in the sample, namely the low-field hyperfine transition of the individual phosphorus donors as well as the P_2 dimers. The bare resonator linewidth is extracted at $B_0 = 168.5\,\mathrm{mT}$. The cooperativity C indicates strong coupling for the P donors and weak coupling for the P_2 dimers.

Parameter	P donors (LF)	P dimers
$\kappa_c/2\pi$	534.85 ± 2.58 kHz	534.85 ± 2.58 kHz
$\gamma_s/2\pi$	365.11 ± 70.31 kHz	1.74 ± 0.09 MHz
$g_{\mathrm{eff}}/2\pi$	1.54 ± 0.01 MHz	0.35 ± 0.01 MHz
$C = g_{\mathrm{eff}}^2/(\kappa_c\gamma_s)$	12.2	0.13

5.2 Echo trains in a strongly coupled spin ensemble

In this section, we investigate the dynamics of a two-pulse spin echo sequence in the context of a strongly coupled spin ensemble. The results of this section have been submitted for publication in Physical Review Letters. The main results of this section were published in Physical Review Letters [SW2].

5.2.1 Spin echos in a strongly coupled spin ensemble

One of the most basic spin echo pulse sequences is the spin echo [13], as already introduced in Chapter 2. We again describe a spin echo in conventional ESR for reference and then give details about spin echos in the strong coupling regime

A spin echo sequence consists of two microwave pulses, separated by a free evolution period with length τ. Fig. 5.2 schematically shows the pulse sequence, i.e. the microwave signal $|s(t)|$ as a function of time. The diagrams below show the associated spin configurations in the Bloch sphere. At the beginning (panel 1), the magnetization (blue arrow in the Bloch sphere) is in thermal equilibrium and points along the external magnetic field axis, which is along the z axis in this

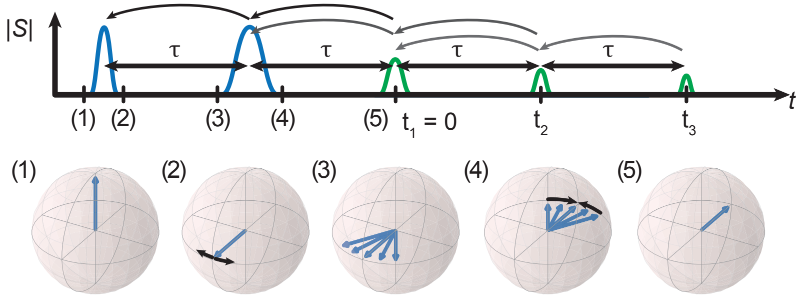

Fig. 5.2 Schematic of the spin echo pulse sequence and the associated states in the Bloch sphere. An initial pulse rotates the magnetization from the equilibrium state (1) into the equatorial plane (2), where the magnetization starts to dephase (3). A second pulse after a time τ refocuses the dephased magnetization (4), such that at a time 2τ a spin echo forms. In the strong coupling regime, additional echos at multiples of τ after the initial spin echo are generated. The arrows indicate the excitation and refocusing "pulses" of subsequent spin echos.

case. The first $\pi/2$ pulse rotates the magnetization into the equatorial $x-y$ plane (panel 2). During the free evolution period with a duration corresponding to the echo spacing τ, the magnetization dephases[1] (panel 3). The second π pulse rotates the magnetization by 180°, which corresponds to a time-reversal operation. This leads to a refocusing of the magnetization such that a spin echo signal is generated at a time 2τ after the initial pulse (panel 5).

In the case of a strongly coupled spin ensemble, the evolution of the hybrid system during the echo interval is more involved. Here, the interaction of the spin ensemble and the microwave resonator has to be taken into account. First, the strong coupling allows for a more sensitive readout of the spin system, as the microwave signal stimulated by the spin echo is efficiently transferred to the microwave circuitry. Second, the transfer of excitations from the spin system into the microwave resonator can be thought of as the generation of

---

[1] This dephasing process can be experimentally measured by recording the microwave signal directly after the microwave pulse, the so-called *free induction decay* (FID).

an additional microwave pulse. This pulse can act on part of the spin system that has been prepared in the $x - y$ plane during the second pulse, leading to an additional echo after time τ after the first conventional echo.

Analogously, the n-th echo is created by the $(n - 1)$-th echo acting as a refocusing pulse for the magnetization that has been prepared in the $x - y$ plane during the $(n - 2)$-th pulse. This is indicated by the black and gray arrows in Fig. 5.2. Note that this mechanism only works if at a time 2τ before the echo spin excitations in the equatorial plane are prepared. In our case, this is due to the non-perfect excitation of the applied microwave pulses caused by the B_1 inhomogeneities. If the second pulse would refocus the spin ensemble without preparing further spins in the equatorial plane, no additional echos would be created.

The mechanism described above has some similarities with a *Carr-Purcell-Meiboom-Gill* (CPMG) pulse sequence [215, 216]. In a CPMG sequence the number of refocusing pulses is increased, which allows simultaneously a reduction of the free evolution period τ. Therefore, the influence of accumulated phase errors between pulses is minimized [13]. A CPMG sequence consists of a $\pi/2$ pulse at the beginning, followed after a delay τ by a train of π pulses, separated by 2τ. In between the π pulses, at time τ, a train of echos with alternating sign is observed. This pulse sequence can be used to measure the spin coherence time in a single experiment, thus improving the signal-to-noise ratio compared to measuring the echo decay using a series of two-pulse experiments [13].

The major difference between a CPMG echo train and the echo train observed in our experiment, is that in our experiments the additional microwave pulses are created by the spin echo itself due to the strong coupling and are situated at different times in the evolution of the sequence. In the CPMG echo train, the echos appear with a time interval of 2τ, interchanging with the applied π pulses. In our experiments,

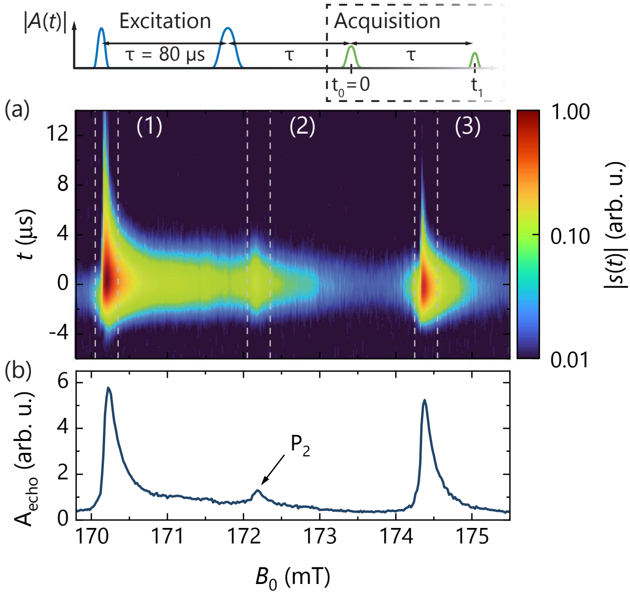

Fig. 5.3 (a) Echo signal as a function of the magnetic field (echo-detected field sweep). We show the time window corresponding to the first observed echo. The dashed regions are shown in more detail in Fig. 5.4. (b) The echo area A_{echo} is obtained by time-integration of the signal presented in panel (a). The two maxima correspond to the strongly coupled phosphorus hyperfine transitions. The small peak in the center corresponds to the hyperfine transition of P_2 dimers.

the echos are separated by τ only, as each echo simultaneously acts as a π pulse in the strong coupling regime. In the weak coupling regime, where $g_{\mathrm{eff}} \ll \kappa_{\mathrm{c}}, \gamma_{\mathrm{s}}$, as in a conventional ESR experiment, the photons created during the spin echo have no time to act back on the spin system but leak out of the resonator.

In a first experiment, we apply a spin echo pulse sequence based on two Gaussian-shaped pulses with pulse lengths of 1 μs and 2 μs, respectively, and an echo spacing of $\tau = 80\,\mu\mathrm{s}$. The resulting spin echo generates a microwave field inside the resonator, which is coupled to the microwave feedline via the coupling rate κ_{ext} and is subsequently detected by the external microwave circuitry (see Sec. 3.2 and 3.3). A schematic of the excitation and acquisition sequence is shown in Fig. 5.3. We sweep the magnetic field and perform this spin echo experiment for each field step, corresponding to an echo-detected magnetic field sweep in conventional ESR. In Fig. 5.3 (a) we show the recorded signal magnitude $|s(t)|$ (see Eq. (3.14)) as a function of the applied magnetic field in the time domain (the two initial microwave pulses were not recorded). The origin of the time axis is set to the peak position of the first echo. Note that the data shown here are single-shot measurements and no signal averaging is performed. The wait time between subsequent measurements is 300 s, which is significantly longer than the spin life time $T_1 = (32.4 \pm 0.8)\,\mathrm{s}$ (see Section 5.3 for details).

In Fig. 5.3 (b), we plot the integrated signal of panel (a), corresponding to the spin echo area A_{echo}. The echo integration is described in more detail in Fig. 3.4.4. We obtain the largest signal magnitude and consequently the largest echo area when the applied magnetic field corresponds to the resonance field of the hyperfine transitions. At $B_0 = 172.2\,\mathrm{mT}$, we observe a small peak corresponding to the P_2 dimer transition. However, we do not recognize a peak corresponding to the $\mathrm{P}_{\mathrm{b0}}/\mathrm{P}_{\mathrm{b1}}$ dangling bond defects. This is attributed to the fact that the spin coherence time of the dangling bond defects ($T_2 = (22.6 \pm 1.6)\,\mu\mathrm{s}$ is small compared to the echo spacing (see Appendix A3.2 for details). This renders the $\mathrm{P}_{\mathrm{b0}}/\mathrm{P}_{\mathrm{b1}}$ invisible. In conclusion, we are able to reproduce the continuous-wave ESR measurement presented in Section 5.1 using an echo-detected field sweep with our home-built pulsed ESR spectrometer.

5.2.2 Multiple echo signatures in the strong coupling regime

In Fig. 5.4 (a) we show extended time traces for the three regions marked by dashed rectangles in Fig. 5.3 (a), corresponding to two hyperfine as well as the P_2 dimer transition. For all three transitions, we detect the first conventional spin echo at $t = 0$. Furthermore, we observe multiple echo signatures (echo trains) in panel (1) and (3), corresponding to the field range of the avoided crossing between the microwave resonator and the hyperfine transitions of the phosphorus donors. The delay between subsequent spin echos matches the echo spacing τ, set by the initial two microwave pulses. In contrast, in panel (2), corresponding to the field range of the P_2 dimer transition, we only record the first conventional spin echo.

Fig. 5.4 (b) shows time traces, recorded at fixed magnetic fields (indicated by arrows in panel (a)) of $B_0 = 172.20\,\mathrm{mT}$ (P_2 dimer transition) and $B_0 = 170.18\,\mathrm{mT}$ (low-field P donor hyperfine transition). The two traces behave qualitatively different in the two coupling regimes. For the weakly coupled P_2 dimers we only observe the first conventional spin echo, while for the strongly coupled phosphorus hyperfine transitions we observe up to 12 echos, separated by the initial inter-pulse delay τ.

The time traces plotted in Fig. 5.4 show a substructure underlying the individual echos. Each echo consists of two echos, attached to one another. The spacing between the two sub-echos increases with time, so that the last echos recorded show a significant dip in the echo signal. The exact origin of this substructure is unclear and would require a quantitative time-domain modeling of the hybrid system.

5.2.3 Origin of the echo train

The measured data shows that echo trains only occur for the two strongly coupled hyperfine lines of the phosphorus donors, but not for the P_2 dimers. The absence of multiple echos for the P_2 dimers cannot be explained with the decoherence properties, as the measured T_2 time of the P_2 dimers is in fact larger than for the hyperfine transition (see Section 5.3). This suggests that a mechanism related to strong coupling is responsible for the generation of the subsequent echos.

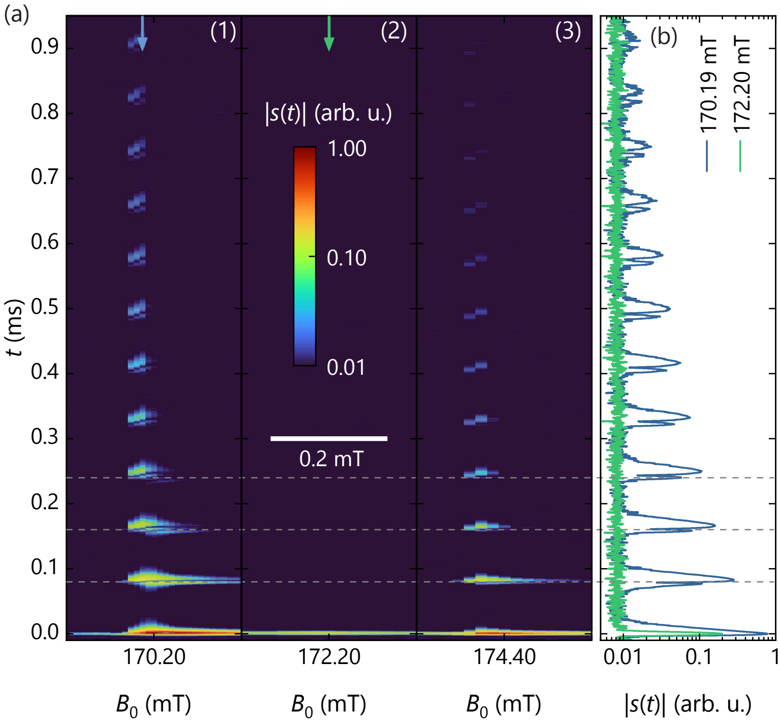

Fig. 5.4 (a) Zoomed time traces of the regions indicated in Fig. 5.3. We observe several spin echo signals in the field regime of the strongly coupled hyperfine lines (panel one and three), while only one echo is recorded for the weakly coupled P_2 dimers (panel two). (b) Time trace at fixed magnetic fields (indicated by arrows in panel (a)) for the low-field hyperfine transition (blue) and P_2 line (green).

While multiple spin echos or echo train have not been observed in ESR before, there are numerous reports of multiple echos in nuclear magnetic resonance (NMR), including experiments on ^{3}He [217–219], ^{3}He/^{4}He mixtures [220–222] as well as water samples [223–225].

In general, the generation of these multiple echos can be traced back to an additional "soft" microwave pulse generated by the magnetization itself. If this pulse is generated during the first echo it acts as a refocusing pulse and leads to the generation of subsequent echos [226]. In the experiments using water samples described above, a large dipolar field is responsible for the additional rotation of the magnetization [227], while in the experiments using ^{3}He and ^{3}He/^{4}He mixtures the Legett-Rice effect in Fermi liquids is responsible [228]. However, in these experiments, an additional magnetic field gradient is applied to the sample, which is required for the generation of multiple echos [224]. In our experiments, we do not apply a field gradient and also assume that a possible gradient due to a sample misalignment is negligible.

Other mechanisms that can generate an additional pulse during an echo is radiation damping, which describes a strong interaction between the radiation between the NMR coil and the sample [229, 230]. In fact, numerical simulations of a two-pulse experiment in an inhomogeneously broadened spin system showed the formation of multiple echos if radiation damping was considered [226].

In our system, the strong coupling between the microwave resonator and the spin ensemble is analogous to radiation damping in NMR, with the difference that the strong coupling in our case is motivated from a quantum mechanical point of view while radiation damping is typically treated classically [231]. Nevertheless, the mechanism in the end is similar: the strong coupling between the microwave resonator and the spin ensemble during a spin echo leads to a back-action of the resonator on the spin system. This additional rotation of the magnetization during a spin echo subsequently leads to further spin echos.

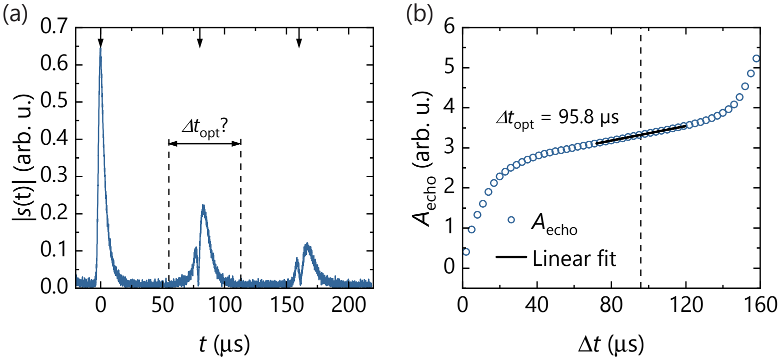

Fig. 5.5 Integration of an multiple echo signal. (a) Exemplary part of a multiple echo signal. The optimal integration window length Δt_{opt} has to be chosen in such a way that the full echo under investigation is integrated without integrating parts of the next echo. (b) Integrated echo area as a function of the integration window length Δt for the echo signal enclosed in dashed lines in panel (a). We find Δt_{opt} from the data and extract the DC voltage offset as the slope of a linear fit (solid line).

5.2.4 Decay of the echo train

In Fig. 5.4, it is apparent that the echo train decays over time, i.e. the echo area of each individual echo decreases. To further investigate this decay, we apply a spin echo pulse sequence with identical pulse lengths, but varying τ at a fixed magnetic field of 170.18 mT. The pause between subsequent measurements was 180 s.

One challenge in evaluating the recorded multiple echo traces is the determination of an optimal time window Δt_{opt} used in the integration of each echo. For short τ, the time window has to be chosen in such a way, that subsequent echos are not included in the integration. Additionally, as we integrate the signal magnitude $|s(t)|$, a finite DC voltage offset V_{dc} is present. When integration over a time window Δt, an additional term $V_{\mathrm{dc}}\Delta t$ will contribute to A_{echo}.

In the following we describe the algorithm we implemented to integrate multiple echo traces. In Fig. 5.5 (a), we plot an excerpt of an exemplary multiple echo trace including the first three recorded echos. We identify the coarse location of each echo (indicated by arrows) using a peak detection algorithm. Next, we integrate the signal using a variable time window Δt, centered around the echo peak under investigation, and plot it in Fig. 5.5 (b).

For small Δt, the echo under investigation is not yet fully included in the integration window and the echo area increases rapidly with increasing time window. For large Δt, the integration window already includes parts of the next (or previous) echo signal and we again observe a rapid increase of the echo area. In the center part, we observe a linear increase of A_{echo} with Δt. Here, the echo under investigation is fully included in the integration window and the linear slope is caused by the additional $V_{\mathrm{dc}}\Delta t$ term due to the voltage offset. The optimal integration time window is then determined as the point where the slope of the curve is minimal. Finally, we fit a linear fit to the region around the optimal integration time window (solid line in Fig. 5.5 (b)) to extract the DC voltage offset from the slope of the curve.

We use this algorithm to extract the echo area for each echo signal. We plot the extracted echo area as a function of the arrival time t_n in Fig. 5.6 (a) in a semi-logarithmic plot. Here, n is the number of the echo. We obtain the characteristic decay time T_{decay} by fitting an an exponential relaxation (solid lines),

$$A_{\mathrm{echo}} = A_0 \cdot \exp\left[-t_n/T_{\mathrm{decay}}\right], \tag{5.1}$$

where A_0 is the echo area of the first conventional spin echo.

With increasing τ, the number of observed echos in an echo train decreases. At the same time, T_{decay} increases with increasing τ. We plot T_{decay} as a function of τ in Fig. 5.6. Here, the trend is more obvious. For $\tau = 40\,\mu\mathrm{s}$ we obtain the shortest decay time of $96\,\mu\mathrm{s}$, which increases by almost an order of magnitude to $T_{\mathrm{decay}} = 0.73\,\mathrm{ms}$ for $\tau = 960\,\mu\mathrm{s}$. We determined the echo train decay up to $\tau = 960\,\mu\mathrm{s}$.

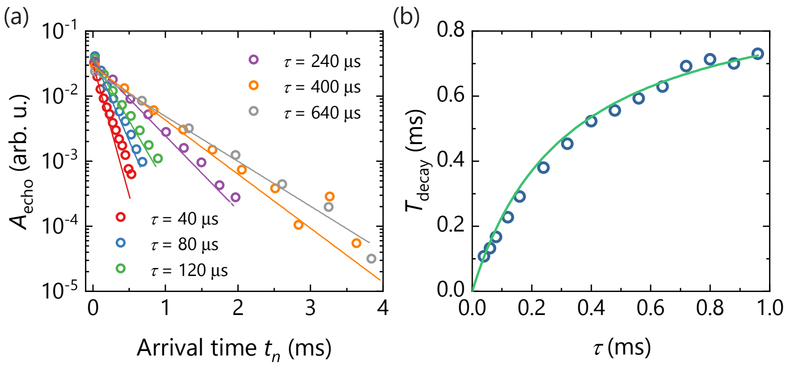

Fig. 5.6 Analysis of the decay of an echo train. (a) Extracted echo areas (data points) of several echo trains for different echo spacing τ. The solid line is an exponential fit (Eq. (5.1)) to extract the decay time. (b) The decay time T_{decay} as a function of the echo spacing τ. For small τ, the decay time is limited by the resonator loss, for long τ the T_2 time is the limiting factor.

For longer τ, the number of recorded echos decreased to two echos, so that no meaningful exponential fit was possible.

The dependence of T_{decay} on τ can be explained by a phenomenological rate equation model. We assume an efficient transfer of excitations between the spin ensemble and the microwave resonator. This assumption is valid, as the measurements are performed in the strong coupling regime and therefore $g_{\text{eff}} \gg \kappa_c, \gamma_s$ and $C \gg 1$.

In the following, we consider two loss mechanisms of the coupled system, which are schematically depicted in Fig. 5.7.

1. Decoherence of the spin ensemble via T_2 processes.
2. Microwave radiation loss due to the coupling of the resonator to the microwave feedline, characterized by κ_{ext}.

First, we neglect radiative losses of the resonator into the feedline. Then the echo area decreases only due to decoherence processes and

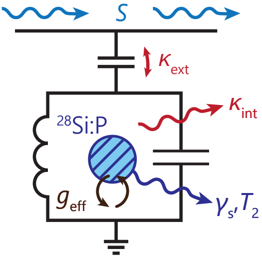

Fig. 5.7 Schematic of the loss mechanisms of the hybrid system with the collective coupling rate g_{eff}. The resonator is coupled to the external microwave circuitry via κ_{ext}. The total loss rate is $\Gamma = \kappa_{\text{c}} + \gamma_{\text{s}} = (\kappa_{\text{ext}} + \kappa_{\text{int}}) + \gamma_{\text{s}}$.

we expect for the n-th echo

$$A_{\text{echo}} \propto \exp\left[-t_n/T_{2,\text{eff}}\right] . \tag{5.2}$$

Here, $T_{2,\text{eff}} = T_2/2$, as we are interested in the decoherence in the time interval τ, whereas T_2 is usually determined as the decay over the time interval 2τ. Note, that for the experiments described here the time scale is T_2 and not T_2^*. This is due to the fact that each echo reverses inhomogeneous effects.

Next, we neglect effects of decoherence and discuss the radiative losses of the photon field inside the microwave resonator during the spin echo. This is characterized by the resonator decay rate κ_{c}. During the echo, the spin system evolves back in the bright state. Due to the coupling to the resonator, a photon fields builds up in the resonator, of which a certain part is coupled to the microwave feedline and is subsequently detected as an echo. Additionally, the spin ensemble dephases again with the dephasing rate γ_{s} and the bright state propagates into a spin dark state. The total decay rate is then given $\Gamma = \kappa_{\text{c}} + \gamma_{\text{s}}$. The ratio $\kappa_{\text{ext}}/\Gamma$ determines the signal coupled out of the resonator. Thus, we can write for the echo area of the n-th echo

$$A_{\text{echo}} \propto \exp\left[-\frac{\kappa_{\text{ext}}}{\kappa_{\text{c}} + \gamma_{\text{s}}} n\right] . \tag{5.3}$$

We rewrite Eq. (5.3) using $t_n = n\tau$ and combine it with Eq. (5.2) using Matthiesen's rule. We obtain an expression for the decay time of the echo train:

$$\frac{1}{T_{\text{decay}}} = \frac{2}{T_2} + \frac{\kappa_{\text{ext}}}{\kappa_{\text{c}} + \gamma_{\text{s}}} \frac{1}{\tau}. \tag{5.4}$$

With this analysis, we can explain the two limiting cases of short and long echo spacing. For $\tau \ll T_2$, decoherence losses are minimized and the decay time is dominated by τ due to the losses via the microwave resonator. Similarly, for $\tau \approx T_2$, the signal lost to the microwave feedline is minimal and the dominating loss source are losses due to T_2 processes. In contrast to experiments in the weak coupling regime, in the strong coupling regime the resonator losses have to be taken into account. This leads to the counter-intuitive result that T_{decay} increases with increasing τ (in contrast to a CPMG sequence).

We fit Eq. (5.2) to the data displayed in Fig. 5.6 (b). We fix κ_{ext}, κ_{c} and γ_{s} to the previously experimentally determined values (see Table 5.1) and vary only T_2. The fit shows a good agreement with the data and we extract $T_2 = (1.9 \pm 0.3)\,\text{ms}$. This value is in the same order of magnitude as $T_{2,\text{conv}} = (2.71 \pm 0.06)\,\text{ms}$, determined by conventional spin echo spectroscopy (see Section 5.3 for details). This fitting method allows to estimate the T_2 time of the spin ensemble using a single measurement of an echo train and previously determined loss parameters of the resonator and spin ensemble. This single-shot approach leads to significantly reduced measurement time.

5.3 Measurement of spin coherence and spin life time

Now that we have established the feasibility of spin echos both in the strong and weak coupling regime, we can use two-pulse and three-pulse sequences to measure both the spin coherence and spin life time of the individual phosphorus donors as well as the P_2 dimers.

5.3.1 Spin coherence time T_2

We first measure the spin coherence time T_2 of the strongly and weakly coupled system using standard spin echo spectroscopy. We apply a series of two-pulse spin echo sequences with pulse durations of 1 µs and 2 µs, respectively, while varying the free evolution period τ. We set the magnetic field to the resonance field of the low-field phosphorus donor hyperfine transition and the P_2 dimer transition and apply the microwave pulses at the resonance frequency. For the strongly coupled phosphorus donors, we apply the microwave pulse at the center frequency of the normal mode splitting.

We extract the echo area for several temperatures and plot A_{echo} as a function of 2τ in Fig. 5.8 (a) and (b) for the individual P donors and P_2 dimers. In this semi-logarithmic plot, the echo area decreases linearly with 2τ. We extract T_2 by fitting an exponential decay function to the data:

$$A_{\mathrm{echo}} = A_0 e^{-2\tau/T_2}, \tag{5.5}$$

where A_0 is the echo amplitude of the first echo. The exponential fits are shown as solid lines in Fig. 5.8 (a) and (b).

We plot the extracted spin coherence time as a function of the sample temperature in Fig. 5.8 (c). At the lowest temperature of $T = 80\,\mathrm{mK}$, we find a T_2 time of $T_{2,P} = (2.71 \pm 0.07)\,\mathrm{ms}$ and $T_{2,P_2} = (10.07 \pm 0.28)\,\mathrm{ms}$ for the individual phosphorus donors and P_2 dimers, respectively. So far, literature values of the spin coherence time of phosphorus donors at millikelvin temperatures are not available. At $T = 1.6\,\mathrm{K}$ and a donor concentration of $[P] = 2 \times 10^{16}\,\mathrm{cm}^{-3}$, a value of approximately 5 ms for individual phosphorus donors was obtained [57]. The spin coherence time of P_2 dimers in an ^{28}Si:P sample with $[P] = 1.6 \times 10^{16}\,\mathrm{cm}^{-3}$, measured at 1.7 K, saturates at 4 ms [99]. The measured spin coherence time of the P donors and P_2 dimers is in the same order of magnitude as the published values, although at a much lower temperature. Additionally, T_2 depends on the donor concentration, as a larger donor concentration

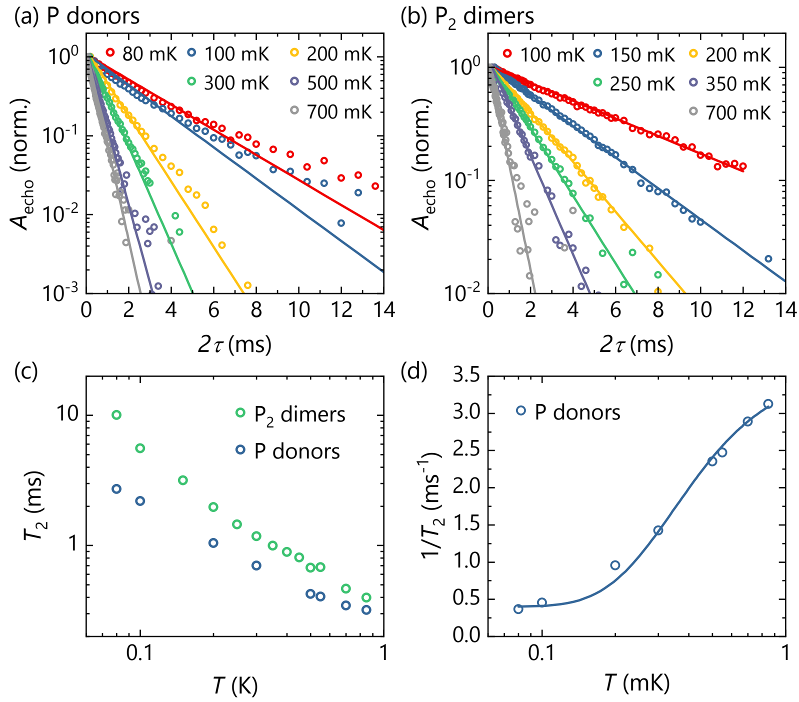

Fig. 5.8 Temperature dependent measurement of the spin coherence time measurements of P donors and P_2 dimers. (a) and (b) show the integrated echo area as a function of 2τ for P donors and P_2 dimers, respectively. The solid lines are fits of Eq. 5.5 to the data. (c) The extracted spin coherence time T_2 for both spin systems as a function of temperature. The T_2 time decreases for both spin systems with increasing temperature. The standard deviation from the fitting procedure is smaller than the symbol size. (d) Inverse T_2 time as a function of temperature. The solid line is a fit to Eq. (5.6). For details, see text.

leads to more dipolar interactions between neighboring spins and thus to a reduction in T_2 [99].

When we increase the sample temperature, the measured T_2 time decreases for both systems. At $T = 850\,\mathrm{mK}$ we extract a T_2 time of 0.32 ms and 0.40 ms for the P donors and P_2 dimers, respectively. From a literature point of view, it is expected that T_2 does not show a temperature dependence below 4 K [57, 99, 232]. For temperatures above 4 K, the dominating relaxation process is the indirect flip-flop mechanism. Here, the dipole-dipole interaction drives spin flip-flops between spin pairs, which are sensed by as random magnetic field fluctuations by neighboring spins. This effectively leads to decoherence [57, 233].

However, in the investigated temperature range, another mechanism has to be responsible for the strong temperature dependence of the T_2 time. We can exclude any effects related to strong coupling, e.g. the cavity protection effect [66, 107, 122], as we observe the temperature dependence also for the weakly coupled P_2 dimers. Takahashi et al. proposed that the temperature dependence of T_2 can be explained by coupling of the electron spin to a fluctuating spin bath [234, 235]. In our case, the phosphorus donors could form such a spin bath. Below a certain temperature threshold, the spin bath is fully polarized and the fluctuations cease, in turn increasing the T_2 time. In Fig. 5.8 (d) we have plotted the inverse T_2 time. The data points can be modeled by the following function [234, 236]:

$$\frac{1}{T_2} = \frac{C}{(1 + e^{T_{\mathrm{Ze}}/T})(1 + e^{-T_{\mathrm{Ze}}/T})} + \Gamma_{\mathrm{res}}, \tag{5.6}$$

where C is a temperature independent parameter, Γ_{res} is a residual relaxation rate and T_{Ze} is the temperature corresponding to the Zeeman energy. We fit Eq. (5.6) to the data (solid line) with a fixed residual relaxation rate $\Gamma_{\mathrm{res}} = 0.4\,\mathrm{ms}^{-1}$. We obtain $T_{\mathrm{Ze}} = (0.705 \pm 0.026)\,\mathrm{K}$, which is approximately three times larger than the expected Zeeman temperature. We attribute this deviation to the limited data in the high-temperature regime for $T > 1\,\mathrm{K}$. While the fitted curve is in good agreement with the data of the P donors, the data for the P_2 dimers cannot be described by this model.

Therefore, further measurements are required to explain the temperature dependence of the T_2 time. One approach, for example, could be to study different decoherence mechanisms by spatially separating the thermal emitter from the spin sample [237]. This could be achieved by inserting a heatable attenuator in the input path, such that the microwave line can be independently heated from the sample. This would allow to check if broadband thermal microwave noise is responsible for the additional decoherence. Additionally, the existing data should be extended to temperatures above 1 K.

5.3.2 Instantaneous diffusion and intrinsic T_2 time

The T_2 time of the individual phosphorus donors at $T = 80\,\mathrm{mK}$ is additionally limited by instantaneous diffusion [99]. This is a process, where flips of nearby spins due to the applied microwave pulse lead to fluctuating magnetic fields at the position of the center spin [238, 239]. As a result, spins with the same resonance frequency before the pulse can have different resonance frequencies afterwards [13]. It is possible to suppress the effects of instantaneous diffusion by applying a spin echo pulse sequence, where the 180° rotation of the second pulse is reduced [232, 240]. This way, the number of spin flips in the vicinity of the central spin are reduced. We perform such an experiment, where we vary the amplitude of the second pulse relative to the first pulse. This effectively reduces the flipping angle of the second pulse.

We plot the extracted inverse T_2 time for both the P donors and the P_2 dimers as a function of the relative amplitude $A_\pi / A_{\pi/2}$ in Fig. 5.9. As can be seen, both datasets show a linear decrease of the inverse T_2 time for smaller rotation angles. The solid lines are linear fits to extrapolate the intrinsic T_2 time of both systems when instantaneous diffusion is completely suppressed. We obtain $T_{2,\mathrm{P,intr.}} = (14.8 \pm 1.0)\,\mathrm{ms}$ and

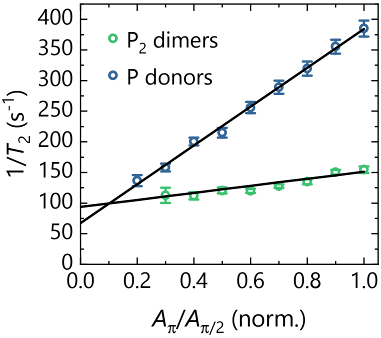

Fig. 5.9 T_2 measurement using a two-pulse spin echo sequence with a variable pulse amplitude A_π of the second pulse. When reducing the flipping angle of the second pulse, instantaneous diffusion is suppressed and the intrinsic T_2 time can be extracted from extrapolating the data to $A_\pi = 0$.

$T_{2,\mathrm{P}_2,\mathrm{intr.}} = (10.67 \pm 0.36)\,\mathrm{ms}$ for the phosphorus donors and P_2 dimers, respectively. From the slope of the linear fit we can see that the phosphorus donors are more affected by instantaneous diffusion than the P_2 dimers. This is attributed to the higher concentration of phosphorus donors than of P_2 dimers, leading to stronger dipole-dipole interactions between neighboring spins, which is a prerequisite for instantaneous diffusion. Consequently, the intrinsic T_2 of the P_2 dimers is comparable to the measured T_2 time above.

5.3.3 Spin lifetime T_1

In the final part, we measure the spin lifetime T_1 using a three-pulse inversion recovery sequence (see Section 2.1.3 for details). We keep the pulse durations $t_\pi = 2t_{\pi/2} = 2\,\mu\mathrm{s}$ as well as the echo spacing $\tau = 80\,\mu\mathrm{s}$ fixed and vary the wait time t_wait between the first and the second pulse.

We apply the inversion recovery sequence with the magnetic field centered on the low-field phosphorus donors hyperfine resonance field as well as the P_2 dimers resonance field. In Fig. 5.10 (a) we plot the

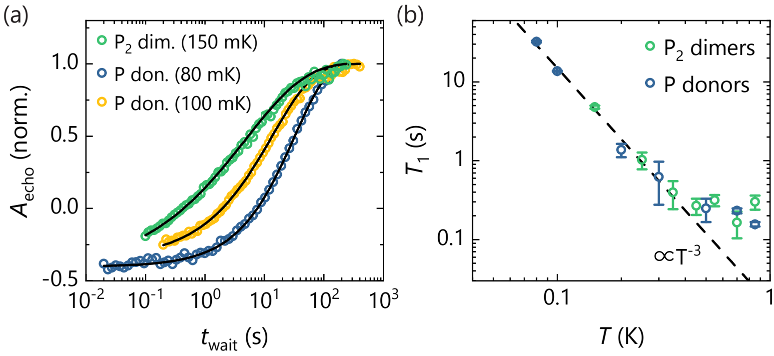

Fig. 5.10 Spin life time measurements of P donors and P_2 dimers. (a) Inversion recovery traces for P donors and P_2 dimers at different temperatures. For small wait times, A_{echo} is negative, indicating an inversed spin ensemble. For long wait times, the spin ensemble is fully relaxed to its equilibrium position. (b) Spin life time T_1 extracted from the data shown in the left panel. T_1 decreases strongly with temperature. The dashed line corresponds to a T^{-3} power law (guide to the eye).

normalized echo area of three measurement series as a function of t_{wait}. For short wait periods, we obtain negative echo areas. Here, the first pulse inverts the spin ensemble and the magnetization points along the $-z$ axis. When increasing t_{wait}, more and more spins relax due to T_1 processes, leading to a reduction of the magnetization. For long wait times, the magnetization can fully recover before the last two pulses are applied and we obtain the full (positive) spin echo response. Note that due to the inhomogeneity of the microwave excitation fields, we do not achieve perfect inversion with the first pulse. This leads to the shown asymmetry of the echo area for short and long wait times.

The recovery of the echo area is described by a stretched exponential,

$$A_{echo} = y_0 + A_0 \left(1 - 2e^{(t_{wait}/T_1)^b}\right), \tag{5.7}$$

where y_0 describes a possible offset of the echo area, A_0 is the amplitude of the recovery and b is the stretch factor. We fit Eq. (5.7) to the data (solid lines) and plot the extracted T_1 times in Fig. 5.10 (b). From the ratio $y_0/(y_0 + A) \approx 0.46$ we estimate that we effectively invert about 46 % of the spin ensemble. The spin life times of the phosphorus donors and the P_2 dimers agree within the error bars, which suggests the same underlying relaxation mechanism for both spin systems. For $T = 80\,\mathrm{mK}$, we obtain $T_{1,\mathrm{P}} = (32.4 \pm 0.8)\,\mathrm{s}$. For temperatures below 500 mK, the temperature dependence can be described by a T^{-3} power law (dashed line), which does not match the predicted $1/T$ behaviour of previous experiments [57, 232]. For temperatures above 500 mK, T_1 remains constant in the measured temperature range up to 850 mK.

A stretched exponential decay is expected when the spin relaxation is subject to a distribution of relaxation rates instead of a single exponential decay [241]. In our case, such a distribution could be caused by the remaining ^{29}Si nuclei. Similar to the spin coherence time, the temperature dependence of the spin life time is unexpected from literature. We again can exclude an origin of the effect related to strong coupling, as both the strongly coupled phosphorus donors as well as the weakly coupled P_2 dimers show a comparable temperature dependence. Additionally, we estimate the Purcell-enhanced relaxation [65, 67]) to be on the order of 50 s, i.e. much longer than the observed relaxation times. Other relaxation mechanisms like direct one-photon process or a two-photon Raman process [81, 82, 91, 232] only apply to temperatures above 2 K and predict a constant T_1 time below 2 K. Therefore, further measurements are required to explain the temperature dependence and microscopic origin of the measured spin life times.

5.4 Discussion and conclusion

In this chapter, we studied the dynamics of a strongly coupled spin-photon hybrid system, consisting of a superconducting microwave resonator and a paramagnetic spin ensemble. We first employed continuous-wave ESR spectroscopy to characterize the hybrid system. The observed avoided crossings at the resonance field of the phosphorus donor hyperfine transition are a clear indicator for strong coupling between the microwave resonator and the individual phosphorus donors. We extracted a coupling rate of $g_{\text{eff}} = (1.54 \pm 0.01)\,\text{MHz}$ and found a cooperativity $C = g_{\text{eff}}^2/(\kappa_{\text{c}}\gamma_{\text{s}}) = 12.2 \gg 1$. Moreover, we identified an additional spin ensemble consisting of exchange-coupled phosphorus dimers (P_2 dimers), which is only weakly coupled to the microwave resonator ($C = 0.13$). This allowed a direct comparison between the strong and weak coupling regime under the same experimental conditions.

In the main part of this chapter, we studied the dynamics of two-pulse spin echo sequences in both of the spin systems. First, we conducted a echo-detected magnetic field sweep by applying a spin echo sequence based on two Gaussian-shaped pulses at each magnetic field step. We obtain an ESR spectrum by integrating the echo response and find a good agreement between the echo-detected and the continuous-wave spectrum, demonstrating the feasibility of spin echos in the strong coupling regime.

Furthermore, when prolonging the acquisition time window, we observe additional echo signatures (echo trains) when the magnetic field is set to the resonance field of the strongly coupled hyperfine transitions. The delay between subsequent spin echos matches the free evolution period τ. In contrast, when the magnetic field is set to the resonance field of the weakly coupled P_2 dimers, we only observe the first conventional spin echo. We attribute the occurrence of these echo signatures to the strong coupling between the microwave resonator and the spin ensemble: During the spin echo, photons are created in the microwave resonator, which can again act on the spin ensemble due to the strong coupling. We analyzed the decay of the echo train and found a decay time that depends on the echo spacing τ. We quantitatively understand this behavior in terms of a rate equation model by taking the coherence and dephasing rates of the spin ensemble as well as the microwave resonator into account.

Finally, we investigated the spin coherence time T_2 and spin lifetime T_1 of both the phosphorus donors as well as the P_2 dimers. The T_2 time of the phosphorus donors is dominated by instantaneous diffusion. By adjusting the pulse sequence so that instantaneous diffusion is suppressed, we obtain an intrinsic T_2 time of the phosphorus donors of $T_2 = (14.8 \pm 1.0)\,\mathrm{ms}$ at $T = 80\,\mathrm{mK}$, while the T_2 of the phosphorus dimers is determined to $(10.67 \pm 0.36)\,\mathrm{ms}$. We reproduced the previously measured temperature dependence of both the coherence time as well as the spin life time of the phosphorus donors [56]. In this unexpected behavior, T_1 as well as T_2 increases with decreasing temperature, whereas from literature a constant behavior is expected. We have observed a similar behavior of T_1 and T_2 for the P_2 dimer spin ensemble, which rules out any effect related to collective coupling (e.g. Purcell relaxation, cavity protection effect). The exact origin of this behavior is still unclear and has to be investigated in future experiments. One approach to discern different decoherence mechanisms could be to spatially separate heating of the sample and heating of the microwave input line.

In conclusion, we have demonstrated the feasibility of spin echo experiments in the strong coupling regime. This allows to implement more complex pulsed ESR sequences, which use spin echos as a readout method. However, the dynamics of the coupled system, in particular the generation of an echo train, has to be taken into account. In order to quantitatively understand the dynamics of the echo traces, numerical modeling of the equations of motion describing the temporal evolution is required.

CHAPTER 6

SUMMARY AND OUTLOOK

In this thesis, we investigated the dynamics of a strongly-coupled spin-photon hybrid system consisting of a spin ensemble of phosphorus donors in ^{28}Si and a superconducting microwave resonator. In particular, we investigated the dynamics of the strongly coupled system after applying the well known two-pulse spin echo sequence from conventional ESR spectroscopy. In order to qualitatively understand the spin-photon coupling, we analyzed three different resonator structures in regarding to their field homogeneity, temperature- and magnetic field robustness as well as their suitability for reaching the strong coupling regime.

In Chapter 3 we presented the technical implementation of our magnetic resonance experiments. In the course of this thesis, we developed and built a pulsed ESR spectrometer based on an arbitrary waveform generator and a fast digitizer. This setup enables the generation and phase-sensitive detection of arbitrarily shaped microwave pulses and pulse sequences. The experiments were conducted in two cryogenic environments, optimized to reduce the noise impinging on the sample.

In the first main part of the thesis (Chapter 4), we analyzed three different geometries for superconducting microwave resonators. To this end, we employed finite element simulations to calculate the three-dimensional microwave magnetic field distribution. We compared the three resonator geometries in regard to the homogeneity of the generated magnetic field, the robustness to temperature- and magnetic field changes as well as a quantitative comparison of the expected spin-photon coupling rates. We demonstrated that the spiral resonator (SR) offers an improved field homogeneity and robustness compared to the other two designs due to the novel arrangement of the superconducting wire. Our analysis shows that the capacitively-shunted resonator (CR) promises the largest coupling rates due to the minimization of the inductance of the resonator. In order to quantitatively calculate the spin-photon coupling rate, we extended a previous model to take into account the field inhomogeneity of the microwave resonators. We calculated the power-dependent coupling rate and found a good agreement between the model and experimental data, corroborating the validity of our model approach.

The second main aspect of this thesis (Chapter 5), are experiments to investigate the spin dynamics of spin-photon hybrid systems in the strong coupling regime. First, we established the presence of two different but highly comparable spin systems in the phosphorus-doped ^{28}Si crystal, individual P donors and clusters consisting of phosphorus donor pairs. The individual phosphorus donors were strongly coupled to the microwave resonator with a cooperativity $C \approx 12$, giving rise to an avoided crossing at the resonance field of the two hyperfine transitions. In contrast, the exchange-coupled P_2 dimers were only weakly coupled to the microwave resonator with $C = 0.13$. This allowed for a comparison of the dynamics of the strong and weak coupling regime under the same experimental conditions.

We then continued with pulsed ESR spectroscopy, applied to both of the spin systems. We could reproduce the continuous-wave ESR spectrum using a echo-detected magnetic field sweep, demonstrating the feasibility of spin echos in the strong coupling regime. Further analysis of the time trace showed a whole series of spin echo signatures, spaced apart by the echo delay τ. These echo trains occurred only when the magnetic field was set to the resonance field of the strongly coupled hyperfine transitions. For the weakly coupled P_2 dimers, we only observed the first conventional spin echo. We attributed the occurrence of these echo trains to the strong coupling between the spin ensemble and the microwave resonator. During the spin echo, photons are created in the resonator, which can act itself on the magnetization, thereby giving rise to further echos. We analyzed the decay of the echo train and found a dependence on the echo spacing τ. We quantitatively understand this dependence in terms of a simple rate equation model, taking into account the coherence and dephasing rates of both the spin ensemble and the microwave resonator. Finally, we investigated the spin life time and spin coherence time of both the phosphorus donors as well as the P_2 dimers. We observed a temperature dependence of the T_1 and T_2 time for both spin systems, which is not expected from literature. However, a more thorough analysis is required to reveal the microscopic origin of this temperature dependence.

The insights of the demonstrated experiments deepen the understanding of the dynamics of strongly coupled spin-photon hybrid systems and are a further step towards quantum memory applications, generation of non-classical spin states like squeezed spin states [242–244] or the implementation of discrete time crystals [245, 246] using spin ensembles.

However, all of these experiments mentioned in the last paragraph require coherent control over the complete spin ensemble. In our experiments, the B_1 inhomogeneity of the microwave resonators prevented such a coherent control, even with the improved field homogeneity of the SR. In order to compensate the B_1 inhomogeneities, we suggest to implement adiabatic [135, 136, 210] or optimal control pulses [137, 138, 211]. Adiabatic and optimal control pulses are a amplitude- and frequency modulated microwave pulses, which are insensitive to B_1

inhomogeneities. As our experimental setup allows the generation of arbitrarily shaped microwave pulses, these pulse sequences can be readily implemented.

In regard to the dynamics of strongly-coupled spin-photon hybrid systems, we suggest to develop a theoretical model based on solving the coupled equations of motion [64] in order to describe the full coupled dynamics of the hybrid system. This allows, for example, to simulate the time traces of the multiple echo signatures to obtain further insight into the microscopic mechanism involved in the echo creation. Additional phase cycling experiments, where the phase relation of the individual echos is investigated, might give additional insight. Furthermore, we suggest additional measurements to resolve the microscopic origin of the temperature dependence of the spin coherence and spin lifetime. One approach could be, for example, to separate contributions from thermal noise and microwave noise by including a heatable attenuator in the input path of the experimental setup. This would allow to keep the spin ensemble at base temperature, while generating microwave noise via heating.

APPENDIX

A1 Sample Overview

We give an overview of the three samples used in this thesis in Table A1.1. Details about the sample preparation are given in Section 3.1

Table A1.1 Summary of the samples used in this thesis.

Sample	Description
#1	Fabricated by Petio Natzkin [124] **Material:** 150 nm Nb/10 nm Al on ^{nat}Si substrate **Substrate dimensions:** $6 \times 10 \times 0.525\,\mathrm{mm}^3$ **Layout:** 14 resonators (6 CR, 4 MR, 4 SR) **Spin ensemble:** ^{nat}Si:P, $[P] = 2 \times 10^{17}\,\mathrm{cm}^{-3}$ (20 µm thick flakes)
#2	Fabricated by Christoph Zollitsch [139] **Material:** 150 nm Nb on ^{nat}Si substrate **Substrate dimensions:** $6 \times 10 \times 0.525\,\mathrm{mm}^3$ **Layout:** 5 resonators (5 CR) **Spin ensemble:** ^{28}Si:P, $[P] = 1 \times 10^{17}\,\mathrm{cm}^{-3}$ (20 µm thick flakes)
#3	Fabricated by Andreas Faltermeier and Stefan Weichselbaumer **Material:** 150 nm Nb on ^{nat}Si substrate **Substrate dimensions:** $6 \times 10 \times 0.525\,\mathrm{mm}^3$ **Layout:** 5 resonators (5 CR, nominally identical to Sample #2) **Spin ensemble:** ^{28}Si:P, $[P] = 1 \times 10^{17}\,\mathrm{cm}^{-3}$ (20 µm thick flakes)

A2 Derivations

A2.1 Change of resonance frequency with kinetic inductance

In the following, we derive the expression for the relative frequency change of a microwave resonator when the kinetic inductance changes. We assume that the change of the kinetic inductance, ΔL_k, is small compared to the total inductance:

$$\Delta L_\mathrm{k} \ll L_\mathrm{k} + L_\mathrm{m}, \tag{A2.1}$$

where L_k and L_m are the kinetic and magnetic inductance, respectively. The resonance frequency is given by

$$\omega_\mathrm{r}(L_\mathrm{k}) = \frac{1}{\sqrt{LC}} = \frac{1}{\sqrt{C\,(L_\mathrm{k} + L_\mathrm{m})}}. \tag{A2.2}$$

For a small change of the kinetic inductance, we can express Eq. (A2.2) using a Taylor expansion:

$$\begin{aligned} \omega_\mathrm{r}(L_\mathrm{k} + \Delta L_\mathrm{k}) &= \omega_\mathrm{r}(L_\mathrm{k}) + \frac{\mathrm{d}}{\mathrm{d}L_\mathrm{k}}\omega_\mathrm{r}(L_\mathrm{k}) \cdot \Delta L_\mathrm{k} \\ &= \omega_\mathrm{r}(L_\mathrm{k}) - \frac{1}{2} C \omega_\mathrm{r}(L_\mathrm{k})^3 \Delta L_\mathrm{k} \end{aligned} \tag{A2.3}$$

With this, we can now give an expression for the relative change of the resonance frequency:

$$\begin{aligned} \frac{\omega_\mathrm{r}(L_\mathrm{k} + \Delta L_\mathrm{k})}{\omega_\mathrm{r}(L_\mathrm{k})} &= 1 - \frac{1}{2} C \omega_\mathrm{r}(L_\mathrm{k})^2 \Delta L_\mathrm{k} \\ &= 1 - \frac{1}{2} C \left(\frac{1}{\sqrt{C(L_\mathrm{m} + L_\mathrm{k})}} \right)^2 \Delta L_\mathrm{k} \\ &= 1 - \frac{1}{2} \frac{\Delta L_\mathrm{k}}{L_\mathrm{m} + L_\mathrm{k}}. \end{aligned} \tag{A2.4}$$

The change of the kinetic inductance is given by $\Delta L_\mathrm{k} = L_\mathrm{k}(x=0) - L_\mathrm{k}(x)$, where x is a placeholder for either temperature or magnetic field. With this, we obtain:

$$\begin{aligned}\frac{\omega_\mathrm{r}(L_\mathrm{k}+\Delta L_\mathrm{k})}{\omega_\mathrm{r}(L_\mathrm{k})} &= 1 - \frac{1}{2}\frac{L_\mathrm{k}(x=0) - L_\mathrm{k}(x)}{L_\mathrm{m} + L_\mathrm{k}(x=0)} \\ &= 1 - \frac{1}{2}\frac{L_\mathrm{k}(x=0)}{L_\mathrm{m} + L_\mathrm{k}(x=0)}\left(1 - \frac{L_\mathrm{k}(x)}{L_\mathrm{k}(0)}\right) \\ &= 1 - \frac{1}{2}\alpha\left(1 - \frac{L_\mathrm{k}(x)}{L_\mathrm{k}(0)}\right), \end{aligned} \tag{A2.5}$$

with the kinetic inductance participation ratio $\alpha = \frac{L_\mathrm{k}(0)}{L_\mathrm{k}(0)+L_\mathrm{m}}$.

A2.2 Collective coupling rate in an inhomogeneous B_1 field

In this section, we provide an alternative derivation of Eq. (4.10), based on the average photon density in a volume element ΔV. As before, the collective coupling strength in a homogeneous magnetic field is given by

$$g_\mathrm{eff,hom} = \frac{g_\mathrm{e}\mu_\mathrm{B}}{2\hbar}\sqrt{\frac{1}{2}\mu_0 \rho_\mathrm{eff}\hbar\omega_\mathrm{r}\nu}. \tag{A2.6}$$

In our simulations, we calculate the 3D microwave magnetic field distribution and export it as discrete volume elements, arranged on a regular grid. The elements have a finite volume $\Delta V = \Delta x \Delta y \Delta z$, where Δi is the extent in the corresponding spatial dimension. We choose $\Delta i = 1\,\mu$m for the CR and MR and $\Delta i = 1.5\,\mu$m for the SR due to the larger mode volume.

Assuming that the volume element is small enough that the magnetic field over the volume element is homogeneous, we use Eq. (A2.6) to find for the collective coupling strength of a single volume element

$$\tilde{g}_\mathrm{eff}(\vec{r}) = \frac{g_\mathrm{e}\mu_\mathrm{B}}{2\hbar}\left(\alpha B_{1,\mathrm{sim}}^{yz}(\vec{r})\right)\sqrt{\rho_\mathrm{eff}\Delta V}. \tag{A2.7}$$

Here, $B_{1,\mathrm{sim}}^{yz}$ is the exported average field amplitude of the volume element and $\rho_{\mathrm{eff}}\Delta V$ is the number of spins in the volume element. The calibration factor α rescales the microwave magnetic field amplitude from the simulated excitation power to the power level of vacuum fluctuations. It can be calculated by equating the vacuum energy with the integrated energy density of the magnetic field: [33]

$$\frac{\hbar\omega_{\mathrm{r}}}{4} = \frac{1}{2\mu_0}\int_{\mathrm{V_m}} \left(\alpha B_{1,\mathrm{sim}}^{xyz}\right)^2 \, \mathrm{d}V. \tag{A2.8}$$

Note that we also take into account the x component of the magnetic field in order to obtain a valid normalization. Solving Eq. (A2.8) we obtain

$$\alpha = \sqrt{\frac{\mu_0\hbar\omega_{\mathrm{r}}}{2\Delta V \sum_{V_{\mathrm{m}}} \left(B_{1,\mathrm{sim}}^{xyz}\right)^2}}. \tag{A2.9}$$

The collective coupling strength g_{eff} can then be calculated by combining Eq. (A2.6) and (A2.9) and summing over all volume elements in the sample volume:

$$g_{\mathrm{eff}} = \sqrt{\sum_{\Delta V} \left|\tilde{g}_{\mathrm{eff}}\right|^2} = \tag{A2.10}$$

$$= \frac{g_{\mathrm{e}}\mu_{\mathrm{B}}}{2\hbar}\sqrt{\frac{\mu_0\hbar\omega_{\mathrm{r}}\rho_{\mathrm{eff}}}{2}\,\frac{\sum_V \left|B_{1,\mathrm{sim}}^{yz}(\vec{r})\right|^2}{\sum_{V_{\mathrm{m}}} \left|B_{1,\mathrm{sim}}^{xyz}(\vec{r})\right|^2}}. \tag{A2.11}$$

A3 Additional pulsed ESR measurements

In this section, we present additional pulsed ESR measurements, which were not included in the main text.

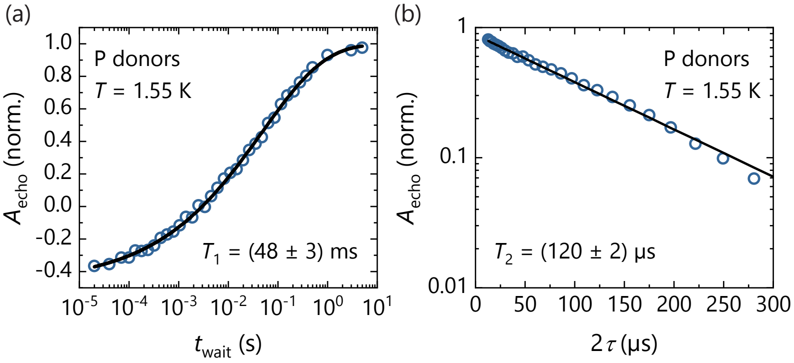

Fig. A3.1 Pulsed measurements of a ${}^{\mathrm{nat}}$Si:P sample at $T = 1.55\,\mathrm{K}$. (a) Integrated echo area as a function of the wait time in an inversion recovery sequence. The solid line is a fit of Eq. (5.7) to the data in order to extract the spin relaxation time $T_1 = (48 \pm 3)\,\mathrm{ms}$. (b) Integrated echo area as a function of 2τ in a two-pulse spin echo sequence. The solid line is a fit of an exponential decay given in Eq. (5.5) to extract $T_2 = (120 \pm 2)\,\mu\mathrm{s}$.

A3.1 Spin relaxation and spin coherence time of ${}^{\mathrm{nat}}$Si:P

We present pulsed ESR measurements of a ${}^{\mathrm{nat}}$Si:P sample at $T = 1.55\,\mathrm{K}$ in Fig. A3.1. In order to determine the spin relaxation time T_1 we perform inversion recovery spectroscopy. Panel a shows the integrated echo area as a function of the wait time of the inversion recovery sequence. Fitting Eq. (5.7) allows to extract a spin relaxation time $T_1 = (48 \pm 3)\,\mathrm{ms}$.

The spin coherence time is measured using a two-pulse spin echo sequence, where the free evolution period τ is varied. In Fig. A3.1 (b), we plot the integrated echo area as a function of 2τ. The solid line is a fit to Eq. (5.5), describing a standard exponential decay. We obtain $T_2 = (120 \pm 2)\,\mu\mathrm{s}$. Note that the measured spin coherence time is significantly shorter than the value determined in Section 5.3. This is due to the presence of naturally abundant ^{29}Si nuclei in the natural Si substrate.

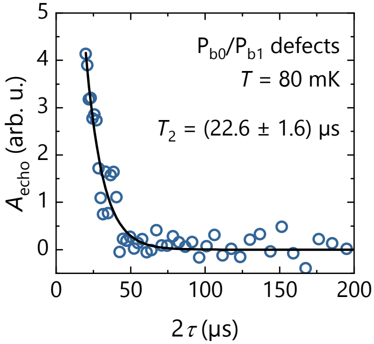

Fig. A3.2 Pulsed measurements of a ^{28}Si:P sample at $T = 80\,\mathrm{mK}$ with the magnetic field set to the resonance field of the P_{b0}/P_{b1} defects. The graph shows the integrated echo area as a function of 2τ in a two-pulse spin echo sequence. The solid line is a fit of an exponential decay given in Eq. (5.5) to extract $T_2 = (22.6 \pm 1.6)\,\mu\mathrm{s}$.

A3.2 Spin coherence time of $\mathrm{P_{b0}/P_{b1}}$ defects

In Fig. A3.2, we show a measurement of the spin coherence time T_2 of $\mathrm{P_{b0}/P_{b1}}$ defects at the $\mathrm{Si/SiO_2}$ interface [202, 203] at $T = 80\,\mathrm{mK}$. We measure T_2 using a two-pulse spin echo sequence, where the free evolution time τ is varied. We extract $T_2 = (22.6 \pm 1.6)\,\mu\mathrm{s}$. This value is considerably shorter than the length of the pulse sequence in the echo detected field sweep presented in Section 5.2, rendering the $\mathrm{P_{b0}/P_{b1}}$ peak invisible.

BIBLIOGRAPHY

List of author's publications

[SW1] S. Weichselbaumer, P. Natzkin, C. W. Zollitsch, M. Weiler, R. Gross, and H. Huebl. *Quantitative Modeling of Superconducting Planar Resonators for Electron Spin Resonance*. Physical Review Applied **12**, 024021 (2019).

[SW2] S. Weichselbaumer, M. Zens, C. W. Zollitsch, M. S. Brandt, S. Rotter, R. Gross, and H. Huebl. *Echo Trains in Pulsed Electron Spin Resonance of a Strongly Coupled Spin Ensemble*. Physical Review Letters **125**, 137701 (2020).

References to scientific publications

[1] I. I. Rabi, J. R. Zacharias, S. Millman, and P. Kusch. *A New Method of Measuring Nuclear Magnetic Moment*. Physical Review **53**, 318 (1938).

[2] E. K. Zavoisky. *Spin-Magnetic Resonance in Paramagnetics*. J. Phys. (USSR) **9**, 245 (1945).

[3] E. K. Zavoisky. *Paramagnetic Relaxation of Liquid Solutions for Perpendicular Fields*. J. Phys. (USSR) **9**, 211 (1945).

[4] F. Bloch. *Nuclear Induction*. Physical Review **70**, 460 (1946).

[5] E. M. Purcell, H. C. Torrey, and R. V. Pound. *Resonance Absorption by Nuclear Magnetic Moments in a Solid*. Physical Review **69**, 37 (1946).

[6] P. G. Baranov, H. J. von Bardeleben, F. Jelezko, and J. Wrachtrup. *Magnetic Resonance of Semiconductors and Their Nanostructures*. Springer Series in Materials Science (Springer Vienna, Vienna, 2017, ISBN: 978-3-7091-1156-7).

[7] S. Van Doorslaer and D. M. Murphy. *EPR Spectroscopy in Catalysis*. en. In: *EPR Spectroscopy: Applications in Chemistry and Biology*. Ed. by M. Drescher and G. Jeschke. Topics in Current Chemistry. Berlin, Heidelberg: Springer, 2012, 1 ISBN: 978-3-642-28347-5.

[8] M. A. Hemminga and L. J. Berliner. *ESR Spectroscopy in Membrane Biophysics*. Biological Magnetic Resonance v. 27 (Springer, New York, 2007, ISBN: 978-0-387-25066-3).

[9] M. Drescher. *EPR in Protein Science*. en. In: *EPR Spectroscopy: Applications in Chemistry and Biology*. Ed. by M. Drescher and G. Jeschke. Topics in Current Chemistry. Berlin, Heidelberg: Springer, 2012, 91 ISBN: 978-3-642-28347-5.

[10] E. Bordignon. *Site-Directed Spin Labeling of Membrane Proteins*. en. In: *EPR Spectroscopy: Applications in Chemistry and Biology*. Ed. by M. Drescher and G. Jeschke. Topics in Current Chemistry. Berlin, Heidelberg: Springer, 2012, 121 ISBN: 978-3-642-28347-5.

[11] A. Abragam and B. Bleaney. *Electron Paramagnetic Resonance of Transition Ions* (Oxford University Press, Oxford, 2012, ISBN: 978-0-19-102300-2).

[12] C. P. Poole. *Electron Spin Resonance: A Comprehensive Treatise on Experimental Techniques* (Dover Publications, Mineola, N.Y, 1996, ISBN: 978-0-486-69444-3).

[13] A. Schweiger and G. Jeschke. *Principles of Pulse Electron Paramagnetic Resonance* (Oxford University Press, Oxford, UK, 2001, ISBN: 978-0-19-850634-8).

[14] G. R. Eaton, S. S. Eaton, D. P. Barr, and R. T. Weber. *Quantitative EPR* (Springer-Verlag, Wien, 2010, ISBN: 978-3-211-92947-6).

[15] E. L. Hahn. *Nuclear Induction Due to Free Larmor Precession*. Physical Review **77**, 297 (1950).

[16] E. L. Hahn. *Spin Echoes*. Physical Review **80**, 580 (1950).

[17] R. J. Blume. *Electron Spin Relaxation Times in Sodium-Ammonia Solutions*. Physical Review **109**, 1867 (1958).

[18] L. G. Rowan, E. L. Hahn, and W. B. Mims. *Electron-Spin-Echo Envelope Modulation*. Physical Review **137**, A61 (1965).

[19] W. B. Mims. *Envelope Modulation in Spin-Echo Experiments*. Physical Review B **5**, 2409 (1972).

[20] G. Feher. *Observation of Nuclear Magnetic Resonances via the Electron Spin Resonance Line*. Physical Review **103**, 834 (1956).

[21] W. B. Mims. *Pulsed Endor Experiments*. Proceedings of the Royal Society A: Mathematical, Physical and Engineering Sciences **283**, 452 (1965).

[22] E. R. Davies. *A New Pulse Endor Technique*. Physics Letters A **47**, 1 (1974).

[23] C. Gemperle, G. Aebli, A. Schweiger, and R. Ernst. *Phase Cycling in Pulse EPR*. Journal of Magnetic Resonance **88**, 241 (1990).

[24] A. L. Barra, L. C. Brunel, and J. B. Robert. *EPR Spectroscopy at Very High Field*. Chemical Physics Letters **165**, 107 (1990).

[25] T. F. Prisner, M. Rohrer, and K. Möbius. *Pulsed 95 GHz High-Field EPR Heterodyne Spectrometer with High Spectral and Time Resolution*. Applied Magnetic Resonance **7**, 167 (1994).

[26] K. Möbius and A. Savitsky. *High-Field EPR Spectroscopy on Proteins and Their Model Systems - Characterization of Transient Paramagnetic States* (The Royal Society of Chemistry, 2008, ISBN: 978-0-85404-368-2).

[27] S. Geschwind, R. J. Collins, and A. L. Schawlow. *Optical Detection of Paramagnetic Resonance in an Excited State of* Cr^{3+} *in* Al_2O_3. Physical Review Letters **3**, 545 (1959).

[28] C. Boehme and K. Lips. *Theory of Time-Domain Measurement of Spin-Dependent Recombination with Pulsed Electrically Detected Magnetic Resonance*. Physical Review B **68**, 245105 (2003).

[29] J. Köhler, J. a. J. M. Disselhorst, M. C. J. M. Donckers, E. J. J. Groenen, J. Schmidt, and W. E. Moerner. *Magnetic Resonance of a Single Molecular Spin*. Nature **363**, 242 (1993).

[30] J. Wrachtrup, C. von Borczyskowski, J. Bernard, M. Orrit, and R. Brown. *Optical Detection of Magnetic Resonance in a Single Molecule*. Nature **363**, 244 (1993).

[31] A. Morello, J. J. Pla, F. A. Zwanenburg, K. W. Chan, K. Y. Tan, H. Huebl, M. Möttönen, C. D. Nugroho, C. Yang, J. A. van Donkelaar, A. D. C. Alves, D. N. Jamieson, C. C. Escott, L. C. L. Hollenberg, R. G. Clark, and A. S. Dzurak. *Single-Shot Readout of an Electron Spin in Silicon*. Nature **467**, 687 (2010).

[32] B. E. Kane. *A Silicon-Based Nuclear Spin Quantum Computer*. Nature **393**, 133 (1998).

[33] R. J. Schoelkopf and S. M. Girvin. *Wiring up Quantum Systems*. Nature **451**, 664 (2008).

[34] R. Schirhagl, K. Chang, M. Loretz, and C. L. Degen. *Nitrogen-Vacancy Centers in Diamond: Nanoscale Sensors for Physics and Biology*. Annual Review of Physical Chemistry **65**, 83 (2014).

[35] Y. Nakamura, Y. A. Pashkin, and J. S. Tsai. *Coherent Control of Macroscopic Quantum States in a Single-Cooper-Pair Box*. Nature **398**, 786 (1999).

[36] M. H. Devoret and J. M. Martinis. *Implementing Qubits with Superconducting Integrated Circuits*. Quantum Information Processing **3**, 163 (2004).

[37] M. Steffen, M. Ansmann, R. C. Bialczak, N. Katz, E. Lucero, R. McDermott, M. Neeley, E. M. Weig, A. N. Cleland, and J. M. Martinis. *Measurement of the Entanglement of Two Superconducting Qubits via State Tomography*. Science **313**, 1423 (2006).

[38] M. Göppl, A. Fragner, M. Baur, R. Bianchetti, S. Filipp, J. M. Fink, P. J. Leek, G. Puebla, L. Steffen, and A. Wallraff. *Coplanar Waveguide Resonators for Circuit Quantum Electrodynamics*. Journal of Applied Physics **104**, 113904 (2008).

[39] T. Lindström, J. E. Healey, M. S. Colclough, C. M. Muirhead, and A. Y. Tzalenchuk. *Properties of Superconducting Planar Resonators at Millikelvin Temperatures*. Physical Review B **80**, 132501 (2009).

[40] A. Blais, R.-S. Huang, A. Wallraff, S. M. Girvin, and R. J. Schoelkopf. *Cavity Quantum Electrodynamics for Superconducting Electrical Circuits: An Architecture for Quantum Computation*. Physical Review A **69**, 062320 (2004).

[41] A. Wallraff, D. I. Schuster, A. Blais, L. Frunzio, R.-S. Huang, J. Majer, S. Kumar, S. M. Girvin, and R. J. Schoelkopf. *Strong Coupling of a Single Photon to a Superconducting Qubit Using Circuit Quantum Electrodynamics*. Nature **431**, 162 (2004).

[42] I. Chiorescu, P. Bertet, K. Semba, Y. Nakamura, C. J. P. M. Harmans, and J. E. Mooij. *Coherent Dynamics of a Flux Qubit Coupled to a Harmonic Oscillator*. Nature **431**, 159 (2004).

[43] D. I. Schuster, A. A. Houck, J. A. Schreier, A. Wallraff, J. M. Gambetta, A. Blais, L. Frunzio, J. Majer, B. Johnson, M. H. Devoret, S. M. Girvin, and R. J. Schoelkopf. *Resolving Photon Number States in a Superconducting Circuit*. Nature **445**, 515 (2007).

[44] A. A. Houck, D. I. Schuster, J. M. Gambetta, J. A. Schreier, B. R. Johnson, J. M. Chow, L. Frunzio, J. Majer, M. H. Devoret, S. M. Girvin, and R. J. Schoelkopf. *Generating Single Microwave Photons in a Circuit*. Nature **449**, 328 (2007).

[45] J. Majer, J. M. Chow, J. M. Gambetta, J. Koch, B. R. Johnson, J. A. Schreier, L. Frunzio, D. I. Schuster, A. A. Houck, A. Wallraff, A. Blais, M. H. Devoret, S. M. Girvin, and R. J. Schoelkopf. *Coupling Superconducting Qubits via a Cavity Bus*. Nature **449**, 443 (2007).

[46] D. S. Dovzhenko, S. V. Ryabchuk, Y. P. Rakovich, and I. R. Nabiev. *Light–Matter Interaction in the Strong Coupling Regime: Configurations, Conditions, and Applications*. Nanoscale **10**, 3589 (2018).

[47] A. Roy and M. Devoret. *Introduction to Parametric Amplification of Quantum Signals with Josephson Circuits*. Comptes Rendus Physique **17**, 740 (2016).

[48] A. Bienfait, J. J. Pla, Y. Kubo, M. Stern, X. Zhou, C. C. Lo, C. D. Weis, T. Schenkel, M. L. W. Thewalt, D. Vion, D. Esteve, B. Julsgaard, K. Mølmer, J. J. L. Morton, and P. Bertet. *Reaching the Quantum Limit of Sensitivity in Electron Spin Resonance*. Nature Nanotechnology **11**, 253 (2016).

[49] C. Eichler, A. J. Sigillito, S. A. Lyon, and J. R. Petta. *Electron Spin Resonance at the Level of* 10^4 *Spins Using Low Impedance Superconducting Resonators*. Physical Review Letters **118**, 037701 (2017).

[50] S. Probst, A. Bienfait, P. Campagne-Ibarcq, J. J. Pla, B. Albanese, J. F. Da Silva Barbosa, T. Schenkel, D. Vion, D. Esteve, K. Mølmer, J. J. L. Morton, R. Heeres, and P. Bertet. *Inductive-Detection Electron-Spin Resonance Spectroscopy with 65 Spins/$\sqrt{Hz}$ Sensitivity*. Applied Physics Letters **111**, 202604 (2017).

[51] Y. Kubo, F. R. Ong, P. Bertet, D. Vion, V. Jacques, D. Zheng, A. Dréau, J.-F. Roch, A. Auffeves, F. Jelezko, J. Wrachtrup, M. F. Barthe, P. Bergonzo, and D. Esteve. *Strong Coupling of a Spin Ensemble to a Superconducting Resonator*. Physical Review Letters **105**, 140502 (2010).

[52] R. Amsüss, C. Koller, T. Nöbauer, S. Putz, S. Rotter, K. Sandner, S. Schneider, M. Schramböck, G. Steinhauser, H. Ritsch, J. Schmiedmayer, and J. Majer. *Cavity QED with Magnetically Coupled Collective Spin States*. Physical Review Letters **107**, 060502 (2011).

[53] D. I. Schuster, A. P. Sears, E. Ginossar, L. DiCarlo, L. Frunzio, J. J. L. Morton, H. Wu, G. A. D. Briggs, B. B. Buckley, D. D. Awschalom, and R. J. Schoelkopf. *High-Cooperativity Coupling of Electron-Spin Ensembles to Superconducting Cavities*. Physical Review Letters **105**, 140501 (2010).

[54] P. Bushev, A. K. Feofanov, H. Rotzinger, I. Protopopov, J. H. Cole, C. M. Wilson, G. Fischer, A. Lukashenko, and A. V. Ustinov. *Ultralow-Power Spectroscopy of a Rare-Earth Spin Ensemble Using a Superconducting Resonator*. Physical Review B **84**, 060501 (2011).

[55] S. Probst, H. Rotzinger, S. Wünsch, P. Jung, M. Jerger, M. Siegel, A. V. Ustinov, and P. A. Bushev. *Anisotropic Rare-Earth Spin Ensemble Strongly Coupled to a Superconducting Resonator*. Physical Review Letters **110**, 157001 (2013).

[56] C. W. Zollitsch, K. Mueller, D. P. Franke, S. T. B. Goennenwein, M. S. Brandt, R. Gross, and H. Huebl. *High Cooperativity Coupling between a Phosphorus Donor Spin Ensemble and a Superconducting Microwave Resonator*. Applied Physics Letters **107**, 142105 (2015).

[57] A. M. Tyryshkin, S. Tojo, J. J. L. Morton, H. Riemann, N. V. Abrosimov, P. Becker, H.-J. Pohl, T. Schenkel, M. L. W. Thewalt, K. M. Itoh, and S. A. Lyon. *Electron Spin Coherence Exceeding Seconds in High-Purity Silicon*. Nature Materials **11**, 143 (2011).

[58] M. Steger, K. Saeedi, M. L. W. Thewalt, J. J. L. Morton, H. Riemann, N. V. Abrosimov, P. Becker, and H.-. J. Pohl. *Quantum Information Storage for over 180 s Using Donor Spins in a ^{28}Si "Semiconductor Vacuum"*. Science **336**, 1280 (2012).

[59] K. Saeedi, S. Simmons, J. Z. Salvail, P. Dluhy, H. Riemann, N. V. Abrosimov, P. Becker, H.-J. Pohl, J. J. Morton, and M. L. Thewalt. *Room-Temperature Quantum Bit Storage Exceeding 39 Minutes Using Ionized Donors in Silicon-28*. Science **342**, 830 (2013).

[60] H. Wu, R. E. George, J. H. Wesenberg, K. Mølmer, D. I. Schuster, R. J. Schoelkopf, K. M. Itoh, A. Ardavan, J. J. L. Morton, and G. A. D. Briggs. *Storage of Multiple Coherent Microwave Excitations in an Electron Spin Ensemble*. Physical Review Letters **105**, 140503 (2010).

[61] Y. Kubo, C. Grezes, A. Dewes, T. Umeda, J. Isoya, H. Sumiya, N. Morishita, H. Abe, S. Onoda, T. Ohshima, V. Jacques, A. Dréau, J.-F. Roch, I. Diniz, A. Auffeves, D. Vion, D. Esteve, and P. Bertet. *Hybrid Quantum Circuit with a Superconducting Qubit Coupled to a Spin Ensemble*. Physical Review Letters **107**, 220501 (2011).

[62] Y. Kubo, I. Diniz, A. Dewes, V. Jacques, A. Dréau, J.-F. Roch, A. Auffeves, D. Vion, D. Esteve, and P. Bertet. *Storage and Retrieval of a Microwave Field in a Spin Ensemble*. Physical Review A **85**, 012333 (2012).

[63] C. Grezes, B. Julsgaard, Y. Kubo, W. L. Ma, M. Stern, A. Bienfait, K. Nakamura, J. Isoya, S. Onoda, T. Ohshima, V. Jacques, D. Vion, D. Esteve, R. B. Liu, K. M?lmer, and P. Bertet. *Storage and Retrieval of Microwave Fields at the Single-Photon Level in a Spin Ensemble*. Physical Review A **92**, 020301 (2015).

[64] D. F. Walls and G. J. Milburn. *Quantum Optics* (Springer Berlin Heidelberg, Berlin, Heidelberg, 1994, ISBN: 978-3-540-58831-3).

[65] E. M. Purcell. *Spontaneous Emission Probabilities at Radio Frequencies*. Physical Review **69**, 681 (1946).

[66] S. Putz, D. O. Krimer, R. Amsüss, A. Valookaran, T. Nöbauer, J. Schmiedmayer, S. Rotter, and J. Majer. *Protecting a Spin Ensemble against Decoherence in the Strong-Coupling Regime of Cavity QED*. Nature Physics **10**, 720 (2014).

[67] A. Bienfait, J. J. Pla, Y. Kubo, X. Zhou, M. Stern, C. C. Lo, C. D. Weis, T. Schenkel, D. Vion, D. Esteve, J. J. L. Morton, and P. Bertet. *Controlling Spin Relaxation with a Cavity*. Nature **531**, 74 (2016).

[68] S. Putz, A. Angerer, D. O. Krimer, R. Glattauer, W. J. Munro, S. Rotter, J. Schmiedmayer, and J. Majer. *Spectral Hole Burning and Its Application in Microwave Photonics*. Nature Photonics **11**, 36 (2017).

[69] A. Angerer, S. Putz, D. O. Krimer, T. Astner, M. Zens, R. Glattauer, K. Streltsov, W. J. Munro, K. Nemoto, S. Rotter, J. Schmiedmayer, and J. Majer. *Ultralong Relaxation Times in Bistable Hybrid Quantum Systems*. Science Advances **3**, e1701626 (2017).

[70] R. H. Dicke. *Coherence in Spontaneous Radiation Processes*. Physical Review **93**, 99 (1954).

[71] B. C. Rose, A. M. Tyryshkin, H. Riemann, N. V. Abrosimov, P. Becker, H.-J. Pohl, M. L. W. Thewalt, K. M. Itoh, and S. A. Lyon. *Coherent Rabi Dynamics of a Superradiant Spin Ensemble in a Microwave Cavity*. Physical Review X **7**, 031002 (2017).

[72] A. Angerer, K. Streltsov, T. Astner, S. Putz, H. Sumiya, S. Onoda, J. Isoya, W. J. Munro, K. Nemoto, J. Schmiedmayer, and J. Majer. *Superradiant Emission from Colour Centres in Diamond*. Nature Physics **14**, 1168 (2018).

[73] B. Julsgaard, C. Grezes, P. Bertet, and K. Mølmer. *Quantum Memory for Microwave Photons in an Inhomogeneously Broadened Spin Ensemble*. Physical Review Letters **110**, 250503 (2013).

[74] C. Grezes, Y. Kubo, B. Julsgaard, T. Umeda, J. Isoya, H. Sumiya, H. Abe, S. Onoda, T. Ohshima, K. Nakamura, I. Diniz, A. Auffeves, V. Jacques, J.-F. Roch, D. Vion, D. Esteve, K. Moelmer, and P. Bertet. *Towards a Spin-Ensemble Quantum Memory for Superconducting Qubits*. Comptes Rendus Physique **17**, 693 (2016).

[75] B. Odom, D. Hanneke, B. D'Urso, and G. Gabrielse. *New Measurement of the Electron Magnetic Moment Using a One-Electron Quantum Cyclotron*. Physical Review Letters **97**, 030801 (2006).

[76] A. Bienfait. *Magnetic Resonance with Quantum Microwaves*. PhD thesis. Université Paris-Saclay, 2016.

[77] D. J. Lepine. *Spin-Dependent Recombination on Silicon Surface*. Physical Review B **6**, 436 (1972).

[78] J. Hennig. *Echoes—How to Generate, Recognize, Use or Avoid Them in MR-Imaging Sequences. Part I: Fundamental and Not so Fundamental Properties of Spin Echoes*. Concepts in Magnetic Resonance **3**, 125 (1991).

[79] C. P. Slichter. *Spin Resonance of Impurity Atoms in Silicon*. Physical Review **99**, 479 (1955).

[80] J. P. Gordon and K. D. Bowers. *Microwave Spin Echoes from Donor Electrons in Silicon*. Physical Review Letters **1**, 368 (1958).

[81] G. Feher. *Electron Spin Resonance Experiments on Donors in Silicon. I. Electronic Structure of Donors by the Electron Nuclear Double Resonance Technique*. Physical Review **114**, 1219 (1959).

[82] G. Feher and E. A. Gere. *Electron Spin Resonance Experiments on Donors in Silicon. II. Electron Spin Relaxation Effects*. Physical Review **114**, 1245 (1959).

[83] D. K. Wilson and G. Feher. *Electron Spin Resonance Experiments on Donors in Silicon. III. Investigation of Excited States by the Application of Uniaxial Stress and Their Importance in Relaxation Processes*. Physical Review **124**, 1068 (1961).

[84] E. B. Hale and R. L. Mieher. *Shallow Donor Electrons in Silicon. I. Hyperfine Interactions from ENDOR Measurements*. Physical Review **184**, 739 (1969).

[85] H. Huebl, A. R. Stegner, M. Stutzmann, M. S. Brandt, G. Vogg, F. Bensch, E. Rauls, and U. Gerstmann. *Phosphorus Donors in Highly Strained Silicon*. Physical Review Letters **97**, 166402 (2006).

[86] L. Dreher, T. A. Hilker, A. Brandlmaier, S. T. B. Goennenwein, H. Huebl, M. Stutzmann, and M. S. Brandt. *Electroelastic Hyperfine Tuning of Phosphorus Donors in Silicon*. Physical Review Letters **106**, 037601 (2011).

[87] G. Feher, R. C. Fletcher, and E. A. Gere. *Exchange Effects in Spin Resonance of Impurity Atoms in Silicon*. Physical Review **100**, 1784 (1955).

[88] D. Jérome and J. M. Winter. *Electron Spin Resonance on Interacting Donors in Silicon*. Physical Review **134**, A1001 (1964).

[89] S. Maekawa and N. Kinoshita. *Electron Spin Resonance in Phosphorus Doped Silicon at Low Temperatures*. Journal of the Physical Society of Japan **20**, 1447 (1965).

[90] P. R. Cullis and J. R. Marko. *Determination of the Donor Pair Exchange Energy in Phosphorus-Doped Silicon*. Physical Review B **1**, 632 (1970).

[91] T. G. Castner. *Raman Spin-Lattice Relaxation of Shallow Donors in Silicon*. Physical Review **130**, 58 (1963).

[92] D. Taylor, J. Marko, and I. Bartlet. *Exchange and Dipolar Fields in Phosphorus-Doped Silicon Measured by Electron Spin Echoes*. Solid State Communications **14**, 295 (1974).

[93] P. R. Cullis. *Electron Paramagnetic Resonance in Inhomogeneously Broadened Systems: A Spin Temperature Approach*. Journal of Magnetic Resonance **21**, 397 (1976).

[94] N. Stone. *Table of Nuclear Magnetic Dipole and Electric Quadrupole Moments*. Atomic Data and Nuclear Data Tables **90**, 75 (2005).

[95] H. Morishita, L. S. Vlasenko, H. Tanaka, K. Semba, K. Sawano, Y. Shiraki, M. Eto, and K. M. Itoh. *Electrical Detection and Magnetic-Field Control of Spin States in Phosphorus-Doped Silicon*. Physical Review B **80**, 205206 (2009).

[96] E. B. Hale and R. L. Mieher. *Shallow Donor Electrons in Silicon. II. Considerations Regarding the Fermi Contact Interactions*. Physical Review **184**, 751 (1969).

[97] E. Abe, A. M. Tyryshkin, S. Tojo, J. J. L. Morton, W. M. Witzel, A. Fujimoto, J. W. Ager, E. E. Haller, J. Isoya, S. A. Lyon, M. L. W. Thewalt, and K. M. Itoh. *Electron Spin Coherence of Phosphorus Donors in Silicon: Effect of Environmental Nuclei*. Physical Review B **82**, 121201 (2010).

[98] P. R. Cullis and J. R. Marko. *Electron Paramagnetic Resonance Properties of N-Type Silicon in the Intermediate Impurity-Concentration Range*. Physical Review B **11**, 4184 (1975).

[99] S. Shankar, A. M. Tyryshkin, and S. A. Lyon. *ESR Measurements of Phosphorus Dimers in Isotopically Enriched* ^{28}*Si Silicon*. Physical Review B **91**, 245206 (2015).

[100] K. Morigaki and S. Maekawa. *Electron Spin Resonance Studies of Interacting Donor Clusters in Phosphorus-Doped Silicon*. Journal of the Physical Society of Japan **32**, 462 (1972).

[101] D. New and T. G. Castner. *Donor Clusters in Silicon. Results of ESR Measurements*. Physical Review B **29**, 2077 (1984).

[102] D. New. *Donor Clusters in Silicon. II. ESR Simulations*. Physical Review B **32**, 2419 (1985).

[103] D. M. Pozar. *Microwave Engineering* 4th ed (Wiley, Hoboken, NJ, 2012, ISBN: 978-0-470-63155-3).

[104] S. Putz. *Circuit Cavity QED with Macroscopic Solid-State Spin Ensembles*. Springer Theses: Recognizing Outstanding Ph.D. Research (Springer, Cham, 2017, ISBN: 978-3-319-66447-7).

[105] C. W. Gardiner and M. J. Collett. *Input and Output in Damped Quantum Systems: Quantum Stochastic Differential Equations and the Master Equation*. Physical Review A **31**, 3761 (1985).

[106] A. A. Clerk, M. H. Devoret, S. M. Girvin, F. Marquardt, and R. J. Schoelkopf. *Introduction to Quantum Noise, Measurement, and Amplification*. Reviews of Modern Physics **82**, 1155 (2010).

[107] K. Sandner, H. Ritsch, R. Amsüss, C. Koller, T. Nöbauer, S. Putz, J. Schmiedmayer, and J. Majer. *Strong Magnetic Coupling of an Inhomogeneous Nitrogen-Vacancy Ensemble to a Cavity*. Physical Review A **85**, 053806 (2012).

[108] M. Aspelmeyer, T. J. Kippenberg, and F. Marquardt. *Cavity Optomechanics*. Reviews of Modern Physics **86**, 1391 (2014).

[109] I. Diniz, S. Portolan, R. Ferreira, J. M. Gérard, P. Bertet, and A. Auffèves. *Strongly Coupling a Cavity to Inhomogeneous Ensembles of Emitters: Potential for Long-Lived Solid-State Quantum Memories*. Physical Review A **84**, 063810 (2011).

[110] E. Jaynes and F. Cummings. *Comparison of Quantum and Semiclassical Radiation Theories with Application to the Beam Maser*. Proceedings of the IEEE **51**, 89 (1963).

[111] I. Chiorescu, N. Groll, S. Bertaina, T. Mori, and S. Miyashita. *Magnetic Strong Coupling in a Spin-Photon System and Transition to Classical Regime*. Physical Review B **82**, 024413 (2010).

[112] F. P. Laussy, E. del Valle, M. Schrapp, A. Laucht, and J. J. Finley. *Climbing the Jaynes–Cummings Ladder by Photon Counting*. Journal of Nanophotonics **6**, 061803 (2012).

[113] G. Tosi, F. A. Mohiyaddin, H. Huebl, and A. Morello. *Circuit-Quantum Electrodynamics with Direct Magnetic Coupling to Single-Atom Spin Qubits in Isotopically Enriched* ^{28}Si. AIP Advances **4**, 087122 (2014).

[114] A. Bienfait, P. Campagne-Ibarcq, A. H. Kiilerich, X. Zhou, S. Probst, J. J. Pla, T. Schenkel, D. Vion, D. Esteve, J. J. L. Morton, K. Moelmer, and P. Bertet. *Magnetic Resonance with Squeezed Microwaves*. Physical Review X **7**, 041011 (2017).

[115] M. Tavis and F. W. Cummings. *Exact Solution for an N-Molecule—Radiation-Field Hamiltonian*. Physical Review **170**, 379 (1968).

[116] R. Amsüss. *Strong Coupling of an* NV^- *Spin Ensemble to a Superconducting Resonator*. PhD Thesis. Technische Universität Wien, 2012.

[117] K. Henschel, J. Majer, J. Schmiedmayer, and H. Ritsch. *Cavity QED with an Ultracold Ensemble on a Chip: Prospects for Strong Magnetic Coupling at Finite Temperatures*. Physical Review A **82**, 033810 (2010).

[118] J. H. Wesenberg, A. Ardavan, G. A. D. Briggs, J. J. L. Morton, R. J. Schoelkopf, D. I. Schuster, and K. Mølmer. *Quantum Computing with an Electron Spin Ensemble*. Physical Review Letters **103**, 070502 (2009).

[119] R. K. Bullough. *Photon, Quantum and Collective, Effects from Rydberg Atoms in Cavities*. Hyperfine Interactions **37**, 71 (1987).

[120] M. Gross and S. Haroche. *Superradiance: An Essay on the Theory of Collective Spontaneous Emission*. Physics Reports **93**, 301 (1982).

[121] H. Primakoff and T. Holstein. *Many-Body Interactions in Atomic and Nuclear Systems*. Physical Review **55**, 1218 (1939).

[122] Z. Kurucz, J. H. Wesenberg, and K. Mølmer. *Spectroscopic Properties of Inhomogeneously Broadened Spin Ensembles in a Cavity*. Physical Review A **83**, 053852 (2011).

[123] G. Hechenblaikner, M. Gangl, P. Horak, and H. Ritsch. *Cooling an Atom in a Weakly Driven High- Q Cavity*. Physical Review A **58**, 3030 (1998).

[124] P. Natzkin. *Superconducting Microwave Resonator Designs for Electron Spin Resonance Applications*. Master Thesis. Technische Universität München, 2017.

[125] E. Abe, K. M. Itoh, J. Isoya, and S. Yamasaki. *Electron-Spin Phase Relaxation of Phosphorus Donors in Nuclear-Spin-Enriched Silicon*. Physical Review B **70**, 033204 (2004).

[126] H.-G. Huebl. *Coherent Manipulation and Electrical Detection of Phosphorus Donor Spins in Silicon*. PhD Thesis. Technische Universität München, 2007.

[127] T. F. Rosenbaum, R. F. Milligan, M. A. Paalanen, G. A. Thomas, R. N. Bhatt, and W. Lin. *Metal-Insulator Transition in a Doped Semiconductor*. Physical Review B **27**, 7509 (1983).

[128] J. Goetz, F. Deppe, M. Haeberlein, F. Wulschner, C. W. Zollitsch, S. Meier, M. Fischer, P. Eder, E. Xie, K. G. Fedorov, E. P. Menzel, A. Marx, and R. Gross. *Loss Mechanisms in Superconducting Thin Film Microwave Resonators*. Journal of Applied Physics **119**, 015304 (2016).

[129] F. Hrubesch, G. Braunbeck, A. Voss, M. Stutzmann, and M. Brandt. *Broadband Electrically Detected Magnetic Resonance Using Adiabatic Pulses*. Journal of Magnetic Resonance **254**, 62 (2015).

[130] A. Doll, S. Pribitzer, R. Tschaggelar, and G. Jeschke. *Adiabatic and Fast Passage Ultra-Wideband Inversion in Pulsed EPR*. Journal of Magnetic Resonance **230**, 27 (2013).

[131] T. Kaufmann, T. J. Keller, J. M. Franck, R. P. Barnes, S. J. Glaser, J. M. Martinis, and S. Han. *DAC-Board Based X-Band EPR Spectrometer with Arbitrary Waveform Control*. Journal of Magnetic Resonance **235**, 95 (2013).

[132] U. Madhow. *Fundamentals of Digital Communication* (Cambridge University Press, Cambridge, UK, 2008, ISBN: 978-0-511-38606-0).

[133] J. J. de Witt. *Modelling, Estimation and Compensation of Imbalances in Quadrature Transceivers*. PhD thesis. Stellenbosch University, 2011.

[134] M. Garwood and L. DelaBarre. *The Return of the Frequency Sweep: Designing Adiabatic Pulses for Contemporary NMR*. Journal of Magnetic Resonance **153**, 155 (2001).

[135] A. Tannús and M. Garwood. *Adiabatic Pulses*. NMR in Biomedicine **10**, 423 (1997).

[136] E. Kupce and R. Freeman. *Adiabatic Pulses for Wideband Inversion and Broadband Decoupling*. Journal of Magnetic Resonance, Series A **115**, 273 (1995).

[137] P. E. Spindler, Y. Zhang, B. Endeward, N. Gershernzon, T. E. Skinner, S. J. Glaser, and T. F. Prisner. *Shaped Optimal Control Pulses for Increased Excitation Bandwidth in EPR*. Journal of Magnetic Resonance **218**, 49 (2012).

[138] T. E. Skinner, M. Braun, K. Woelk, N. I. Gershenzon, and S. J. Glaser. *Design and Application of Robust Rf Pulses for Toroid Cavity NMR Spectroscopy*. Journal of Magnetic Resonance **209**, 282 (2011).

[139] C. W. Zollitsch. *Single Excitation Transfer in the Quantum Regime: A Spin-Based Solid-State Approach*. PhD thesis. Technische Universität München, 2016.

[140] A. T. A. M. de Waele. *Basic Operation of Cryocoolers and Related Thermal Machines*. Journal of Low Temperature Physics **164**, 179 (2011).

[141] M. Greifenstein. *Elektronenspinresonanz Mit Supraleitenden Mikrowellenresonatoren Bei Millikelvin-Temperaturen*. Diploma Thesis. Technische Universität München, 2012.

[142] H. Maier-Flaig. *Magnetic Resonance of Ferrimagnetic Insulators*. PhD Thesis. Technische Universität München, 2017.

[143] M. S. Khalil, M. J. A. Stoutimore, F. C. Wellstood, and K. D. Osborn. *An Analysis Method for Asymmetric Resonator Transmission Applied to Superconducting Devices*. Journal of Applied Physics **111**, 054510 (2012).

[144] S. Probst, F. B. Song, P. A. Bushev, A. V. Ustinov, and M. Weides. *Efficient and Robust Analysis of Complex Scattering Data under Noise in Microwave Resonators*. Review of Scientific Instruments **86**, 024706 (2015).

[145] A. D. Bain. *Coherence Levels and Coherence Pathways in NMR. A Simple Way to Design Phase Cycling Procedures*. Journal of Magnetic Resonance **56**, 418 (1984).

[146] G. Bodenhausen, H. Kogler, and R. Ernst. *Selection of Coherence-Transfer Pathways in NMR Pulse Experiments*. Journal of Magnetic Resonance **58**, 370 (1984).

[147] F. Hoehne, L. Dreher, J. Behrends, M. Fehr, H. Huebl, K. Lips, A. Schnegg, M. Suckert, M. Stutzmann, and M. S. Brandt. *Lock-in Detection for Pulsed Electrically Detected Magnetic Resonance*. Review of Scientific Instruments **83**, 043907 (2012).

[148] S. Stoll and B. Kasumaj. *Phase Cycling in Electron Spin Echo Envelope Modulation*. Applied Magnetic Resonance **35**, 15 (2008).

[149] G. Bodenhausen, R. Freeman, and D. L. Turner. *Suppression of Artifacts in Two-Dimensional J Spectroscopy*. Journal of Magnetic Resonance **27**, 511 (1977).

[150] H. Kuribayashi, D. P. Bradley, D. R. Checkley, P. L. Worthington, and J. J. Tessier. *Averaging Keyhole Pulse Sequence with Presaturation Pulses and EXORCYCLE Phase Cycling for Dynamic Contrast-Enhanced MRI*. Magnetic Resonance in Medical Sciences **3**, 207 (2004).

[151] R. Narkowicz, D. Suter, and R. Stonies. *Planar Microresonators for EPR Experiments*. Journal of Magnetic Resonance **175**, 275 (2005).

[152] A. C. Torrezan, T. P. Mayer Alegre, and G. Medeiros-Ribeiro. *Microstrip Resonators for Electron Paramagnetic Resonance Experiments*. Review of Scientific Instruments **80**, 075111 (2009).

[153] A. Megrant, C. Neill, R. Barends, B. Chiaro, Y. Chen, L. Feigl, J. Kelly, E. Lucero, M. Mariantoni, P. J. J. O'Malley, D. Sank, A. Vainsencher, J. Wenner, T. C. White, Y. Yin, J. Zhao, C. J. Palmstrøm, J. M. Martinis, and A. N. Cleland. *Planar Superconducting Resonators with Internal Quality Factors above One Million*. Applied Physics Letters **100**, 113510 (2012).

[154] O. Benningshof, H. Mohebbi, I. Taminiau, G. Miao, and D. Cory. *Superconducting Microstrip Resonator for Pulsed ESR of Thin Films*. Journal of Magnetic Resonance **230**, 84 (2013).

[155] A. J. Sigillito, H. Malissa, A. M. Tyryshkin, H. Riemann, N. V. Abrosimov, P. Becker, H.-J. Pohl, M. L. W. Thewalt, K. M. Itoh, J. J. L. Morton, A. A. Houck, D. I. Schuster, and S. A. Lyon. *Fast, Low-Power Manipulation of Spin Ensembles in Superconducting Microresonators*. Applied Physics Letters **104**, 222407 (2014).

[156] H. Malissa, D. I. Schuster, A. M. Tyryshkin, A. A. Houck, and S. A. Lyon. *Superconducting Coplanar Waveguide Resonators for Low Temperature Pulsed Electron Spin Resonance Spectroscopy*. Review of Scientific Instruments **84**, 025116 (2013).

[157] M. S. Khalil, F. C. Wellstood, and K. D. Osborn. *Loss Dependence on Geometry and Applied Power in Superconducting Coplanar Resonators*. IEEE Transactions on Applied Superconductivity **21**, 879 (2011).

[158] K. Geerlings, S. Shankar, E. Edwards, L. Frunzio, R. J. Schoelkopf, and M. H. Devoret. *Improving the Quality Factor of Microwave Compact Resonators by Optimizing Their Geometrical Parameters*. Applied Physics Letters **100**, 192601 (2012).

[159] J. Gao, J. Zmuidzinas, A. Vayonakis, P. Day, B. Mazin, and H. Leduc. *Equivalence of the Effects on the Complex Conductivity of Superconductor Due to Temperature Change and External Pair Breaking*. Journal of Low Temperature Physics **151**, 557 (2008).

[160] D. S. Wisbey, J. Gao, M. R. Vissers, F. C. S. da Silva, J. S. Kline, L. Vale, and D. P. Pappas. *Effect of Metal/Substrate Interfaces on Radio-Frequency Loss in Superconducting Coplanar Waveguides*. Journal of Applied Physics **108**, 093918 (2010).

[161] J. Wenner, R. Barends, R. C. Bialczak, Y. Chen, J. Kelly, E. Lucero, M. Mariantoni, A. Megrant, P. J. J. O'Malley, D. Sank, A. Vainsencher, H. Wang, T. C. White, Y. Yin, J. Zhao, A. N. Cleland, and J. M. Martinis. *Surface Loss Simulations of Superconducting Coplanar Waveguide Resonators*. Applied Physics Letters **99**, 113513 (2011).

[162] C. P. Wen. *Coplanar Waveguide: A Surface Strip Transmission Line Suitable for Nonreciprocal Gyromagnetic Device Applications*. IEEE Transactions on Microwave Theory and Techniques **17**, 1087 (1969).

[163] T. Niemczyk, F. Deppe, M. Mariantoni, E. P. Menzel, E. Hoffmann, G. Wild, L. Eggenstein, A. Marx, and R. Gross. *Fabrication Technology of and Symmetry Breaking in Superconducting Quantum Circuits*. Superconductor Science and Technology **22**, 034009 (2009).

[164] W. J. Wallace and R. H. Silsbee. *Microstrip Resonators for Electron-spin Resonance*. Review of Scientific Instruments **62**, 1754 (1991).

[165] R. Barends, J. Wenner, M. Lenander, Y. Chen, R. C. Bialczak, J. Kelly, E. Lucero, P. O'Malley, M. Mariantoni, D. Sank, H. Wang, T. C. White, Y. Yin, J. Zhao, A. N. Cleland, J. M. Martinis, and J. J. A. Baselmans. *Minimizing Quasiparticle Generation from Stray Infrared Light in Superconducting Quantum Circuits*. Applied Physics Letters **99**, 113507 (2011).

[166] J. P. Turneaure, J. Halbritter, and H. A. Schwettman. *The Surface Impedance of Superconductors and Normal Conductors: The Mattis-Bardeen Theory*. Journal of Superconductivity **4**, 341 (1991).

[167] *CST Microwave Studio 2016*. CST Computer Simulation Technology GmbH. 2016.

[168] D. C. Mattis and J. Bardeen. *Theory of the Anomalous Skin Effect in Normal and Superconducting Metals*. Physical Review **111**, 412 (1958).

[169] *EPR Accessories*. https://www.bruker.com/fileadmin/user_upload/8-PDF-Docs/MagneticResonance/EPR_brochures/EPR_accessories.pdf. 2012.

[170] R. Meservey and P. M. Tedrow. *Measurements of the Kinetic Inductance of Superconducting Linear Structures*. Journal of Applied Physics **40**, 2028 (1969).

[171] K. Yoshida, M. S. Hossain, T. Kisu, K. Enpuku, and K. Yamafuji. *Modeling of Kinetic-Inductance Coplanar Stripline with NbN Thin Films*. Japanese Journal of Applied Physics **31**, 3844 (1992).

[172] A. J. Annunziata, D. F. Santavicca, L. Frunzio, G. Catelani, M. J. Rooks, A. Frydman, and D. E. Prober. *Tunable Superconducting Nanoinductors*. Nanotechnology **21**, 445202 (2010).

[173] M. Tinkham. *Introduction to Superconductivity* (R. E. Krieger Pub. Co, Huntington, N.Y, 1980, ISBN: 978-0-89874-049-3).

[174] K. Watanabe, K. Yoshida, T. Aoki, and S. Kohjiro. *Kinetic Inductance of Superconducting Coplanar Waveguides*. Japanese Journal of Applied Physics **33**, 5708 (1994).

[175] S. Doyle. *Lumped Element Kinetic Inductance Detectors*. PhD Thesis. Cardiff University, 2008.

[176] A. I. Gubin, K. S. Il'in, S. A. Vitusevich, M. Siegel, and N. Klein. *Dependence of Magnetic Penetration Depth on the Thickness of Superconducting Nb Thin Films*. Physical Review B **72**, 064503 (2005).

[177] M. Xu, X. Han, W. Fu, C.-L. Zou, M. H. Devoret, and H. X. Tang. *Frequency-Tunable High-*Q *Superconducting Resonators via Wireless Control of Nonlinear Kinetic Inductance*. Applied Physics Letters **114**, 192601 (2019).

[178] J. Zmuidzinas. *Superconducting Microresonators: Physics and Applications*. Annual Review of Condensed Matter Physics **3**, 169 (2012).

[179] A. B. Pippard. *Field Variation of the Superconducting Penetration Depth*. Proceedings of the Royal Society of London. Series A. Mathematical and Physical Sciences **203**, 210 (1950).

[180] J. Bardeen. *Field Variation of Superconducting Penetration Depth*. Physical Review **81**, 1070 (1951).

[181] Y. V. Sharvin and V. F. Gantmakher. *Dependence of the Depth of Penetration of the Magnetic Field in a Superconductor on the Magnetic Field Strength*. Journal of Experimental and Theoretical Physics **12**, 866 (1961).

[182] D. Gerstenberg and P. M. Hall. *Superconducting Thin Films of Niobium, Tantalum, Tantalum Nitride, Tantalum Carbide, and Niobium Nitride*. Journal of The Electrochemical Society **111**, 936 (1964).

[183] J. Rairden and C. Neugebauer. *Critical Temperature of Niobium and Tantalum Films*. Proceedings of the IEEE **52**, 1234 (1964).

[184] D. K. Finnemore, T. F. Stromberg, and C. A. Swenson. *Superconducting Properties of High-Purity Niobium*. Physical Review **149**, 231 (1966).

[185] D.-H. Wu, C. A. Shiffman, and S. Sridhar. *Field Variation of the Penetration Depth in Ceramic* $Y_1Ba_2Cu_3O_y$. Physical Review B **38**, 9311 (1988).

[186] S. Sridhar, D.-H. Wu, and W. Kennedy. *Temperature Dependence of Electrodynamic Properties of* $YBa_2Cu_3O_y$ *Crystals*. Physical Review Letters **63**, 1873 (1989).

[187] M. Arzeo, F. Lombardi, and T. Bauch. *Microwave Losses in MgO, $LaAlO_3$, and $(La_{0.3}Sr_{0.7})(Al_{0.65}Ta_{0.35})O_3$ Dielectrics at Low Power and in the Millikelvin Temperature Range*. Applied Physics Letters **104**, 212601 (2014).

[188] C. Song, T. W. Heitmann, M. P. DeFeo, K. Yu, R. McDermott, M. Neeley, J. M. Martinis, and B. L. T. Plourde. *Microwave Response of Vortices in Superconducting Thin Films of Re and Al*. Physical Review B **79**, 174512 (2009).

[189] C. Song, M. P. DeFeo, K. Yu, and B. L. T. Plourde. *Reducing Microwave Loss in Superconducting Resonators Due to Trapped Vortices*. Applied Physics Letters **95**, 232501 (2009).

[190] D. Bothner, C. Clauss, E. Koroknay, M. Kemmler, T. Gaber, M. Jetter, M. Scheffler, P. Michler, M. Dressel, D. Koelle, and R. Kleiner. *Reducing Vortex Losses in Superconducting Microwave Resonators with Microsphere Patterned Antidot Arrays*. Applied Physics Letters **100**, 012601 (2012).

[191] M. Tinkham. *Effect of Fluxoid Quantization on Transitions of Superconducting Films*. Physical Review **129**, 2413 (1963).

[192] A. Ghirri, C. Bonizzoni, D. Gerace, S. Sanna, A. Cassinese, and M. Affronte. *$YBa_2Cu_3O_7$ Microwave Resonators for Strong Collective Coupling with Spin Ensembles*. Applied Physics Letters **106**, 184101 (2015).

[193] N. Samkharadze, A. Bruno, P. Scarlino, G. Zheng, D. P. DiVincenzo, L. DiCarlo, and L. M. K. Vandersypen. *High-Kinetic-Inductance Superconducting Nanowire Resonators for Circuit QED in a Magnetic Field*. Physical Review Applied **5**, 044004 (2016).

[194] J. Kroll, F. Borsoi, K. van der Enden, W. Uilhoorn, D. de Jong, M. Quintero-Pérez, D. van Woerkom, A. Bruno, S. Plissard, D. Car, E. Bakkers, M. Cassidy, and L. Kouwenhoven. *Magnetic-Field-Resilient Superconducting Coplanar-Waveguide Resonators for Hybrid Circuit Quantum Electrodynamics Experiments*. Physical Review Applied **11**, 064053 (2019).

[195] C. M. Yen, L. E. Toth, Y. M. Shy, D. E. Anderson, and L. G. Rosner. *Superconducting* H_c-J_c *and* T_c *Measurements in the Nb–Ti–N, Nb–Hf–N, and Nb–V–N Ternary Systems*. Journal of Applied Physics **38**, 2268 (1967).

[196] T. Shiino, S. Shiba, N. Sakai, T. Yamakura, L. Jiang, Y. Uzawa, H. Maezawa, and S. Yamamoto. *Improvement of the Critical Temperature of Superconducting NbTiN and NbN Thin Films Using the AlN Buffer Layer*. Superconductor Science and Technology **23**, 045004 (2010).

[197] D. Bothner, T. Gaber, M. Kemmler, D. Koelle, and R. Kleiner. *Improving the Performance of Superconducting Microwave Resonators in Magnetic Fields*. Applied Physics Letters **98**, 102504 (2011).

[198] D. Bothner, D. Wiedmaier, B. Ferdinand, R. Kleiner, and D. Koelle. *Improving Superconducting Resonators in Magnetic Fields by Reduced Field Focussing and Engineered Flux Screening*. Physical Review Applied **8**, 034025 (2017).

[199] J. E. Healey, T. Lindström, M. S. Colclough, C. M. Muirhead, and A. Y. Tzalenchuk. *Magnetic Field Tuning of Coplanar Waveguide Resonators*. Applied Physics Letters **93**, 043513 (2008).

[200] M. R. Vissers, J. Hubmayr, M. Sandberg, S. Chaudhuri, C. Bockstiegel, and J. Gao. *Frequency-Tunable Superconducting Resonators via Nonlinear Kinetic Inductance*. Applied Physics Letters **107**, 062601 (2015).

[201] O. Kennedy, J. Burnett, J. Fenton, N. Constantino, P. Warburton, J. Morton, and E. Dupont-Ferrier. *Tunable Nb Superconducting Resonator Based on a Constriction Nano-SQUID Fabricated with a Ne Focused Ion Beam*. Physical Review Applied **11**, 014006 (2019).

[202] E. H. Poindexter, P. J. Caplan, B. E. Deal, and R. R. Razouk. *Interface States and Electron Spin Resonance Centers in Thermally Oxidized (111) and (100) Silicon Wafers*. Journal of Applied Physics **52**, 879 (1981).

[203] A. Stesmans and V. V. Afanas'ev. *Electron Spin Resonance Features of Interface Defects in Thermal (100)Si/SiO*$_2$. Journal of Applied Physics **83**, 2449 (1998).

[204] P. F. Herskind, A. Dantan, J. P. Marler, M. Albert, and M. Drewsen. *Realization of Collective Strong Coupling with Ion Coulomb Crystals in an Optical Cavity*. Nature Physics **5**, 494 (2009).

[205] *EMXplus Digital Upgrade*. https://www.bruker.com/fileadmin/user_upload/8-PDF-Docs/MagneticResonance/EPR_brochures/EMXUpgrade.pdf. 2012.

[206] T. G. Castner. *Saturation of the Paramagnetic Resonance of a V Center*. Physical Review **115**, 1506 (1959).

[207] A. M. Portis. *Electronic Structure of F Centers: Saturation of the Electron Spin Resonance*. Physical Review **91**, 1071 (1953).

[208] P. Fajer, A. Watts, and D. Marsh. *Saturation Transfer, Continuous Wave Saturation, and Saturation Recovery Electron Spin Resonance Studies of Chain-Spin Labeled Phosphatidylcholines in the Low Temperature Phases of Dipalmitoyl Phosphatidylcholine Bilayers. Effects of Rotational Dynamics and Spin-Spin Interactions*. Biophysical Journal **61**, 879 (1992).

[209] J. J. Pla, A. Bienfait, G. Pica, J. Mansir, F. A. Mohiyaddin, Z. Zeng, Y. M. Niquet, A. Morello, T. Schenkel, J. J. L. Morton, and P. Bertet. *Strain-Induced Spin-Resonance Shifts in Silicon Devices*. Physical Review Applied **9**, 044014 (2018).

[210] S. R. Staewen, A. J. Johnson, B. D. Ross, T. Parrish, H. Merkle, and M. Garwood. *3-D FLASH Imaging Using a Single Surface Coil and a New Adiabatic Pulse, BIR-4*. Investigative Radiology **25**, 559 (1990).

[211] W. Kallies and S. J. Glaser. *Cooperative Broadband Spin Echoes through Optimal Control*. Journal of Magnetic Resonance **286**, 115 (2018).

[212] M. Bailleul, D. Olligs, and C. Fermon. *Propagating Spin Wave Spectroscopy in a Permalloy Film: A Quantitative Analysis*. Applied Physics Letters **83**, 972 (2003).

[213] M. Benito, X. Mi, J. M. Taylor, J. R. Petta, and G. Burkard. *Input-Output Theory for Spin-Photon Coupling in Si Double Quantum Dots*. Physical Review B **96**, 235434 (2017).

[214] M. Harder, Y. Yang, B. M. Yao, C. H. Yu, J. W. Rao, Y. S. Gui, R. L. Stamps, and C.-M. Hu. *Level Attraction Due to Dissipative Magnon-Photon Coupling*. Physical Review Letters **121**, 137203 (2018).

[215] H. Y. Carr and E. M. Purcell. *Effects of Diffusion on Free Precession in Nuclear Magnetic Resonance Experiments*. Physical Review **94**, 630 (1954).

[216] S. Meiboom and D. Gill. *Modified Spin-Echo Method for Measuring Nuclear Relaxation Times*. Review of Scientific Instruments **29**, 688 (1958).

[217] G. Deville, M. Bernier, and J. M. Delrieux. *NMR Multiple Echoes Observed in Solid* ^{3}*He*. Physical Review B **19**, 5666 (1979).

[218] G. Eska, H.-G. Willers, B. Amend, and W. Wiedemann. *Spin Echo Experiments in Superfluid* ^{3}*He*. Physica B+C **108**, 1155 (1981).

[219] Y. Hasegawa. *Multiple Spin Echoes in Superfluid* ^{3}*He*. Progress of Theoretical Physics **67**, 1232 (1982).

[220] J. Owers-Bradley. *Measurements on Nuclear Spin Polarized* ^{3}*He-*^{4}*He Solutions*. Physica B: Condensed Matter **169**, 190 (1991).

[221] A. S. Bedford, R. M. Bowley, J. R. Owers-Bradley, and D. Wightman. *Multiple Spin Echoes in Spin Polarized Fermi Liquids*. Journal of Low Temperature Physics **85**, 389 (1991).

[222] G. Nunes, C. Jin, D. L. Hawthorne, A. M. Putnam, and D. M. Lee. *Spin-Polarized* ^{3}*He-*^{4}*He Solutions: Longitudinal Spin Diffusion and Nonlinear Spin Dynamics*. Physical Review B **46**, 9082 (1992).

[223] R. Bowtell, R. Bowley, and P. Glover. *Multiple Spin Echoes in Liquids in a High Magnetic Field*. Journal of Magnetic Resonance **88**, 643 (1990).

[224] W. Warren, S. Lee, W. Richter, and S. Vathyam. *Correcting the Classical Dipolar Demagnetizing Field in Solution NMR*. Chemical Physics Letters **247**, 207 (1995).

[225] R. Bowtell and P. Robyr. *Structural Investigations with the Dipolar Demagnetizing Field in Solution NMR*. Physical Review Letters **76**, 4971 (1996).

[226] A. Vlassenbroek, J. Jeener, and P. Broekaert. *Radiation Damping in High Resolution Liquid NMR: A Simulation Study*. The Journal of Chemical Physics **103**, 5886 (1995).

[227] M. P. Augustine and K. W. Zilm. *Observation of Bulk Susceptibility Effects in High-Resolution Nuclear Magnetic Resonance*. Journal of Magnetic Resonance, Series A **123**, 145 (1996).

[228] D. Einzel, G. Eska, Y. Hirayoshi, T. Kopp, and P. Wolfle. *Multiple Spin Echoes in a Normal Fermi Liquid*. Physical Review Letters **53**, 2312 (1984).

[229] N. Bloembergen and R. V. Pound. *Radiation Damping in Magnetic Resonance Experiments*. Physical Review **95**, 8 (1954).

[230] S. Bloom. *Effects of Radiation Damping on Spin Dynamics*. Journal of Applied Physics **28**, 800 (1957).

[231] M. Augustine. *Transient Properties of Radiation Damping*. Progress in Nuclear Magnetic Resonance Spectroscopy **40**, 111 (2002).

[232] A. M. Tyryshkin, S. A. Lyon, A. V. Astashkin, and A. M. Raitsimring. *Electron Spin Relaxation Times of Phosphorus Donors in Silicon*. Physical Review B **68**, 193207 (2003).

[233] W. M. Witzel, M. S. Carroll, A. Morello, Ł. Cywiński, and S. Das Sarma. *Electron Spin Decoherence in Isotope-Enriched Silicon*. Physical Review Letters **105**, 187602 (2010).

[234] S. Takahashi, R. Hanson, J. van Tol, M. S. Sherwin, and D. D. Awschalom. *Quenching Spin Decoherence in Diamond through Spin Bath Polarization*. Physical Review Letters **101**, 047601 (2008).

[235] S. Probst, H. Rotzinger, A. V. Ustinov, and P. A. Bushev. *Microwave Multimode Memory with an Erbium Spin Ensemble*. Physical Review B **92**, 014421 (2015).

[236] C. Kutter, H. P. Moll, J. van Tol, H. Zuckermann, J. C. Maan, and P. Wyder. *Electron-Spin Echoes at 604 GHz Using Far Infrared Lasers*. Physical Review Letters **74**, 2925 (1995).

[237] J. Goetz, F. Deppe, P. Eder, M. Fischer, M. Müting, J. P. Martínez, S. Pogorzalek, F. Wulschner, E. Xie, K. G. Fedorov, A. Marx, and R. Gross. *Second-Order Decoherence Mechanisms of a Transmon Qubit Probed with Thermal Microwave States*. Quantum Science and Technology **2**, 025002 (2017).

[238] J. R. Klauder and P. W. Anderson. *Spectral Diffusion Decay in Spin Resonance Experiments*. Physical Review **125**, 912 (1962).

[239] V. V. Kurshev and T. Ichikawa. *Effect of Spin Flip-Flop on Electron-Spin-Echo Decay Due to Instantaneous Diffusion*. Journal of Magnetic Resonance **96**, 563 (1992).

[240] K. Salikhov, S. Dzuba, and A. Raitsimring. *The Theory of Electron Spin-Echo Signal Decay Resulting from Dipole-Dipole Interactions between Paramagnetic Centers in Solids*. Journal of Magnetic Resonance **42**, 255 (1981).

[241] M. Alaimo and I. Roberts. *Effects of Paramagnetic Cations on the Non-exponential Spin-Lattice Relaxation of Rare Spin Nuclei in Solids*. Solid State Nuclear Magnetic Resonance **8**, 241 (1997).

[242] D. J. Wineland, J. J. Bollinger, W. M. Itano, F. L. Moore, and D. J. Heinzen. *Spin Squeezing and Reduced Quantum Noise in Spectroscopy*. Physical Review A **46**, R6797 (1992).

[243] D. J. Wineland, J. J. Bollinger, W. M. Itano, and D. J. Heinzen. *Squeezed Atomic States and Projection Noise in Spectroscopy*. Physical Review A **50**, 67 (1994).

[244] M. Kitagawa and M. Ueda. *Squeezed Spin States*. Physical Review A **47**, 5138 (1993).

[245] F. Wilczek. *Quantum Time Crystals*. Physical Review Letters **109**, 160401 (2012).

[246] J. Zhang, P. W. Hess, A. Kyprianidis, P. Becker, A. Lee, J. Smith, G. Pagano, I.-D. Potirniche, A. C. Potter, A. Vishwanath, N. Y. Yao, and C. Monroe. *Observation of a Discrete Time Crystal*. Nature **543**, 217 (2017).

DANKSAGUNG

Diese Dissertation fasst die Ergebnisse meiner Doktorarbeit der letzten vier Jahre zusammen. In dieser Zeit hatte ich das Vergnügen mit Kolleginnen und Kollegen am Walther-Meißner-Institut (und darüber hinaus) an spannenden Projekten zu arbeiten, um gemeinsam die Wissenschaft ein wenig nach vorne zu bewegen. An dieser Stelle möchte ich mich nun bei all den Personen bedanken, die zum Gelingen dieser Arbeit beigetragen haben.

Insbesondere möchte ich mich bei meinem Doktorvater *Dr. Hans Hübl* und *Prof. Rudolf Gross* bedanken, die meine Promotion am WMI ermöglicht haben. *Hans* hat mir dabei von Anfang an großes Vertrauen geschenkt, was sich in sehr viel Freiheit hinsichtlich meiner Arbeitsweise im Labor niedergeschlagen hat. Dennoch konnte man sich stets darauf verlassen, gute Hinweise oder auch das ein oder andere Mikrowellenbauteil aus einer seiner magischen Schubladen zu erhalten. Ich danke dir auch für die Organisation unseres Forschungsaufenthalts an der University of New South Wales in Sydney, Australien. Es war eine großartige Zeit mit dir! Bei *Prof. Gross* möchte ich mich ebenfalls für das entgegengebrachte Vertrauen bedanken und die Möglichkeit, meine Doktorarbeit am WMI zu verfassen. Seine Kommentare zu meinen Manuskripten und Konferenzbeiträgen haben stets zu mehr Nachdenken (im positiven Sinne) geführt und die entstehenden Werke noch ein Stückchen besser gemacht.

Diese Promotion (wie auch der Weg dahin) wäre ohne die großartige Unterstützung *meiner Familie* nicht möglich gewesen. Ich danke meinen Eltern von ganzem Herzen für ihren Rückhalt, den ich während meines Studiums und darüber hinaus genießen konnte und das Wissen, mich jederzeit auf sie verlassen zu können. Meinem Bruder *Thomas* möchte ich für seine Geduld und Interesse danken, wenn ich ihm mal wieder erklärt habe, was ich eigentlich genau mache. Danke, dass ihr in jeder Situation und bei allen Entscheidungen hinter mir steht.

Darüber hinaus möchte ich noch weiteren Kollegen und Freunden danken, insbesondere

- *Dr. Mathias Weiler*, für Diskussionen und Anregungen zu Manuskripten und die Bereitschaft uns im AC-Meeting an seinem Wissen teilhaben zu lassen, insbesondere was die experimentellen Aspekte im Labor angeht.
- *Prof. Dr. Martin Brandt*, für die vielen Diskussionen im Walther-Seminar, deine Kommentare und Anregungen zu den Veröffentlichungen und die vielen Geschichten rund um den wissenschaftlichen Betrieb.
- *Christoph Zollitsch*, der als mein „Vorgänger" wesentliche Beiträge zu dieser Arbeit geleistet hat. So war er nicht nur am Aufbau des kryogenen Mikrowellensetups beteiligt, sondern hat auch die Probe fabriziert, mit denen der Großteil der Experimente im zweiten Teil der Arbeit durchgeführt wurde. Ich habe die Zusammenarbeit mit dir sehr genossen, was insbesondere auch durch deine lockere Art und dem Gefühl, dass dich nichts aus der Ruhe bringen kann, bedingt ist.
- den Bachelor- und Masterstudenten *Daniela Lutz, Niklas Bruckmooser, Andreas Faltermeier* und *Petio Natzkin*, mit denen ich während meiner Promotion zusammengearbeitet habe. Ich hoffe, ihr hattet genauso viel Spaß im Labor, wie ich! Ganz besonders möchte ich *Petio* danken, der mit seiner Arbeit zu den supralei-

tenden Resonatoren den Grundstein für den ersten Teil dieser Arbeit gelegt hat.

- den Mitarbeitern der feinmechanischen Werkstatt, *Georg Nitschke*, *Christian Reichlmeier*, *Alexander Rößl* und *Helmut Thieß*, die sich mit so mancher handgezeichneter Konstruktionszeichnung auseinandersetzen mussten und dabei immer erstklassige Arbeiten abgeliefert haben. Vielen Dank auch für eure zahlreichen Ratschläge rund um meine Konstruktionen und das Leihen von Werkzeugen (das ich hoffentlich immer rechtzeitig zurückgebracht habe).
- den Mitarbeitern der Heliumverflüssigung, *Peter Binkert*, *Jan Naundorf* und *Harald Schwaiger* für die problemlose Versorgung mit Flüssighelium und -stickstoff, auch wenn ich mal wieder vergessen habe, mich in die Liste einzutragen.
- *Christoph Kastl* und *Andreas Russo* für ihre Hilfe bei allen Belangen was Elektronik und Elektrik angeht. Ein großes Dankeschön gilt insbesondere Christoph, der die Steuerelektronik für das Spektrometer mitentworfen und die Platine gebaut hat.
- *Astrid Habel* für das Polieren mehrerer ^{28}Si:P Wafer für meine Experimente sowie das Vergolden von Kryo-Bauteilen.
- *Sebastian Kammerer*, *Tom Brenninger* und *Sepp Höß*, die immer bereitwillig bei jedwedem Problem zur Hilfe kamen.
- *Sybille Plöderl* und *Maria Botta*, die nicht nur für Ordnung und Sauberkeit gesorgt haben, sondern auch für eine angenehme Arbeitsatmosphäre durch den ein oder anderen Plausch.
- dem Verwaltungpersonal, das uns Wissenschaftlern sehr viel Bürokratie abnimmt und erst so die Forschung ermöglicht. Insbesondere möchte ich *Emel Dönertas* danken, die mich nicht nur einmal an Rechnungen und Dienstreiseabrechnungen erinnert hat.

- der Magnetiker- und Qubit-Gruppe, denen ich jeweils zur Hälfte angehörte. Obwohl die Teilnahme an zwei Gruppenmeetings pro Woche durchaus zeitintensiv war, konnte ich dennoch von der (manchmal gar nicht so) unterschiedlichen Sichtweise auf die Physik profitieren.

- meinen Bürokollegen *Edwar Xie*, *Lukas Liensberger*, *Daniel Jost* und *Thomas Luschmann*, für die spannende und unterhaltsame Zeit im Büro. *Daniel* danke ich insbesondere für das ein- oder andere Schachspiel, bei denen ich meistens ziemlich schnell schachmatt gesetzt wurde.

- *Philip Schmidt*, mit dem ich so manche Stunde im Labor verbracht habe um den TRITON-Kryostat auf- und wieder zuzuschrauben. Vielen Dank für dein stets ehrlich gemeintes Interesse an meiner Arbeit und an den vielen Verbesserungsvorschlägen, die du hattest.

- *Dr. Stephan Geprägs*, für deine vielen Ratschläge und deine immerzu optimistische und humorvolle Einstellung. Auch wenn wir nie zusammen an einem Forschungsprojekt gearbeitet haben, habe ich unseren morgendlichen Kaffee und die Übungsbesprechung mit dir immer sehr genossen.

- *Natalie Segercrantz*, for the many discussions regarding physics and other (probably more important) topics in the brief time we shared an office. I really enjoy going for a run with you, even though I suspect, we only go running to have a opportunity to talk.

- *Hannes Maier-Flaig*, der die ersten beiden Jahre am WMI mein Schreibtischnachbar war und darüber hinaus zu einem sehr guten Freund wurde. Nicht nur am Institut habe ich mich immer über seine klugen und humorvollen Kommentare gefreut, zusammen haben wir auch so manche Berge bestiegen, steile Felswände durchklettert und den ein oder anderen Wasserfall (unabhängig voneinander) entdeckt.

- *Kathrin Ganzhorn*, *Michael Fischer* und *Daniel Schwienbacher*, die im Laufe der Jahre von Kollegen zu guten Freunden wurden. Zusammen mit Natalie und Hannes haben wir auch viel Zeit außerhalb des Instituts verbracht, was immer eine willkommene Abwechslung war. Vielen Dank für die vielen unterhaltsamen Stunden beim gemeinsamen Kochen oder bei Spieleabenden!